Electronic Structure of GaSb/GaAs and Si/Ge Quantum Dots

by Stephen Michael North

NEWCASTLE UNIVERSITY LIBRARY
201 16698 5
Thesis L7100

A theoretical thesis submitted to the University of Newcastle upon Tyne for the degree of Doctor of Philosophy.

September, 2001

Dedicated to the memory of Patricia North.

Declaration

This thesis has not previously been submitted by the candidate for a degree in this or any other university.

S. M. North

September, 2001

Abstract

There are significant differences between experiment and theoretical calculations of the electronic structure of GaSb/GaAs self-assembled quantum dots. Using a multi-band effective mass approximation it is shown that the influence of size and geometry of quantum dots has little or no effect in determining the hydrostatic strain. Furthermore, the valence-band ground state energies of the quantum dots studied are surprisingly consistent. This apparent paradox attributed to the influence of biaxial strain in shaping the heavy-hole and light-hole potentials. Consequently, it is shown that a simple, hydrostatically derived potential is insufficient to accurately describe the electronic structure of such quantum dots. In addition, using the latest experimental results measuring the conduction-band offset, it has been shown that much better experimental contact may be achieved for the magnitude of the transition energies derived compared to theoretically derived transition energies. The transition energies of Si/Ge self-assembled quantum dots has also been calculated. In particular, a range of quantum dot structures have been proposed that are predicted to have an optical response in the 3-5 micron range.

Some of the work presented in this thesis has been published in the following papers:-

1. "Electronic Structure of GaSb/GaAs Quantum Domes", S. M. North, M. A. Cusack, P. R. Briddon, and M. Jaros, Physical Review B **58**, 12601 (1998).

2. "Si/Ge Self-Assembled Quantum Dots for Infrared Applications", M. A. Cusack, P. R. Briddon, S. M. North, M. R. Kitchin, and M. Jaros, Semi. Sci. Tech. **16**, L81 (2001).

Acknowledgments

I should like to thank my family for support and encouragement during the course of my studies. Also, members of the Theory of Condensed Matter Group, in particular, Dr. Patrick Briddon, Dr. Jerry Hagon, Dr. Matthew Kitchin, Dr. Mark Cusack and, of course, my supervisor Professor Milan Jaros. I would also like to thank J. Michael Straczynski for showing that the impossible is possible and that Faith Manages.

This study was made possible by the financial assistance of the Engineering and Physical Sciences Research Council.

Contents

Contents 7

1 Introduction and Background 10

1.1 Semiconductor Heterostructures 11

1.2 Modeling Semiconductor Heterostructures 19

1.3 Overview of Thesis 20

2 Essential Solid State Physics 23

2.1 The Bravais Lattice and the Zinc-Blende Structure 23

2.2 The Reciprocal Lattice 25

2.3 Bloch Functions 27

2.4 Energy Bands and the Brillouin Zone 28

2.5 Charge Carriers in Semiconductors 31

3 Calculation of the Electronic Band Structure of Semiconductor Heterostructures 34

3.1 Local Empirical Pseudopotential Theory 35

3.1.1 Formulation of the Local Empirical Pseudopotential Method 35
3.1.2 Representation of Bulk Materials 37
3.1.3 Representation of Supercells by the Empirical Pseudopotential Method 39
3.2 $\mathbf{k} \cdot \mathbf{p}$ Theory for Self-assembled Quantum Dots 41
3.2.1 The Kane Model 42
3.2.2 Strain Effects on Band Structures 47
3.2.3 Describing Heterostructures 52
4 Applying the $\mathbf{k} \cdot \mathbf{p}$ Method to Quantum Dot Heterostructures 55
4.1 Atomic Positions 56
4.2 Strain Distribution 60
4.3 Confining Potentials 61
4.4 Effective Masses 63
5 Si/Ge Quantum Dots for Infrared Applications 65
5.1 Introduction and Background 66
5.2 Determining the Correct Quantum Dot Size to Model 67
5.3 The Strain Distribution and Electronic Structure 69
5.4 Conclusion 73
6 Electronic Structure of GaSb/GaAs Quantum Dots 74
6.1 Introduction and Background 75
6.2 Electronic Structure 77
6.3 Discussion 83

6.4 Summary 85

7 Direct Modeling of GaSb/GaAs Quantum Dot Structures 87

7.1 Adaptation of the Method for Larger Unit Cell Sizes 88

7.1.1 Parallelisation of the Valence Force Field Method . . . 88

7.1.2 Optimisation of the Electronic Structure Calculation . 90

7.2 Results and Discussion 91

7.3 Summary 95

8 Conclusions 103

8.1 Future Study 105

Chapter 1

Introduction and Background

The advancement of techniques of crystal growth such as Molecular Beam Epitaxy (MBE) and metal-organic chemical vapour deposition (MOCVD) has led to the ability to fabricate semiconductor-based materials with alternate layers with atomic precision. This remarkable level of control over the growth of these so-called semiconductor "heterostructures" has led some researchers to design novel semiconductor structures that aid in the study of fundamental physics and can also be incorporated into electronic or optical devices. The analytical solution of Schrödinger's equation is demonstrated to every first year physics undergraduate using the one-dimensional "particle-in-a-box" problem. So, with the advent of the processes and degree of control described above, it became possible to actually realise such structures. This, of course, attracted a great deal of academic interest. However, the possible applications of this technology were quickly exploited: with the ability to choose the composition,

layer thicknesses, doping and strain in such structures came the ability to taylor the electronic and optical properties of a heterostructure and subsequently the properties of the device upon which the structure is based. This chapter contains an introduction to the physics of semiconductor heterostructures as well as a review of those properties of semiconductor structures upon which technological devices depend.

1.1 Semiconductor Heterostructures

The conduction electrons in a perfect (i.e. defect-free) sample of a bulk semiconductor such as GaAs are virtually uninhibited by the presence of the periodic potential due to the regular lattice of atoms and are consequently essentially free to propagate throughout the crystal. These electrons are distributed over a continuous energy "band" with the quantum aspect of their character hidden away. However, if two or more layers of different semiconductor materials are fabricated on top of one another we create a “heterostructure”. This aligning of two materials together has the affect of introducing a real-space discontinuity into the conduction band. This occurs because the absolute values of the conduction band energies in each material are, in general, different (see Figure (1.1)). This difference is termed the "conduction band offset" (there is also a similar effect in the valence band). If the conduction band offset is great enough, then the electrons become confined to the material with the lowest band energy, and hence the number of degrees of freedom that they exhibit is

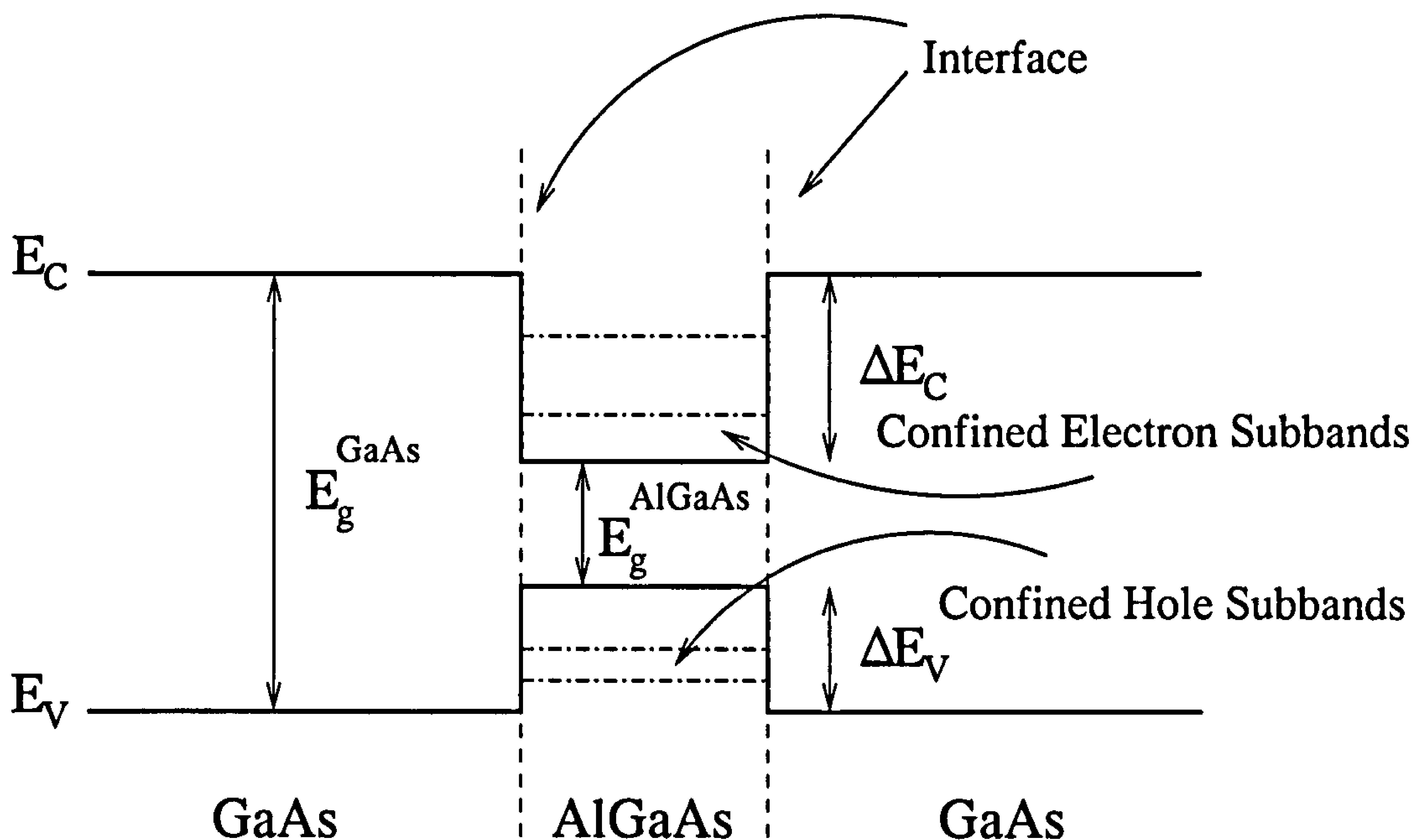

Figure 1.1: The band structure of a quantum well created by the sandwiching of a layer of $Al_xGa_{1-x}As$ between two thicker layers of GaAs.

reduced. One of the most widely studied semiconductor heterostructures is the GaAs/$Al_xGa_{1-x}As$ (where the aluminum mole fraction, x, can be between 0 and 1) quantum well structure. This structure was first proposed by Esaki and Tsu in 1970 and constructed by Chang *et al.* in 1973. This heterostructure is constructed by the growth of a layer of $Al_xGa_{1-x}As$ on a GaAs substrate followed by a thin ($\sim 10^{-9}$m) layer of GaAs, then capped with another layer of $Al_xGa_{1-x}As$. These structures can then provide a range of tailor-made electronic and optical properties by the choice of the material composition and the thickness of the epitaxial layer.

As mentioned above, the ability to select the electronic and optical characteristics of quantum well structures is a result of the reduced de-

grees of motion of the charge carriers within them. Since the number of electronic degrees of freedom are reduced by the discontinuous potential introduced by the alignment of two materials, that generally have different band gaps, the conduction and valence band offsets at the interface must first be determined. As the band gap of any semiconductor is an intrinsic property of the material (and we assume that it is unchanged by the interface) we must gain knowledge of the local chemistry on an atomic scale. This is generally achieved by experimental measurement or by *ab initio* calculations. For carriers in such a heterostructure, namely the electrons in the conduction band and holes in the valence band, the discontinuity represents a step in potential energy. The alternating layers of materials with different band gaps form a potential well and barrier to the electrons and holes (see Figure (1.1)). If the width of the potential well formed by the material with the smaller band gap is less than a de Broglie wavelength of the electrons or holes in the material (for example less than $\approx$ 15 nm for electrons in GaAs), the motion can be considered as quantised in the direction parallel to the growth axis. However, in the plane of the quantum well, their motion is still free. Under these circumstances, the electrons and holes are distributed over discrete subbands rather that over an energy continuum as in a bulk semiconductor material. The relative spacing of these subbands depends upon the depth and width of the potential well that is controlled by the choice of aluminum mole fraction and epitaxial layer thickness of GaAs respectively. Thus by changing these two experimental parameters we can fabricate wells that

can emit and absorb light at specific frequencies.

Further control over the band structure can be achieved by fabricating many such quantum wells on top of one another. If these quantum wells are separated by thick layers (> 100Å) of barrier material such that the wavefunctions of the confined electrons and holes do not overlap we create a multiple quantum well (MQW) structure. These structures will of course have the same properties as a single quantum well structure. However, Esaki and Tsu, (1970) proposed a modification to the MQW heterostructure, in which the barrier layers are grown sufficiently thin to allow significant wavefunctions tunneling between adjacent wells. These structures have subsequently been named *superlattices* and may be endowed with a periodicity that is entirely determined by the repeat length of the multilayer configuration. Owing to wavefunction tunneling, the discrete electron levels broaden into *mini-bands.* However, unlike their bulk counterparts, the band structure of these man-made materials may also be tailored by the fabricator due to the wide range of material combinations (including alloyed materials) and layer thicknesses that may be used. Furthermore, it is not required that the lattice constant of the materials used in the heterostructure have the same lattice constant (as do GaAs and AlAs) and so if materials with different lattice constants are used then strain fields may arise in the structure. Strain effects lead to shifts and degeneracy breaking in the band structure and, provided that they are not so large as to cause dislocations in the lattice, can function as an extra design parameter in the tuning of the mini-band structure.

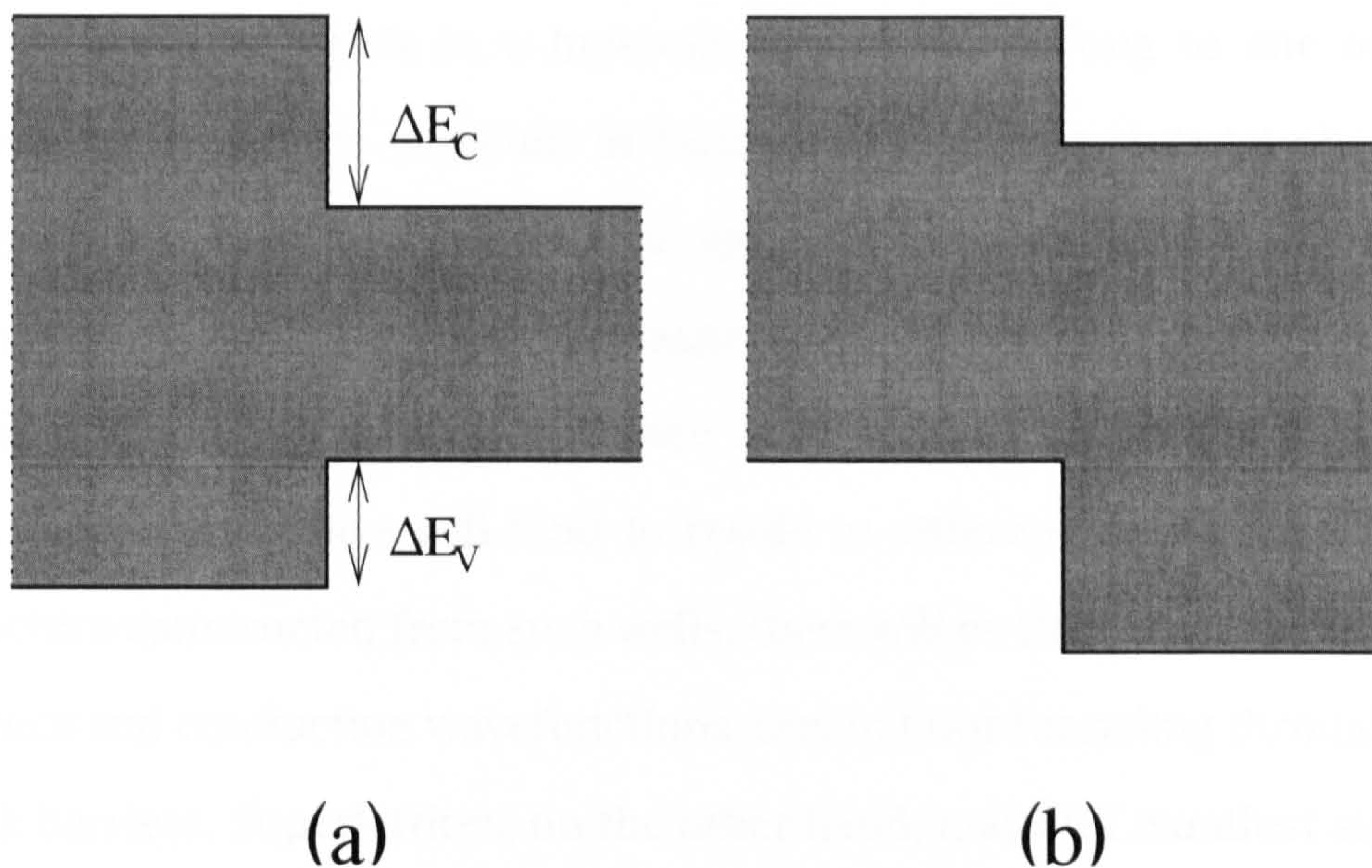

Figure 1.2: Schematic diagrams depicting the band structure interfaces: (a) Type–I (straddling lineup) and (b) Type–II (staggered lineup).

The electronic properties of semiconductors are dependent upon the availability of holes in the valence band and electrons in the conduction band to facilitate the flow of charge under an applied potential. Similarly, optical properties arise from the electromagnetic energy absorbed or emitted as free carriers undergo interband (between valence and conduction band) or intersubband (between mini-bands) transitions. In consequence of this and the above design parameters, the fabricator can construct heterostructures tailored for some potential device with technological applications This has led to the science of *band engineering* (see Capasso and Cho, 1994).

For a given set of the aforementioned design parameters, the band line-ups that may result at a heterojunction (i.e. the interface between

two different materials in a heterostructure) will belong to one of the alignment categories depicted in Figure (1.2). Figure (1.2) (a) shows a "Type I" interface, i.e. the electron and holes are confined to the same material. If the band offset is staggered as in Figure (1.2) (b) the line up is said to be "Type II". In a case such as this, the confined valence and conduction states will tend to reside in different layers. In a MQW structure constructed from such wells, there will be little overlap between valence and conduction wavefunctions, due to poor tunneling through the thick barriers. Superlattices, on the other hand, may still manifest significant overlap due to charge leakage through the thin barriers, even though the valence and conduction mini-bands are largely located in different regions of the structure. The overlap of the wavefunction in such structures is key to determining their optical response and leads to another design parameter for creating a suitable novel material.

Doping quantum well structures with donor or acceptor impurities provides further scope for tailoring their electronic and optical properties. Doping supplies mobile charge carriers to the lowest conduction and valence subbands and thus allows absorption and emission to take place as a result of intersubband transitions (i.e. transitions between conduction or valence subbands) in addition to the interband transitions (i.e., valence subband to conduction subband) that are generally responsible for the generation of optical spectra in these materials. Doped GaAs/AlGaAs quantum well systems are efficient absorbers of infra-red radiation in the 8-12 μm wavelength range because of the narrow energy separation of

quantum well states and the large electron transition probabilities for intersubband transitions. This makes doped GaAs/AlGaAs quantum well systems suitable as infra-red detectors in remote sensing application because the Earth's atmosphere is transparent to electromagnetic radiation with radiation of this wavelength.

By taking the concept of quantum confinement to its logical conclusion one arrives at the concept of a so-called quantum dot structure. A quantum dot is a heterostructure with zero dimensions, i.e. the electrons and holes are confined in all three dimensions to a point, denied even the limited freedom conceded to electrons in a bulk semiconductor. Owing to this complete quantisation of the motion of the charge confined within them, quantum dots exhibit an atomic-like spectrum of energies and a density of states that resembles a series of delta-functions. Up until the early 1990s the most popular method of fabricating quantum dots involved the patterning of quantum wells using advanced lithography and etching techniques similar to those used in the fabrication of state-of-the-art integrated circuits (Reed, 1993). This process involves an electron beam scanning a semiconductor surface that has been coated with a thin polymer called a resist. A series of process steps replaces the resist with a thin layer of metal in areas where the beam was scanned at high intensity. A shower of reactive gas then etches away the unprotected quantum well material, leaving pillars as small as $10^3 Å$ across. Surface effects repel charge from the outside of the pillar, confining it to a $10^2 Å$ region of the GaAs well layer in the process.

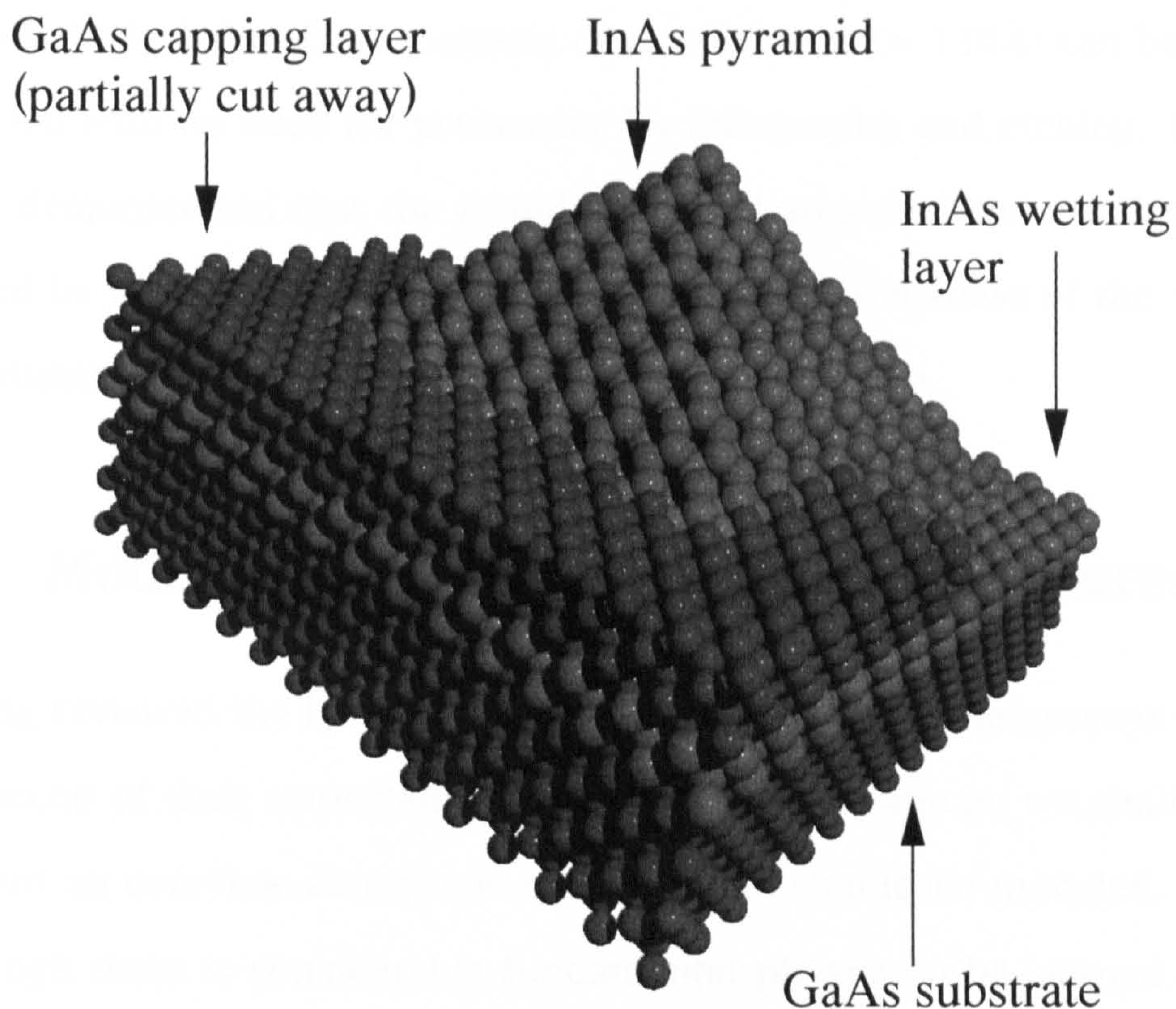

Figure 1.3: InAs/GaAs self-assembled quantum dot, reproduced from Cusack (1996).

However, recent studies (Mosion *et al*, 1994; Marzin *et al*, 1994; Medeiros-Ribeiro *et al*, 1995; Gruundmann *et al*, 1995a) have shown that it also possible to attain three dimensional confinement of charge with the Stranski–Krastanow (Stranski–Krastanow, 1939) growth process. This growth mode begins with an initial MBE layer deposition of InAs on a GaAs substrate. After a certain critical thickness is reached islands of InAs with a pyramidal geometry form spontaneously and a thin wetting layer is left under the islands see Figure (1.3). Fabrication concludes with the capping of the quantum dot island with a layer of the substrate material. By

this method, defect-free quantum dots with sizes ($\approx 120\mathring{A}$) can be constructed with no need for processing by lithography and etching. It has been demonstrated that the island sizes and area densities can be controlled by varying growth parameters such as the thickness of the initial two-dimensional layer deposition, and the growth rate.

1.2 Modeling Semiconductor Heterostructures

Having reviewed the basic properties of semiconductor heterostructures and some of their important properties and applications, we shall now present an overview about how such systems should be modeled. Now although there is considerable fundamental physics to be learned from modeling semiconductor heterostructures, the primary motivation is largely technologically based. The optoelectronics industry is reliant upon the development of devices with useful, fine-tuned wavelengths for specific applications, and this in turn requires the accurate modeling of such the underlying heterostructure. Such models require the descriptions of the constituent materials, strain and the resulting atomistic potentials, and should enable the evaluation of the subsequent optical and electronic properties.

There are a variety of physical theories and methods that have been applied to heterostructures, these include: the tight-binding approximation (Schulman and Chang, 1985), the **k.p** effective mass approximation (Bastard, 1990; Wang *et al*, 1996), *ab initio* pseudopotentials (Jones, 1988)

and the empirical pseudopotential method (Gell *et al*, 1986). Of these, the **k.p** and empirical pseudopotential methods are generally accepted to be the standard methods for calculating the stationary state solution of idealized heterostructures (Cusack *et al*, 1996; Wang *et al* 1996; Wood *et al*, 1996). First principles calculations based upon density functional theory (Dreizler and Gross, 1990), and specifically using the local density approximation and *ab initio* pseudopotentials (Bachelet *et al*, 1982), have been carried out for antimonide-based superlattices by Shaw *et al*, (1995). However, such calculations require state-of-the-art computing facilities and become infeasible for heterostructures containing large numbers of atoms such are those in a quantum dot. In consequence, most models use the **k.p** and empirical pseudopotential methods that both use parameters fitted to experimental data obtained for the bulk constituents. Wang *et al*, (1999) have carried out a detailed comparison of these two methods and their application to InAs/GaSb superlattices. There exist similar comparisons for quantum dot structures (for example Wang *et al*, (2000)). These examples show that the empirical pseudopotential method provides the more detailed atomistic description of the heterostructure and a more complete basis set.

1.3 Overview of Thesis

This thesis investigates the influence of strain and geometry on the bound ground states of self-assembled quantum dots.

In Chapter 2, an overview of a selection of key areas in solid state physics, that is, band structure, crystal symmetry and properties. The content of this chapter functions as a preamble to the main subject matter of the thesis and introduces concepts upon which the main theory is based.

In Chapter 3, an outline is given of the empirical pseudopotential method and the effective mass approximation, used to construct energy bands, wavefunctions, and effective masses in semiconductor heterostructures. The effects of strain on the band structure of bulk semiconductors is reviewed and the necessary correction to the effective Hamiltonian presented.

Chapter 4 contains the method of application of the effective mass approximation to semiconductor heterostructures. The calculation of atomic positions, strain, confining potential, effective masses and the ground state energies of the conduction and valence bands is outlined.

In Chapter 5, we examine a series of Si/Ge self-assembled quantum dots. Quantum dots are shown to provide another avenue by which it may be possible to create a material with a band-gap in the 3-5 micron range. Such a material, if validated by experiment, would prove extremely useful for IR applications.

In Chapter 6, we examine GaSb/GaAs self-assembled quantum dots. These materials are of particular interest because they exhibit a Type-II band-gap line-up. Consequently, they offer fresh opportunities for production of optical and electronic devices. We note that experimental re-

sults are counter to those produced by theory and attempt to provide better contact between the experiment and theory.

In Chapter 7, we revise our calculation of the valence-force-field and electronic structure calculation to provide a means of modeling even larger heterostructures. We revisit the GaSb/GaAs self-assembled quantum dots modeled in the previous chapter and show that the variation of biaxial strain can also reconcile experimental and theoretical results.

Finally Chapter 8 summarises the work presented here and provides avenues of further study.

Chapter 2

Essential Solid State Physics

This chapter aims to summarise the underlying elements of solid state physics that are required to fully understand the forthcoming subject matter. A more thorough and first principled description of the following summary may be found in such excellent introductory texts as Kittel, (1996) or Ashcroft and Mermin, (1976).

2.1 The Bravais Lattice and the Zinc–Blende Structure

In order to develop a model to describe the electronic structure of a crystal we must be able to model its physical structure mathematically. A *Lattice* is the term given to a spatially periodic array of points. If a group of atoms that have consistent composition, arrangement and orientation (a *basis*) is attached to all of the points in a lattice, the latter which is a

purely mathematical construct, will allow a crystal to be described. The lattice is therefore an infinite array of discrete points with an arrangement and orientation that appears equivalent regardless of the point from which it is viewed. The set of lattice geometries that can provide a description of any perfect crystal, provided the correct basis is attached at each site, are commonly referred to as *Bravais lattices.* The points in the Bravais lattice written in terms of *primitive translation vectors* $\mathbf{a}_i$ are:

$$\begin{aligned} \mathbf{r}' &= \mathbf{r} + n_1\mathbf{a}_1 + n_2\mathbf{a}_2 + n_3\mathbf{a}_3 \\ &= \mathbf{r} + \mathbf{R} \end{aligned} \tag{2.1}$$

Here, the n_i represent arbitrary integers and the $\mathbf{a}_i$ do not all lie on the same plane. The equivalence of points $\mathbf{r}$ and $\mathbf{r}'$ in an infinite lattice make it clear that a single grouping of atoms, repeated throughout that entire crystal, will fill the lattice. This grouping is call a *unit cell.*

An example of a Bravais lattice is the face-centred cubic (FCC) lattice. This is one of the simplest and most common Bravais lattices known in nature. A single unit cell is shown in Figure (2.1). The primitive translation vectors of the FCC Bravais lattice are:

$$\begin{aligned} \mathbf{a}_1 &= \frac{A}{2}(\mathbf{j} + \mathbf{k}) \\ \mathbf{a}_2 &= \frac{A}{2}(\mathbf{k} + \mathbf{i}) \\ \mathbf{a}_3 &= \frac{A}{2}(\mathbf{i} + \mathbf{j}) \end{aligned} \tag{2.2}$$

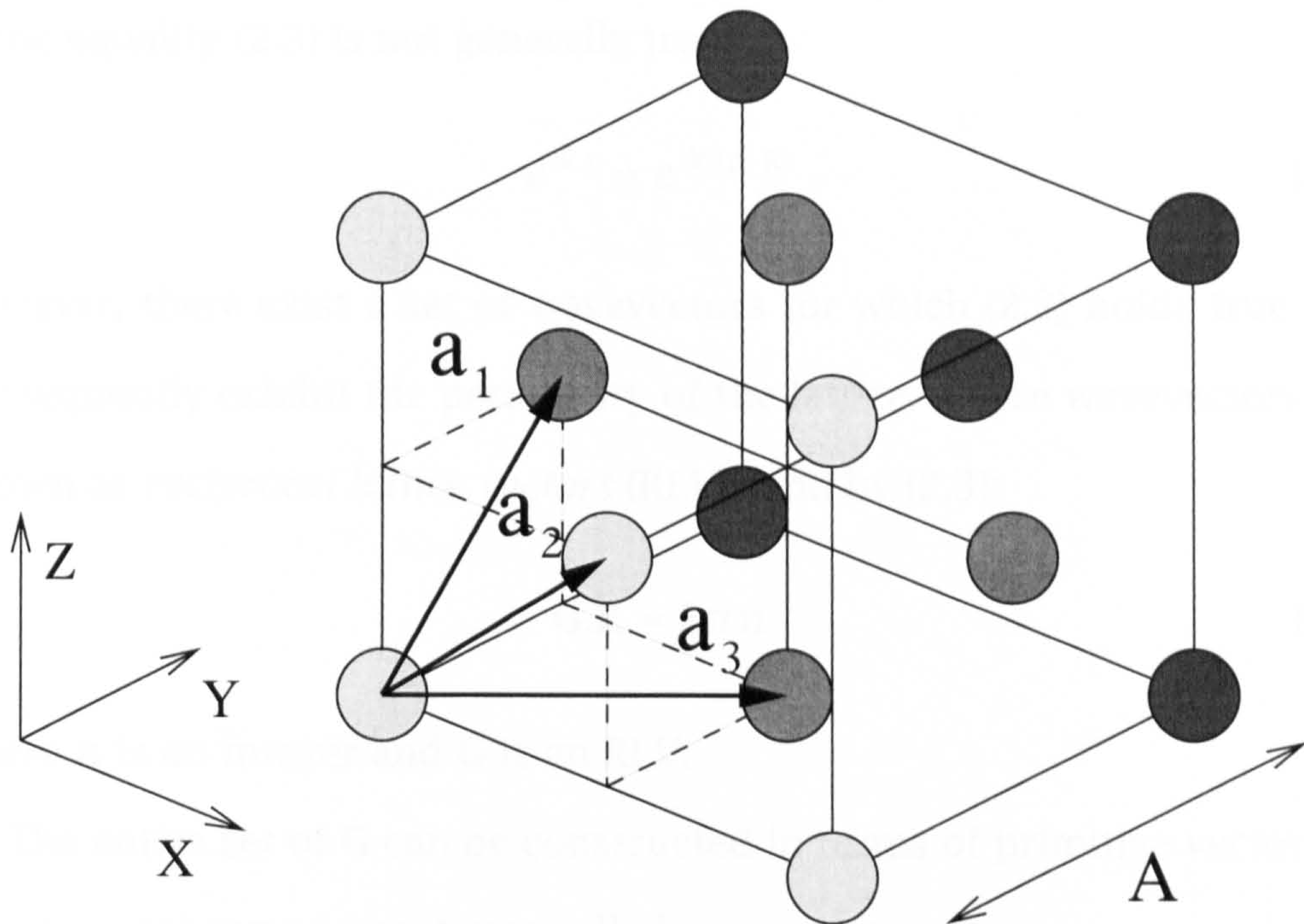

Figure 2.1: The Unit Cell of a Face Centred Cubic (FCC) Lattice.

where **i**, **j** and **k** represent orthonormal vectors along the Cartesian axes x, y and z respectively and A is defined as the lattice constant. The crystal lattice translation vector **R** of equation (2.1) define the Bravais lattice if the primitive vectors are defined correctly.

2.2 The Reciprocal Lattice

Consider a plane wave of some physical quantity propagating through a crystal. Consider also that the crystal is a Bravais lattice defined by (2.1). In general, the plane wave will not have the periodicity of the lattice. That

is the equality (2.3) is not generally true.

$$e^{i\mathbf{k}.\mathbf{r}} = e^{i\mathbf{k}.(\mathbf{r}+\mathbf{R})} \tag{2.3}$$

However, there exist a set of wavevectors for which (2.3) holds true and consequently exhibit the periodicity of the lattice. These wavevectors are known as *reciprocal lattice vectors* (RLV)s and by (2.3):

$$\mathbf{G}.\mathbf{R} = 2\pi n \tag{2.4}$$

where n is an integer and **G** is an RLV.

The entire set of **G** can be constructed in terms of primitive vectors $\mathbf{b}_i$ in *reciprocal space* (sometimes called momentum space):

$$\mathbf{G} = m_1\mathbf{b}_1 + m_2\mathbf{b}_2 + m_3\mathbf{b}_3 \tag{2.5}$$

and m_i are arbitrary integers.

Using equations (2.1), (2.4) and (2.5), the primitive vectors $\mathbf{b}_i$ can be generated from the primitive translation vectors $\mathbf{a}_i$:

$$\begin{aligned} \mathbf{b}_1 &= 2\pi\frac{\mathbf{a}_2 \times \mathbf{a}_3}{\mathbf{a}_1 \cdot (\mathbf{a}_2 \times \mathbf{a}_3)} \\ \mathbf{b}_2 &= 2\pi\frac{\mathbf{a}_3 \times \mathbf{a}_1}{\mathbf{a}_1 \cdot (\mathbf{a}_2 \times \mathbf{a}_3)} \\ \mathbf{b}_3 &= 2\pi\frac{\mathbf{a}_1 \times \mathbf{a}_2}{\mathbf{a}_1 \cdot (\mathbf{a}_2 \times \mathbf{a}_3)} \end{aligned} \tag{2.6}$$

and must satisfy the condition:

$$\mathbf{b}_i.\mathbf{a}_j = 2\pi\delta_{ij} \tag{2.7}$$

where δ_{ij} is the Kronecker delta, defined as:

$$\delta_{ij} = \begin{cases} 1 & \text{if } i = j \\ 0 & \text{if } i \neq j \end{cases} \tag{2.8}$$

One final note, if the $\mathbf{b}_i$ are evaluated for an FCC structure, it is found that they describe a body centred cubic (BCC) Bravais lattice: the reciprocal lattice of the Bravais lattice is itself a Bravais lattice.

2.3 Bloch Functions

F. Bloch proved the important theorem that the solutions of the Schrödinger equation for a periodic potential must be of a special form:

$$\psi_k(\mathbf{r}) = u_k(\mathbf{r}) \exp(i\mathbf{k} \cdot \mathbf{r}) \tag{2.9}$$

where $u_k(\mathbf{r})$ has the period of the crystal lattice such that

$$u_k(\mathbf{r}) = u_k(\mathbf{r} + \mathbf{R}) \tag{2.10}$$

Equations (2.9) and (2.10) express the Bloch theorem: The eigenfunctions of the wave equation for a periodic potential are the product of the plane wave $\exp(i\mathbf{k} \cdot \mathbf{r})$ and a function $u_k(\mathbf{r})$ exhibiting the periodicity of the crystal lattice.

A one-electron wavefunction of the form (2.9) is called a Bloch function and can always be decomposed into a sum of traveling waves. Bloch functions can be readily assembled into localised wave packets to represent electrons and holes that propagate through the potential field of the

ion cores. Bloch functions are therefore the ideal basis set for models such as the empirical pseudopotential method and the $\mathbf{k} \cdot \mathbf{p}$ model.

2.4 Energy Bands and the Brillouin Zone

We shall describe in detail later that the energy states that electrons and holes may assume in a periodic potential are the discrete solutions of an eigenvalues equation called the Schrödinger equation. However, the theory that we have already described has consequences that may be described independently of the anticipated solutions.

Recalling that equation (2.4) shows that

$$e^{i\mathbf{G}.\mathbf{R}} = 1, \tag{2.11}$$

it follows that two $\mathbf{k}$ vectors that differ by a RLV $\mathbf{G}$ label the same representation. Therefore, when we classify the eigenvalues of our problem, it is only necessary to consider those $\mathbf{k}$ vectors that differ in magnitude by amounts less than the magnitude of an RLV. If we then define a volume in reciprocal space that is the smallest region enclosed by bisecting the RLVs from the origin (in reciprocal space, labelled Γ) with perpendicular planes; it is clear that all of the $\mathbf{k}$ points inside this volume will differ in magnitude by values within the required range. This volume is termed the *first Brillouin zone.* Figure (2.2) depicts the first Brillouin zone for an FCC crystal and as can be seen, this zone is a truncated octahedron. There are various points labelled on this figure which are points of high symmetry such as the (0,0,1) and (1,1,1) points, known as the X and L points,

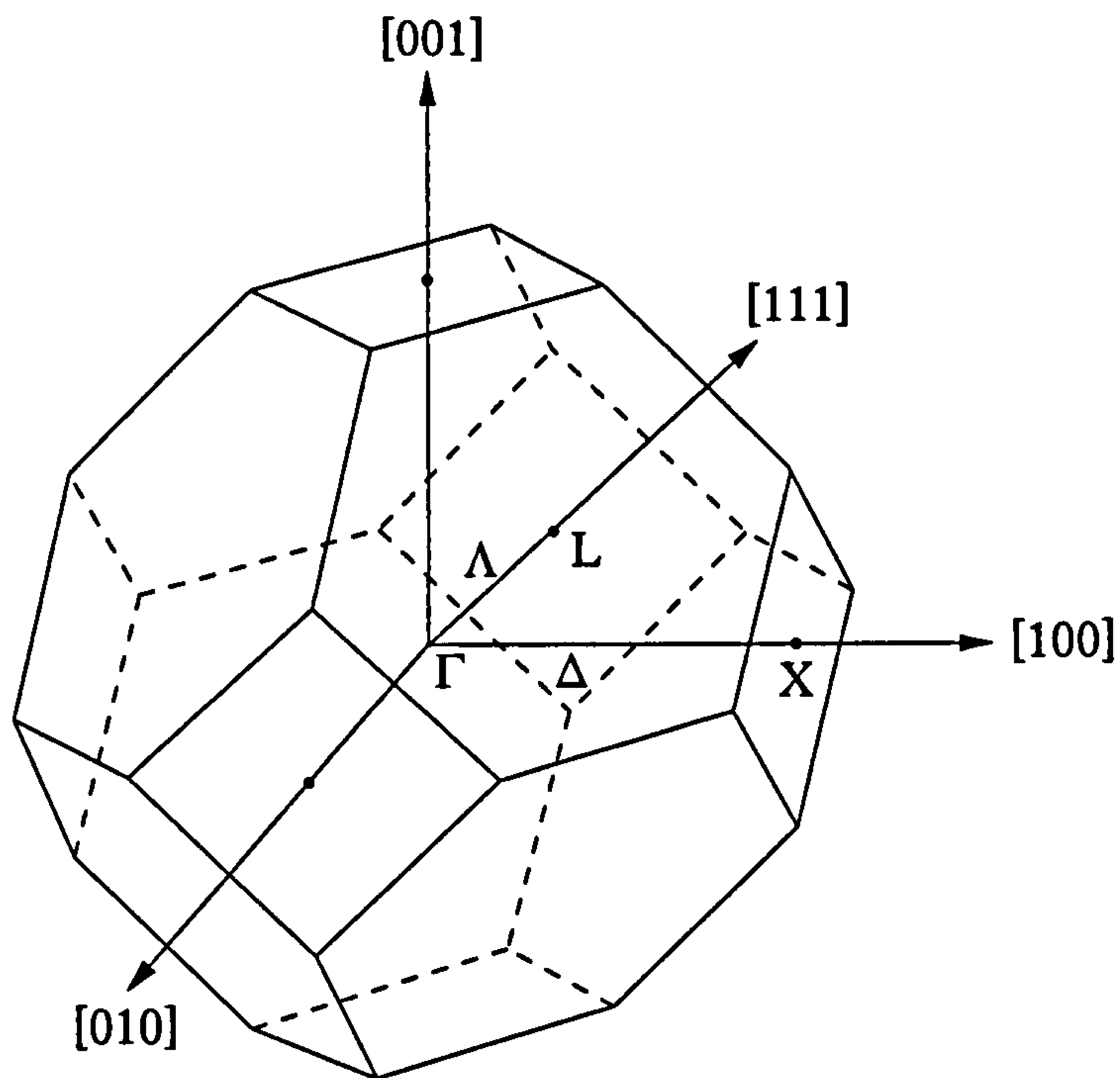

Figure 2.2: The First Brillouin Zone of an FCC Crystal.

respectively. There are, for example, six equivalent X points.

Further Brillouin zones (BBZ) can be constructed in a similar fashion by bisecting the next nearest RLVs with perpendicular planes. However, due to the equivalence of **k** points separated by RLVs **G**, an arbitrary wavevector **k**, in an BZ, may be alternatively expressed **k** + **G** by using the correct choice of **G** and where **k** now lies in the first BZ. This description accommodates a compact way of looking at the electron energy, E, versus the magnitude of the wavevector $|\mathbf{k}|$. Such a plot is known as a *reduced zone* dispersion curve. For each **k** point within the first BZ, then, there are an infinite number of electron eigensolutions that are indexed by n in the subsequent discussion. The eigensolutions, generally labelled by energies

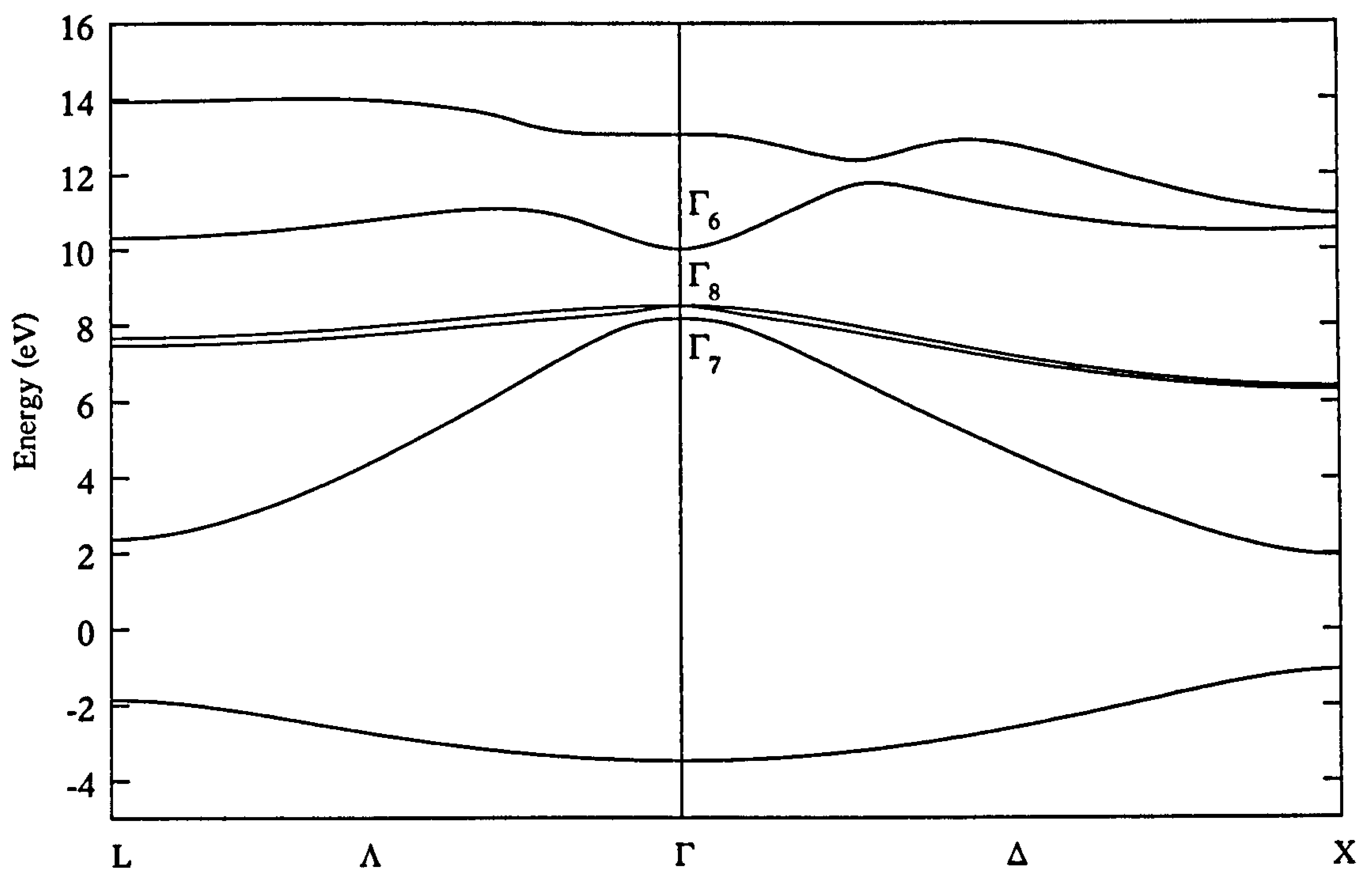

Figure 2.3: The band structure of GaAs

$E_{n\mathbf{k}}$ and wavefunctions $\psi_{n\mathbf{k}}$ comprise the *band structure* of the crystal.

The wave vector $\mathbf{k}$ of an electron is a manifestation of its wave-like properties, as was shown by de Broglie (Ashcroft and Mermin, 1976). It then follows that the valence electrons undergo Bragg reflection (Cohen, 1972) at the Brillouin zone boundaries leading to discontinuities in the electron energy spectrum at these values of $\mathbf{k}$. This then leads to the concept of *forbidden bands* in the electron energy spectrum. That is, there are bands of energies that an electron may not assume. The energy values above and below these forbidden bands are termed the *conduction band* and *valence band* respectively, and the range of forbidden energy values is termed the *band-gap*. It is the form of this *band structure* in a material

that determines it's electrical and optical properties and consequently its classification as either an insulator, semiconductor or metal. Though it should be noted that a semiconductor is merely an insulator with a small band-gap. The band structure calculated using the empirical pseudopotential for bulk GaAs is shown in Figure (2.3). Using the reduced zone representation, this band structure exhibits the energy bands at different **k** points along certain directions in the first BZ.

The *Hamiltonian* is the name given to the energy operator in the eigenvalue equation that determines the electronic band structure, the Schrödinger equation. Applying symmetry operations, there exist a set of wavevectors that map onto one another. As a consequence, only one fraction of the first BZ needs to be considered when looking at the band structure. This is manifested in the various degenerate energy bands that exist in a crystal based upon the FCC Bravais lattice. One such degeneracy can be seen on the band structure plot illustrated in Figure (2.3) where two of the bands, in this case the top two valence bands (the so-called heavy hole and light hole bands) are degenerate at Γ. The breaking of these degeneracies can be achieved by, for example, introducing strain into the crystal and therefore breaking the crystal symmetry.

2.5 Charge Carriers in Semiconductors

In order to gain an understanding of the optical and electronic properties of semiconductors we must gain insight into the energy distribution of

charge carriers. In an idealised semiconductor, in which all the electrons populate their lowest energy states, the valence band is completely full and there are no electrons occupying the conduction band. However, in theory, this situation may only arise when the temperature is at absolute zero. At realistic temperatures, the valence electrons can gain enough energy from the thermal motion of atoms to be excited up to the conduction band. When this occurs, there is a *hole* left in the valence band. This hole can act as a mobile positive charge carrier. This is because valence electrons from previously unionised atoms may flow between them, thus giving the overall impression of positive charges flowing throughout the valence band. These holes, then, may be considered as charge carriers in the valence band in the same way that electrons are considered charge carriers in the conduction band.

These electrons and holes then, are termed charge carriers and are the mediators of the electric current, under an applied potential, in these materials. A Rudimentary analysis of the dynamics of carriers in solids (Ashcroft and Mermin, 1976; Fraser, 1979) leads to the result that under the influence of an external force, such as an electric field, carriers exhibit an apparent mass that differs from that of the free electron mass. This mass has become known as the *effective mass*, m^* of the carrier and embodies the way in which interaction with the lattice potential modifies the carrier motion. Quantitatively, we may express the effective mass by (2.12) and (2.13)

$$m^* = \hbar(\nabla_{\mathrm{k}}^2 E)^{-1} \tag{2.12}$$

$$\nabla_{\mathbf{k}} = \frac{\partial}{\partial k_x}\mathbf{i} + \frac{\partial}{\partial k_y}\mathbf{j} + \frac{\partial}{\partial k_z}\mathbf{k} \tag{2.13}$$

The effective mass of the electron at the bottom of the conduction band is usually smaller, often considerably smaller, than that of the free-electron. Since the band curvature at the valence band maximum is of opposite sign to that of the conduction band, electrons occupying such states in the former band have a negative effective mass. Since, however, we generally consider holes near the top of the valence band, the hole effective mass, like it's charge, is positive because a hole's energy is greater at lower electron energies.

Chapter 3

Calculation of the Electronic Band Structure of Semiconductor Heterostructures

In order to predict the electronic and optical properties of semiconductor heterostructures it is necessary to know the electronic bandstructure and the corresponding wavefunction. This chapter contains details on how this information may be obtained using two key techniques and also the applicability of these methods to different semiconductor heterostructures.

3.1 Local Empirical Pseudopotential Theory

Empirical Pseudopotential Theory (EPT) has proved to be a very successful method for calculating a wide variety of properties relating to semiconductor heterostructures. Indeed, the success of this simple theory is most probably because it is atomistic, i.e. it includes the effects of periodicity or lack thereof, and also that it correctly reproduces the effect of the covalent bonds of III-V semiconductors on the electronic structure of crystals. Presented here is an overview of the formulation of EPT for bulk materials and a description of how the method may be extended to predict the electronic structure of self-assembled quantum dots.

3.1.1 Formulation of the Local Empirical Pseudopotential Method

The formulation of an effective method for calculating the bandstructure of a bulk crystal firstly has to overcome the problem of modeling the quickly varying part of the wavefunction in the proximity of the atomic nuclei. This problem is solved by recognising that the core electrons do not participate in the optical and electronic processes important for semiconductor devices. Therefore we will begin by expanding the wavefunction with two separate terms, one representing the valence states in terms of plane waves $|\mathbf{k}+\mathbf{G}\rangle$ and another representing the core states with an ex-

pansion of the eigenstates of atomic core electrons $|c\rangle$. However, first of all we must write down a time independent Schrödinger equation (TISE) that represents the operation of a Hamiltonian on the overall electron wavefunction.

$$\left[-\frac{\hbar^2}{2m}\nabla^2 + V(\mathbf{r})\right]\psi_{n\mathbf{k}} = E_{n\mathbf{k}}\psi_{n\mathbf{k}} \tag{3.1}$$

where, from the above discussion, the wavefunction is:

$$\psi_{n,\mathbf{k}}(\mathbf{r}) = \sum_{\mathbf{G}} a_{n,\mathbf{k}}(\mathbf{G})|\mathbf{k}+\mathbf{G}\rangle + \sum_{c} b_c|c\rangle \tag{3.2}$$

and Ω is the crystal volume. Thus substituting (3.2) into (3.1) we obtain:

$$\sum_{\mathbf{G}} a_{n,\mathbf{k}}(\mathbf{G})\left[-\frac{\hbar^2}{2m}\nabla^2 + V(\mathbf{r})\right]|\mathbf{k}+\mathbf{G}\rangle + \sum_{c}(E_c - E_n)b_c|c\rangle = E_n\sum_{\mathbf{G}} a_{n,\mathbf{k}}(\mathbf{G})|\mathbf{k}+\mathbf{G}\rangle \tag{3.3}$$

Here, E_c is the energy of the core state c. From the requirement that the core states be orthonormal to all the Bloch functions, we obtain:

$$\langle c'|n\mathbf{k}\rangle \equiv \sum_{\mathbf{G}} a_{n,\mathbf{k}}(\mathbf{G})\langle c'|\mathbf{k}+\mathbf{G}\rangle + \sum_{c}\langle c'|b_c|c\rangle = 0 \tag{3.4}$$

Since all core states are already orthogonal to themselves, (3.4) reduces to:

$$b_{c'} = -\sum_{\mathbf{G}} a_{n,\mathbf{k}}(\mathbf{G})\langle c'|\mathbf{k}+\mathbf{G}\rangle \tag{3.5}$$

Therefore, substituting (3.5) into (3.3) yields a pseudo-TISE:

$$\left[-\frac{\hbar^2}{2m}\nabla^2 + W(\mathbf{r})\right]\phi_{n,\mathbf{k}}(\mathbf{r}) = E_{n,\mathbf{k}}\phi_{n,\mathbf{k}}(\mathbf{r}) \tag{3.6}$$

with a pseudopotential:

$$W(\mathbf{r}) = V(\mathbf{r}) + \sum_{c}(E_c - E_n)b_c|c\rangle\langle c'| \tag{3.7}$$

and a pseudo-wavefunction:

$$\phi_{n,\mathbf{k}}(\mathbf{r}) = \sum_{\mathbf{G}} a_{n,\mathbf{k}}(\mathbf{G})|\mathbf{k}+\mathbf{G}\rangle \tag{3.8}$$

3.1.2 Representation of Bulk Materials

It can be seen from (3.7) that the pseudopotential consists of two parts, an attractive Comloub term and a repulsive term arising from the interaction of the valence electrons with the core. Clearly there will be some cancellation between these two terms and that consequently the pseudopotential will be weaker than any individual component. Also the pseudopotential is an energy-dependent non-local function that requires a self-consistent approach to solve exactly. However, we shall approximate it with an energy-independent, local function, $W_L(\mathbf{r})$, as first used by Cohen and Bergstesser, (1966). This allows us to represent the crystal potential with a sum of spherically symmetric local pseudopotentials centred on atomic sites:

$$W_L(\mathbf{r}) = \sum_{j,\tau_j} \sum_{\mathbf{R}} \omega_j(\mathbf{r} - \mathbf{R} - \tau_j) \tag{3.9}$$

Where the basis site, τ_j is the position of the jth atom type at the lattice point R that constitutes the crystal and $\omega_j(\mathbf{r} - \mathbf{R} - \tau_j)$ is the spherically symmetric local pseudopotential centred on that site.

All we now require therefore, is to solve the one electron Schrödinger equation using the pseudopotential and pseudo-wavefunctions. Thus substituting (3.8) into (3.6) yields:

$$\left[-\frac{\hbar^2}{2m}\nabla^2 + W(\mathbf{r})\right] \sum_{\mathbf{G}} a_{n,\mathbf{k}}(\mathbf{G})|\mathbf{k}+\mathbf{G}\rangle = E_{n,\mathbf{k}} \sum_{\mathbf{G}} a_{n,\mathbf{k}}(\mathbf{G})|\mathbf{k}+\mathbf{G}\rangle \tag{3.10}$$

Operating on (3.10) with $\langle \mathbf{k}+\mathbf{G}'|$ and converting to atomic units we arrive at:

$$\frac{1}{2}|\mathbf{k}+\mathbf{G}'|^2 a_{n\mathbf{k}}(\mathbf{G}') + \sum_{\mathbf{G}\mathbf{G}'} \langle \mathbf{k}+\mathbf{G}'|W(\mathbf{r})|\mathbf{k}+\mathbf{G}\rangle = E_{n\mathbf{k}} a_{n\mathbf{k}}(\mathbf{G}') \qquad (3.11)$$

In order to evaluate (3.11) we must calculate the integral term involving the pseudopotential. Explicitly:

$$\langle \mathbf{k}+\mathbf{G}'|W_L(\mathbf{r})|\mathbf{k}+\mathbf{G}\rangle = \frac{1}{\Omega}\int_{\Omega} e^{-i(\mathbf{k}+\mathbf{G}').\mathbf{r}} W_L(\mathbf{r}) e^{i(\mathbf{k}+\mathbf{G}).\mathbf{r}} d^3\mathbf{r} \qquad (3.12)$$

Substituting (3.9) for $W_L(\mathbf{r})$

$$\langle \mathbf{k}+\mathbf{G}'|W_L(\mathbf{r})|\mathbf{k}+\mathbf{G}\rangle = \frac{1}{\Omega}\int_{\Omega} e^{i(\mathbf{G}-\mathbf{G}').\mathbf{r}} \sum_{j,\tau_j}\sum_{\mathbf{R}} \omega_j(\mathbf{r}-\mathbf{R}-\tau_j) d^3\mathbf{r} \qquad (3.13)$$

Changing the variable of integration from $\mathbf{r}$ to $\mathbf{r}' + \mathbf{R} + \tau_j$ and relabelling $\mathbf{r}'$ as $\mathbf{r}$ (since both $\mathbf{r}'$ and $\mathbf{r}$ are integrated over infinity) we obtain :-

$$\langle \mathbf{k}+\mathbf{G}'|W_L(\mathbf{r})|\mathbf{k}+\mathbf{G}\rangle = \frac{1}{\Omega}\sum_{j,\tau_j}\sum_{\mathbf{R}}\int_{\Omega} e^{i(\mathbf{G}-\mathbf{G}').(\mathbf{r}+\mathbf{R}+\tau_j)} \omega_j(\mathbf{r}) d^3\mathbf{r} \qquad (3.14)$$

which may be factorised:-

$$\langle \mathbf{k}+\mathbf{G}'|W_L(\mathbf{r})|\mathbf{k}+\mathbf{G}\rangle = \frac{1}{\Omega}\sum_{\mathbf{R}} e^{i(\mathbf{G}-\mathbf{G}').\mathbf{R}} \sum_{j,\tau_j} e^{i(\mathbf{G}-\mathbf{G}').\tau_j} \int_{\Omega} e^{i(\mathbf{G}-\mathbf{G}').\mathbf{r}} \omega_j(\mathbf{r}) d^3\mathbf{r} \qquad (3.15)$$

If we consider a crystal volume of N unit cells, the total crystal volume can therefore be written as $\Omega = N\Omega_0$ where Ω_0 is the volume of a single bulk unit cell. Also, by definition $\sum_{\mathbf{R}} e^{i(\mathbf{G}-\mathbf{G}').\mathbf{R}} = N$, the total number of bulk unit cells. Thus (3.15) becomes:

$$\langle \mathbf{k}+\mathbf{G}'|W_L(\mathbf{r})|\mathbf{k}+\mathbf{G}\rangle = \frac{1}{\Omega_o}\sum_{j,\tau_j} e^{i(\mathbf{G}-\mathbf{G}').\tau_j} \int_{\Omega} e^{i(\mathbf{G}-\mathbf{G}').\mathbf{r}} \omega_j(\mathbf{r}) d^3\mathbf{r} \qquad (3.16)$$

We then make the final substitution:

$$\langle \mathbf{k} + \mathbf{G}' | W_L(\mathbf{r}) | \mathbf{k} + \mathbf{G} \rangle = \frac{1}{2} \sum_{j,\tau_j} e^{i(\mathbf{G}-\mathbf{G}').\tau_j} \omega_j(\mathbf{G} - \mathbf{G}') \tag{3.17}$$

where,

$$\omega_j(\mathbf{G} - \mathbf{G}') = \frac{2}{\Omega_o} \int_{\Omega} e^{i(\mathbf{G}-\mathbf{G}').\mathbf{r}} \omega_j(\mathbf{r}) d^3\mathbf{r} \tag{3.18}$$

By this method, $\omega_j(\mathbf{G} - \mathbf{G}')$ becomes the *empirical* parameter and has the additional benefit of including the normalisation for the potential. Thus, in order to fit a bulk bandstructure, $\omega_j(\mathbf{G} - \mathbf{G}')$ is varied until several experimentally measured band-gaps are correctly reproduced. Usually six Fourier components and a basis set of about sixty five plane waves are enough to reproduce the bulk bandstructure without spin-orbit coupling (Vinsome, 1971). This method of calculation requires that the matrix created by (3.11) is diagonalised fully. The implication of this is that the computational effort scales as the cube of the number of plane waves in the basis set.

3.1.3 Representation of Supercells by the Empirical Pseudopotential Method

In the past, electronic structure calculations of semiconductor heterostructures have been performed using a basis set consisting of bulk wavefunctions.

$$\psi_{N\mathbf{K}} = \sum_{n\mathbf{k}} A^N_{n\mathbf{k}} \phi_{n\mathbf{k}} = \sum_{n\mathbf{k}} A^N_{n\mathbf{k}} \sum_{\mathbf{G}} a_{n,\mathbf{k}}(\mathbf{G}) | \mathbf{k} + \mathbf{G} \rangle \tag{3.19}$$

Where $\phi_{n\mathbf{k}}$ is defined by (3.8) and $\mathbf{k}$ the momentum of the bulk wavefunction is a function of $\mathbf{K}$ the supercell (or superlattice) momentum. The

number of **k**-points included in the expansion set is governed by the number of superlattice reciprocal lattice vectors in the first bulk Brillouin zone. The bulk wavefunctions $\phi_{n\mathbf{k}}$ represent the so-called host material, though this does not necessarily have the same meaning here as it does in experimental terms, that is the assignment of host or dopant is arbitrary. The second material (dopant) is included in the calculation by using a perturbation potential. This perturbation potential represents the difference between the host and dopant bulk potentials. Thus the perturbation is a small potential where the host material has been replaced by the dopant material and zero where the host remains. The perturbation potential is defined:-

$$V_p(\mathbf{r}) = \sum_R \left[\sum_{i\tau_j} V_i(\mathbf{r} - \mathbf{R} - \tau_i) - \sum_{j\alpha_j} V_j(\mathbf{r} - \mathbf{R} - \alpha_j) \right] \tag{3.20}$$

where $i(j)$ indexes the dopant (host) material type, $\tau_i(\alpha_j)$ are the positions of the atoms in material $i(j)$ and $V_{i(j)}$ are the potentials of material $i(j)$. Thus with the bulk Hamiltonian H_0 defined by (3.6), $V_p(\mathbf{r})$ by (3.20) and the perturbed wavefunction by (3.19), the TISE for the heterostructure is:-

$$\begin{aligned} [H_0 + V_p(\mathbf{r})] \sum_{n\mathbf{k}} A^N_{n\mathbf{k}} \phi_{n\mathbf{k}} &= E_{N\mathbf{K}} \sum_{n\mathbf{k}} A^N_{n\mathbf{k}} \phi_{n\mathbf{k}} \\ [H_0 + V_p(\mathbf{r})] \sum_{n\mathbf{k}} A^N_{n\mathbf{k}} |n\mathbf{k}\rangle &= E_{N\mathbf{K}} \sum_{n\mathbf{k}} A^N_{n\mathbf{k}} |n\mathbf{k}\rangle \\ [H_0 + V_p(\mathbf{r})] \sum_{n\mathbf{k}} A^N_{n\mathbf{k}} \sum_{\mathbf{G}} a_{n,\mathbf{k}}(\mathbf{G}) |\mathbf{k}+\mathbf{G}\rangle &= E_{N\mathbf{K}} \sum_{n\mathbf{k}} A^N_{n\mathbf{k}} \sum_{\mathbf{G}} a_{n,\mathbf{k}}(\mathbf{G}) |\mathbf{k}+\mathbf{G}\rangle \end{aligned} \tag{3.21}$$

We can then use a similar line of reasoning as was used in Section 3.1.2 (i.e. multiply by $\langle n'\mathbf{k}'|$) and arrive at

$$(E_{n'\mathbf{k}'} - E_{N\mathbf{K}})A^N_{n'\mathbf{k}'} + \sum_{n\mathbf{k}} A^N_{n\mathbf{k}} \langle n'\mathbf{k}'|V_p|n\mathbf{k}\rangle = 0 \tag{3.22}$$

where

$$\langle n'\mathbf{k}'|V_p(\mathbf{r})|n\mathbf{k}\rangle = \sum_{\mathbf{G}\mathbf{G}'} a^*_{n',\mathbf{k}'}(\mathbf{G}')a_{n,\mathbf{k}}(\mathbf{G})\langle \mathbf{k}' + \mathbf{G}'|V_p(\mathbf{r})|\mathbf{k} + \mathbf{G}\rangle \tag{3.23}$$

and

$$\langle \mathbf{k}' + \mathbf{G}'|V_p(\mathbf{r})|\mathbf{k} + \mathbf{G}\rangle = \sum_{i\tau_i} e^{i\mathbf{g}.\tau_i} v_i(\mathbf{g}) - \sum_{j\alpha_j} e^{i\mathbf{g}.\alpha_j} v_j(\mathbf{g}) \tag{3.24}$$

and finally

$$v_{i(j)}(\mathbf{g}) = \frac{1}{\Omega_o}\int_\Omega e^{i\mathbf{g}.\mathbf{r}} V_{i(j)}(\mathbf{r}) \tag{3.25}$$

The reciprocal lattice vector of the supercell, $\mathbf{g}$ is a consequence of $\mathbf{k} - \mathbf{k}' + \mathbf{G} - \mathbf{G}' = \mathbf{g}$ by definition.

This method has been very successful in calculating the electronic structure of superlattices with a single growth direction because of the relatively small size of the supercell. However, the calculation of (3.24) becomes unfeasible because of its non-linear dependence on N, the number of units in the supercell.

3.2 $\mathbf{k} \cdot \mathbf{p}$ Theory for Self-assembled Quantum Dots

The most important regions of the band structure are those most populated by the charge carriers of the crystal. For optical devices this region

is the bottom of the conduction band and the top of the valence band. In addition, a quantum dot has a unit cell so large that the first Brillouin zone is very small and consequently can be well represented by an expansion of bulk wavefunctions at the Γ symmetry point (i.e. the centre of the Brillouin zone). Given these two ideas it is realised that the $\mathbf{k} \cdot \mathbf{p}$ method (Kane, 1966) will provide an ideal theory for calculating electronic and optical properties of self-assembled quantum dots.

3.2.1 The Kane Model

For a direct bandgap semiconductor we can obtain solutions in the immediate vicinity of the Brillouin zone centre if the solution to the one electron Schrödinger equation is known at the zone centre. To do this we regard the scalar product $\mathbf{k} \cdot \mathbf{p}$ (where $\mathbf{k}$ is a wavevector measured from Γ and $\mathbf{p} = -i\hbar\nabla$) as a perturbation.

We therefore write the TISE (3.1) in terms of the periodic part of the Bloch function.

$$Hu_{\mathbf{k}}(\mathbf{r}) = \left[H_0 + V^{so} + \frac{\hbar}{m_0}\mathbf{k} \cdot \mathbf{p} + \frac{\hbar^2 k^2}{2m_0}\right] u_{\mathbf{k}}(\mathbf{r}) = E_{\mathbf{k}} u_{\mathbf{k}}(\mathbf{r}) \tag{3.26}$$

where H_0 is the zone centre Hamiltonian and V^{so} is the spin-orbit potential. We then decide to divide the band edges states into two classes, A and B. The states of interest (close to the band edges e.g. $\Gamma_6, \Gamma_8, \Gamma_7$ in GaAs) are put into class A and every other band into class B. We then realise that our most simple unperturbed basis functions are the 8 band edge Bloch functions i.e. $|S\uparrow\rangle, |X\uparrow\rangle, |Y\uparrow\rangle, |Z\uparrow\rangle, |S\downarrow\rangle, |X\downarrow\rangle, |Y\downarrow\rangle$ and $|Z\downarrow\rangle$. However,

u_i	$\lvert J, J_z\rangle$	ψ_{J,J_z}
u_1	$\lvert\frac{1}{2},\frac{1}{2}\rangle$	$i\lvert S\uparrow\rangle$
u_3	$\lvert\frac{3}{2},\frac{1}{2}\rangle$	$-\sqrt{\frac{2}{3}}\lvert Z\uparrow\rangle+\frac{1}{\sqrt{6}}\lvert(X+iY)\downarrow\rangle$
u_5	$\lvert\frac{3}{2},\frac{3}{2}\rangle$	$\frac{1}{\sqrt{2}}\lvert(X+iY)\uparrow\rangle$
u_7	$\lvert\frac{1}{2},\frac{1}{2}\rangle$	$\frac{1}{\sqrt{3}}\lvert(X+iY)\downarrow\rangle+\frac{1}{\sqrt{3}}\lvert Z\uparrow\rangle$
u_2	$\lvert\frac{1}{2},-\frac{1}{2}\rangle$	$i\lvert S\downarrow\rangle$
u_4	$\lvert\frac{3}{2},-\frac{1}{2}\rangle$	$\frac{1}{\sqrt{6}}\lvert(X-iY)\uparrow\rangle+\sqrt{\frac{2}{3}}\lvert Z\downarrow\rangle$
u_6	$\lvert\frac{3}{2},-\frac{3}{2}\rangle$	$\frac{1}{\sqrt{2}}\lvert(X-iY)\downarrow\rangle$
u_8	$\lvert\frac{1}{2},-\frac{1}{2}\rangle$	$\frac{1}{\sqrt{3}}\lvert(X-iY)\uparrow\rangle+\frac{1}{\sqrt{3}}\lvert Z\downarrow\rangle$

Table 3.1: The Set of Linear Combinations of Unperturbed Basis Functions used in the $\mathbf{k}\cdot\mathbf{p}$ Formulation

of the terms in the Hamiltonian of (3.26) only H_0 and $\frac{\hbar^2k^2}{2m_0}$ are diagonal. and that it would be convenient if V^{so} was also diagonal. Therefore Kane chose a basis set made of linear combinations of the above functions. This basis was chosen such that the total angular momentum $\mathbf{J}=\mathbf{L}+\mathbf{S}$ and it's projection J_z along the z-axis are diagonal in the new basis. We therefore arrive at the basis functions in Table 3.1.

Now we will return to our classification of the two classes of eigenvalues and by using the perturbation method of Löwdin, (1951) the states in

B are treated as a perturbation on those in A. Formally:

$$u_{\mathbf{k}}(\mathbf{r}) = \sum_{j'}^{A} a_{j',\mathbf{k}} u_{j',0}(\mathbf{r}) + \sum_{\gamma'}^{B} a_{\gamma',\mathbf{k}} u_{\gamma',0}(\mathbf{r}) \tag{3.27}$$

where j' are the states in class A and γ' are the states in class B. Löwdins method requires that we solve on the TISE

$$\sum_{j'}^{A} (U_{jj'}^{A} - E\delta_{jj'}) a_{j',\mathbf{k}} = 0 \tag{3.28}$$

instead of

$$\sum_{j'}^{A,B} (H_{jj'} - E\delta_{jj'}) a_{j',\mathbf{k}} = 0 \tag{3.29}$$

To first order we can write the Hamiltonian $U_{jj'}^{A}$ in terms of the true Hamiltonian $H_{jj'}$

$$\begin{aligned} U_{jj'}^{A} &= H_{jj'} + \sum_{\gamma \neq j,j'}^{B} \frac{H_{j\gamma} H_{\gamma j'}}{E_0 - E_\gamma} \\ H_{jj'} &= \langle u_{j,0} | H | u_{j',0} \rangle = \left[E_j(0) + \frac{\hbar^2 k^2}{2m_0} \right] \delta_{jj'} + \sum_{\alpha = x,y,z} \frac{\hbar k_\alpha}{m_0} p_{jj'}^{\alpha} \quad (j, j' \in A) \\ H_{j\gamma} &= \langle u_{j,0} | \frac{\hbar}{m_0} \mathbf{k} \cdot \mathbf{p} | u_{\gamma,0} \rangle = \sum_{\alpha = x,y,z} \frac{\hbar k_\alpha}{m_0} p_{j\gamma}^{\alpha} \quad (j \in A, \gamma \notin A) \end{aligned} \tag{3.30}$$

We therefore arrive at

$$U_{jj'}^{A} = \left[E_j(0) + \frac{\hbar^2 k^2}{2m_0} \right] \delta_{jj'} + \sum_{\alpha = x,y,z} \frac{\hbar k_\alpha}{m_0} p_{jj'}^{\alpha} + \frac{\hbar^2}{m_0} \sum_{\gamma \neq j,j'} \sum_{\alpha,\beta} \frac{k_\alpha k_\beta p_{j\gamma}^{\alpha} p_{\gamma j'}^{\beta}}{E_0 - E_\gamma} \tag{3.31}$$

We shall now relabel $U_{jj'}^{A}$ as $D_{jj'}$ and simplify (3.31) to the form

$$D_{jj'} = E_{j'}(0) \delta_{jj'} + \sum_{\alpha = x,y,z} \frac{\hbar k_\alpha}{m_0} p_{jj'}^{\alpha} + \sum_{\alpha,\beta} D_{jj'}^{\alpha\beta} k_\alpha k_\beta \tag{3.32}$$

where we define $D_{jj'}^{\alpha\beta}$ as

$$D_{jj'}^{\alpha\beta} = \frac{\hbar^2}{2m_0} \left[\delta_{jj'} \delta_{\alpha\beta} + \sum_{\gamma}^{B} \frac{p_{j\gamma}^{\alpha} p_{\alpha j'}^{\beta} + p_{j\gamma}^{\beta} p_{\gamma j'}^{\alpha}}{m_0 (E_0 - E_\gamma)} \right] \tag{3.33}$$

Therefore in order to solve the TISE given by (3.28) we require the matrix elements as defined by (3.32) and (3.33) where the effects of $V(\mathbf{r})$ are incorporated into the momentum matrix elements $p_{jj'}$. However, at this point the calculation of the eigenstates of interest is actually more complex and time consuming than simply calculating all the eigenstates i.e. solve (3.29) directly. So, in order to proceed we must try to simplify the treatment of (3.33).

We will now explicitly define those eigenstates that are of interest. In this case the top four valence bands i.e. the heavy and light hole bands which are both spin degenerate. We therefore place these valence states into class A and all other bands (including the conduction band and valence band) into class B. Now, to simplify (3.33) we define

$$
\begin{aligned}
A_0 &= \frac{\hbar^2}{2m_0} + \frac{\hbar^2}{2m_0^2}\sum_{\gamma}^{B}\frac{p^x_{X\gamma}p^x_{\gamma X}}{E_0 - E_\gamma} \\
B_0 &= \frac{\hbar^2}{2m_0} + \frac{\hbar^2}{m_0^2}\sum_{\gamma}^{B}\frac{p^y_{X\gamma}p^y_{\gamma X}}{E_0 - E_\gamma} \\
C_0 &= \frac{\hbar^2}{m_0^2}\sum_{\gamma}^{B}\frac{p^x_{X\gamma}p^y_{\gamma X} + p^y_{X\gamma}p^x_{\gamma X}}{E_0 - E_\gamma} \qquad (3.34)
\end{aligned}
$$

and also define the Luttinger parameters $\gamma_1, \gamma_2, \gamma_3$ (Luttinger and Kohn, 1955; Luttinger, 1956) in terms of (3.34)

$$
\begin{aligned}
\gamma_1 &= -\frac{2m_0}{3\hbar^2}(A_0 + 2B_0) \\
\gamma_2 &= -\frac{m_0}{3\hbar^2}(A_0 - B_0) \\
\gamma_3 &= -\frac{m_0}{3\hbar^2}C_0 \qquad (3.35)
\end{aligned}
$$

This now gives us an empirical parameter to simplify the calculation of the matrix elements as the Luttinger parameters can be related to the ex-

perimentally measured effective masses of a bulk crystal by the relations (Gershoni *et al*, 1993)

$$\begin{aligned}
\frac{m_0}{m_{hh}^{[001]}} &= \gamma_1 - 2\gamma_2 \\
\frac{m_0}{m_{lh}^{[001]}} &= \gamma_1 + 2\gamma_2 \\
\frac{m_0}{m_{hh}^{[111]}} &= \gamma_1 - 2\gamma_3 \\
\frac{m_0}{m_{lh}^{[111]}} &= \gamma_1 + 2\gamma_3
\end{aligned} \tag{3.36}$$

So by combining (3.32) (3.34) and (3.35) and in the basis defined by Table 3.1 we arrive at the Luttinger-Kohn Hamiltonian (Luttinger and Kohn, 1955) denoted by $\overline{\overline{\mathbf{H}}}^{LK}$.

$$\overline{\overline{\mathbf{H}}}^{LK} = \begin{bmatrix} -P-Q & S & -R & 0 \\ & -P+Q & 0 & -R \\ & & -P+Q & -S \\ & & & -P-Q \end{bmatrix} \begin{matrix} \left|\frac{3}{2},\frac{3}{2}\right\rangle \\ \left|\frac{3}{2},\frac{1}{2}\right\rangle \\ \left|\frac{3}{2},-\frac{1}{2}\right\rangle \\ \left|\frac{3}{2},-\frac{3}{2}\right\rangle \end{matrix}$$

where the elements of the matrix are defined by

$$\begin{aligned}
P &= \frac{\hbar^2}{2m_0}\gamma_1(k_x^2 + k_y^2 + k_z^2) \\
Q &= \frac{\hbar^2}{2m_0}\gamma_2(k_x^2 + k_y^2 - 2k_z^2) \\
R &= \frac{\hbar^2}{2m_0}\sqrt{3}\left[-\gamma_2(k_x^2 - k_y^2) + 2i\gamma_3 k_x k_y\right] \\
S &= \frac{\hbar^2}{2m_0}2\sqrt{3}\gamma_3(k_x - ik_y)k_z
\end{aligned} \tag{3.37}$$

The eigenvalues and eigenvector of the Luttinger-Kohn Hamiltonian then, gives us the approximate solution to (3.1). Where the eigenvalue is given

by $E_{n,\mathbf{k}} = E$ the wavefunction has been defined as

$$\psi_{n,\mathbf{k}}(\mathbf{r}) = e^{i\mathbf{k}\cdot\mathbf{r}} u_{n,\mathbf{k}}(\mathbf{r}) \tag{3.38}$$

$$u_{n,\mathbf{k}}(\mathbf{r}) = \sum_{j=1}^{4} a_{j,\mathbf{k}} u_{j,0}(\mathbf{r}) \tag{3.39}$$

3.2.2 Strain Effects on Band Structures

The introduction of homogeneous strain in a bulk semiconductor changes the lattice parameter and in some cases, the symmetry of the material. These in turn produce significant changes in the electronic band structure. Homogeneous strained configuration can quite generally be divided into two configurations: the isotropic or hydrostatic component, that gives rise to a volume change without disturbing the crystal symmetry, and the anisotropic component that in general reduces the symmetry present in the strain-free lattice. A homogeneous strain induces change in energy gaps and, when the symmetry of the crystal is reduced, removes degeneracies.

In this section then, the effects of a uniform deformation on the conduction and valence band edges of III-V semiconductors at Γ are reviewed. The additional terms to be added to the one electron Schrödinger equation (3.1) to account for strain in bulk semiconductors are discussed using the language of the $\mathbf{k} \cdot \mathbf{p}$ scheme.

As shown in Figure (3.1), the unit vectors **a**,**b**, (and **c**) in the undeformed crystal are related to **a'**, **b'** (and **c'** in the uniformly deformed crystal by (3.40).

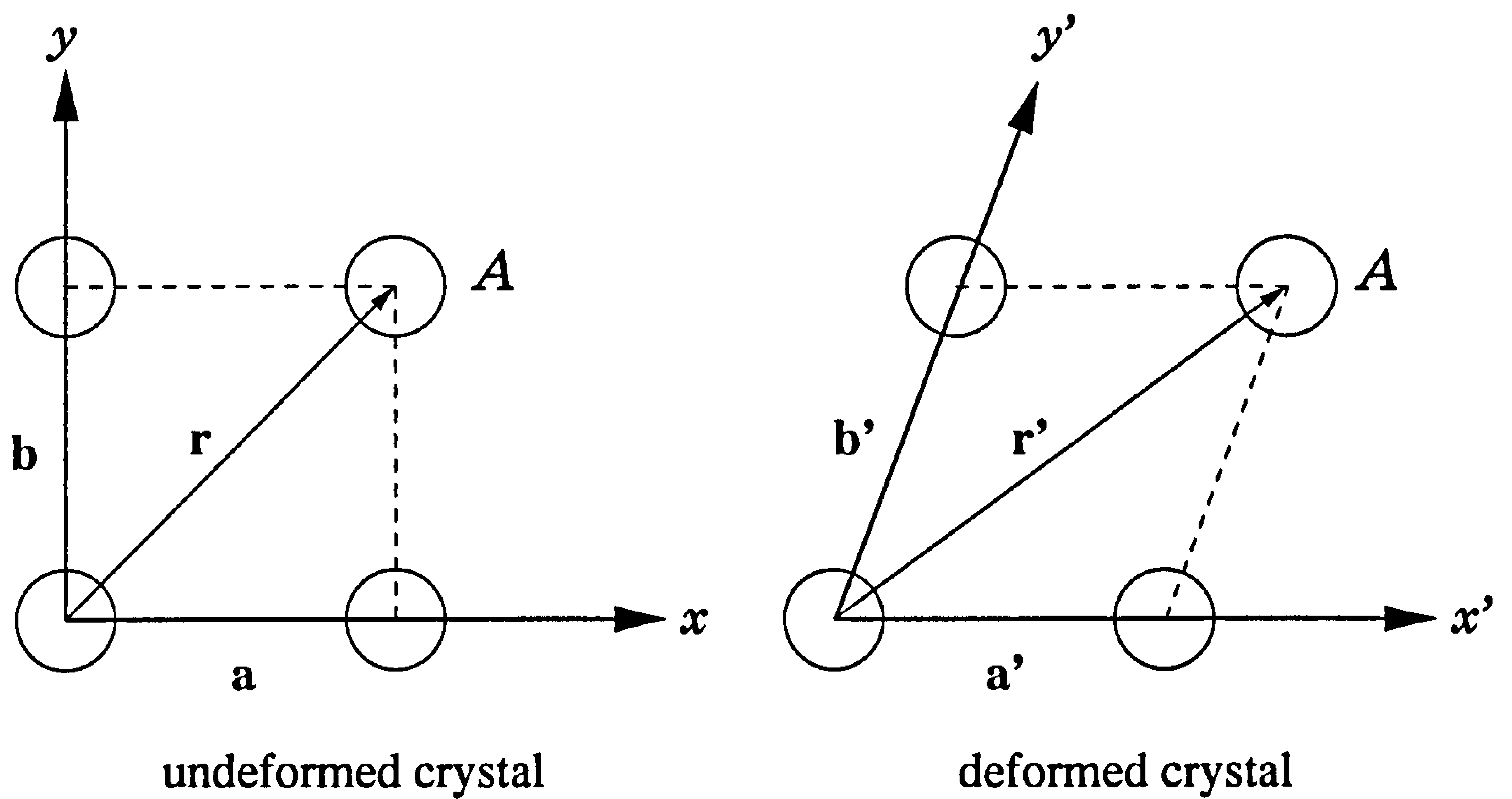

Figure 3.1: Axes of a crystal under uniform deformation.

$$\begin{aligned} \mathbf{a}' &= (1-\epsilon_{xx})\mathbf{a} + \epsilon_{xy}\,\mathbf{b} + \epsilon_{xz}\,\mathbf{c} \\ \mathbf{b}' &= \epsilon_{yx}\,\mathbf{a} + (1-\epsilon_{yy})\mathbf{b} + \epsilon_{yz}\,\mathbf{c} \\ \mathbf{c}' &= \epsilon_{zx}\,\mathbf{a} + \epsilon_{zy}\,\mathbf{b} + (1-\epsilon_{zz})\mathbf{c} \end{aligned} \tag{3.40}$$

We assume a homogeneous strain and a symmetric strain tensor i.e. $\epsilon_{xy} = \epsilon_{yx}$. For a cubic crystal under these conditions there are six independent, non-zero, components of the strain tensor. These are:-

$$\epsilon_{xx}, \epsilon_{yy}, \epsilon_{zz}, \epsilon_{xy} = \epsilon_{yx}, \epsilon_{yz} = \epsilon_{zy}, \epsilon_{zx} = \epsilon_{xz} \tag{3.41}$$

To label a position A (or atom A) in the undeformed crystal, we have

$$\mathbf{r} = x\mathbf{a} + y\mathbf{b} + z\mathbf{c} \tag{3.42}$$

The same atom in the deformed crystal can be labelled either as

$$\mathbf{r}' = x\mathbf{a}' + y\mathbf{b}' + z\mathbf{c}' \tag{3.43}$$

using the new basis vectors $\mathbf{a}', \mathbf{b}', \mathbf{c}'$ or as

$$\mathbf{r}' = x'\mathbf{a} + y'\mathbf{b} + z'\mathbf{c} \tag{3.44}$$

in the original basis of the deformed crystal. In the linear strain regime, the change of volume becomes:-

$$\frac{V + \delta V}{V} \approx \mathbf{a} \cdot \mathbf{b}' \times \mathbf{c}' = 1 + (\epsilon_{xx} + \epsilon_{yy} + \epsilon_{zz}) \tag{3.45}$$

The quantity $\epsilon_{xx} + \epsilon_{yy} + \epsilon_{zz}$ is the trace of the strain matrix $\bar{\bar{\epsilon}}$, or $Tr(\bar{\bar{\epsilon}})$, that is approximately the fractional change of the volume $\delta V/V$ of the crystal under uniform deformation:

$$\frac{\delta V}{V} \approx \epsilon_{xx} + \epsilon_{yy} + \epsilon_{zz} \tag{3.46}$$

The effect of a strain on the conduction band of a III-V semiconductor is to produce a hydrostatic energy shift proportional to the fractional volume change given by:

$$H_\epsilon^c = a_c(\epsilon_{xx} + \epsilon_{yy} + \epsilon_{zz}) \tag{3.47}$$

where a_c is the intraband (absolute) hydrostatic deformation potential of the conduction band. In the valence band, the orbital-strain Hamiltonian $H_\epsilon^v)$ can be written

$$H_\epsilon^v) = -a(\epsilon_{xx}+\epsilon_{yy}+\epsilon_{zz})-3b\left[\left(L_x^2 - \frac{1}{3}\mathbf{L}^2\right) + c.p.\right]-\frac{6d}{\sqrt{3}}[\{L_xL_y\}\epsilon_{xy}+c.p.] \tag{3.48}$$

Material	a_c	a	b	d
GaSb	-6.85	-7.64	-2.0	-4.8
GaAs	-7.17	-8.33	-1.7	-4.5
Si	1.98	-0.48	-2.1	-4.8
Ge	-8.24	-9.48	-2.9	-5.3

Table 3.2: Deformation Potentials for GaSb, GaAs, Si and Ge, all values are in eV.

where **L** is the angular momentum operator, c.p. denotes cyclic permutations with respect to the indices x, y and z and the quantities in the curly brackets indicate the symmetrised product: $\{L_x L_y\} = \frac{1}{2}(L_x L_y + L_y L_x)$. The parameter a is the hydrostatic deformation potential. It represents the intraband (absolute) shift of the orbital valence bands due to the hydrostatic component of the strain. The quantities b and d are uniaxial deformation potentials appropriate to strains of tetragonal and rhombohedral symmetries, respectively. Values for the deformation potentials a_c, a, b and d are given in Table 3.2 for GaSb, GaAs, Si and Ge taken from the summary of experimental and theoretical results by Van der Walle, (1989). We will neglect the stress-dependent, spin-orbit contribution to the valence band strain Hamiltonian since it is small compared to the orbital-strain contribution (Pollack, 1973). In the eight-band $|J, M_J\rangle$ representation the total effective Hamiltonian for a bulk semiconductor, $H = H_0 + V^{so} + H_\epsilon^c + H_\epsilon^v$ can be written at the centre of the Brillouin zone

as (Pollack, 1990)

$$\overline{\overline{\mathbf{H}}} = \begin{bmatrix} E_0 + A & 0 & 0 & 0 & 0 & 0 & 0 & 0 \\ 0 & E_0 + A & 0 & 0 & 0 & 0 & 0 & 0 \\ 0 & 0 & B & E & F & 0 & G & H \\ 0 & 0 & E^* & C & 0 & F & I & J \\ 0 & 0 & F^* & 0 & C & E & J & -I \\ 0 & 0 & 0 & F^* & E^* & B & -H^* & G \\ 0 & 0 & G^* & I^* & J^* & -H & -\Delta + D & 0 \\ 0 & 0 & H^* & J^* & -I^* & G^* & 0 & -\Delta + D \end{bmatrix} \begin{matrix} |S\uparrow\rangle \\ |S\downarrow\rangle \\ \left|\frac{3}{2},\frac{3}{2}\right\rangle \\ \left|\frac{3}{2},\frac{1}{2}\right\rangle \\ \left|\frac{3}{2},-\frac{1}{2}\right\rangle \\ \left|\frac{3}{2},-\frac{3}{2}\right\rangle \\ \left|\frac{1}{2},\frac{1}{2}\right\rangle \\ \left|\frac{1}{2},-\frac{1}{2}\right\rangle \end{matrix}$$

$$\begin{aligned} A &= a_c(\epsilon_{xx} + \epsilon_{yy} + \epsilon_{zz}) \\ B &= -a(\epsilon_{xx} + \epsilon_{yy} + \epsilon_{zz}) - (b/2)(2\epsilon_{zz} - \epsilon_{xx} - \epsilon_{yy}) \\ C &= -a(\epsilon_{xx} + \epsilon_{yy} + \epsilon_{zz}) + (b/2)(2\epsilon_{zz} - \epsilon_{xx} - \epsilon_{yy}) \\ D &= -a(\epsilon_{xx} + \epsilon_{yy} + \epsilon_{zz}) \\ E &= d(\epsilon_{xz} - \epsilon_{yz}) \\ F &= (\sqrt{3}/2)b(\epsilon_{xx} - \epsilon_{yy}) - id\epsilon_{xy} \\ G &= -d(\epsilon_{xz} - i\epsilon_{yz}) \\ H &= (\sqrt{3/2})b(\epsilon_{xx} - \epsilon_{yy}) + (i/\sqrt{2})d\epsilon_{xy} \\ I &= -(b/\sqrt{2})(2\epsilon_{zz} - \epsilon_{xx} - \epsilon_{yy}) \\ J &= (\sqrt{3/2})d(\epsilon_{xz} - i\epsilon_{yz}). \end{aligned} \tag{3.49}$$

Diagonalisation of (3.49) yields the positions of the band edges in a bulk semiconductor subject to an arbitrary uniform deformation.

Consider the form of the effective Hamiltonian for the case of a strictly

hydrostatic strain. Under these conditions the strain matrix is diagonal, the only nonzero elements being $\epsilon_{xx} = \epsilon_{yy} = \epsilon_{zz}$. From (3.49) it is apparent that the total Hamiltonian is also diagonal for this strain configuration. If the stress is compressive, the negative fractional volume change and the negative conduction band deformation potential common to most semiconductors combine to shift the lowest conduction band at Γ up in energy relative to it's unstrained position. A compressive strain also causes a positive shift to the heavy hole, light hole and split off bands relative to their unstrained positions. No splittings of these states occurs since the cubic symmetry is retained.

A uniaxial stress applied parallel to the [001] axis results in a diagonal strain matrix with the nonzero components ϵ_{zz}, and $\epsilon_{xx} = \epsilon_{yy}$. In this case additional so-called biaxial terms enter into the effective Hamiltonian through the terms B, C, and I. The biaxial strain, which can be thought of as a hydrostatic strain plus a uniaxial strain, is proportional to $2\epsilon_{zz} - \epsilon_{xx} - \epsilon_{yy}$. The uniaxial stress splits the heavy hole and light hole states at Γ due to the reduction of symmetry, and introduces a coupling between the heavy hole and split off states.

3.2.3 Describing Heterostructures

The $\mathbf{k} \cdot \mathbf{p}$ theory in conjunction with the effective mass approximation (EMA) has been used to describe the electronic energy levels of semiconductor heterostructures (Bastard and Brum, 1986). The effective mass approximation for the heavy hole and light hole bands is stated as fol-

lows (Luttinger, 1955). If the dispersion relation of the set of degenerate bands satisfying ((3.1)) is given by

$$\sum_{j'=1}^{4} H_{jj'}^{LK} a_{j',\mathbf{k}} \equiv \sum_{j'=1}^{4} \left[E_{j,0}\delta_{jj'} + \sum_{\alpha,\beta} D_{jj'}^{\alpha\beta} k_\alpha k_\beta \right] a_{j',\mathbf{k}} = E_{\mathbf{k}} a_{j,\mathbf{k}} \tag{3.50}$$

then the solution $\psi(\mathbf{r})$ for the semiconductors in the presence of a perturbation $U(\mathbf{r})$, such as an impurity potential or a quantum well potential

$$\left[H_0 + V^{so} + U(\mathbf{r})\right] \psi(\mathbf{r}) = E\psi(\mathbf{r}) \tag{3.51}$$

is given by

$$\psi(\mathbf{r}) = \sum_{j=1}^{4} F_j(\mathbf{r}) u_{j,0}(\mathbf{r}) \tag{3.52}$$

where $F_j(\mathbf{r})$ satisfies

$$\sum_{j'=1}^{4} \left[E_{j,0}\delta_{jj'} + \sum_{\alpha,\beta} D_{jj'}^{\alpha\beta} \left(-i\frac{\partial}{\partial x_\alpha}\right)\left(-i\frac{\partial}{\partial x_\beta}\right) + U(\mathbf{r})\delta_{jj'} \right] F_{j'}(\mathbf{r}) = EF_j(\mathbf{r}) \tag{3.53}$$

The envelope function can be expanded in a set of normalised plane wave states

$$F_j(\mathbf{r}) = \sum_{\mathbf{g}} A_j(\mathbf{g}) \langle \mathbf{r} | \mathbf{g} \rangle \tag{3.54}$$

in which $\mathbf{g}$ is a reciprocal vector of the lattice of unit cells containing a single heterostructure or impurity potential. Substituting (3.54) into (3.53) and multiplying on the left by $\langle \mathbf{g}' |$ gives a square matrix of order $4 \times n_{\mathbf{g}}$, where $n_{\mathbf{g}}$ is the number of plane waves appearing in the expansion (3.54). The attraction of this approach is that there is no need to explicitly match wave functions across a boundary between the host and well materials; the method is thus easily applicable to an arbitrary confining potential.

A necessary condition is that the states in neighbouring heterostructures do not significantly overlap.

A number of simplifying assumptions are made during the construction of the Hamiltonian matrix. First, the periodic parts of the Bloch functions of the heavy and light hole states at Γ do not differ very much from the host to the dopant layers. Second, we assume that the $\{\gamma_i\}$ adopt values appropriate to bulk host material and that these values do not change with position in the unit cell. If the $\{\gamma_i\}$ were to depend on position then the placement of the partial derivatives in (3.53) with respect to the matrix elements $D_{jj'}$ would require careful consideration in order to preserve the Hermiticity of the effective Hamiltonian and the conservation of current across the interface. The scheme by which the abrupt change of the $\{\gamma_i\}$ across a heterostructure interface can by taken into account when using a plane wave basis has been discussed in detail by Baraff and Gershoni, (1991).

Chapter 4

Applying the $\mathbf{k} \cdot \mathbf{p}$ Method to Quantum Dot Heterostructures

When the concept of a one-dimensional confinement of charge in a semiconductor quantum well is abstracted to three dimension we obtain a quantum dot. While there is still a dispersion in the conduction and valence bands in quantum wells, quantum dots exhibit an atomic-like spectrum and a density of states that resembles a series of delta-functions. This changed dimensionality provides greater control over the optical and electronic properties of quantum dots than can be achieved by engineering the band structure of quantum wells.

Now although the empirical pseudopotential and $\mathbf{k} \cdot \mathbf{p}$ methods have been used to great effect to model superlattices and multiple quantum well structures (see for example Shaw, 1998), they have great difficulty in modeling large heterostructures. A unit cell size of > 1000 atoms be-

comes computationally expensive. However, a typically measured quantum dot requires $\sim 200,000$ atoms. Therefore we require a different approach to the traditional matrix creation and diagonalision procedure.

In this chapter we outline the details of applying the $\mathbf{k} \cdot \mathbf{p}$ scheme described earlier for a quantum dot heterostructure.

4.1 Atomic Positions

The positions of the atoms in a quantum dot island and the surrounding host layer are determined using a molecular mechanical model. In this approach the atoms are considered as point particles and the bonds as springs. The mathematics of spring deformation can be used to describe the ability of the bonds to stretch and bend. The object of molecular mechanics is to predict the energy associated with a given atomic structure then attempt to find another structure with a lower energy. When this process is repeated many times and an energy minima is reached, we can assume we have obtained a good approximation to the true equilibrium structure. The total energy in this model is the sum of the total energy associated with the stretching of bonds and the total energy associated with the bending of bonds. These total energies have no meaning as absolute quantities, only differences between two or more structures have meaning. The total energy expression together with the data (parameters) required to describe the behaviour of different kinds of atoms and distortions constitutes a force field. Many different kinds of force field have

been developed over the years. Some include additional energy terms that describe longer ranged interactions. Some force fields account for coupling between bending and stretching in adjacent bonds, bond twisting terms, and non-bonded interactions (e.g. Van de Waals) in order to improve the accuracy of the model.

The choice of force field depends, of course, on the type of bonding present in the material under consideration. In the III-V semiconductors considered here, which displays covalent bonding with only limited charge transfer, the valence force field (VFF) is most suitable. We begin by writing the total potential energy as the sum over the atoms in the dot and host materials,

$$E_{tot} = \sum_{i}^{d} V_i^d + \sum_{i'}^{b} V_{i'}^b, \tag{4.1}$$

where V^d and V^b represent the potential of an atom of the dot and host material respectively. The potential assigned to the ith atom of the dot material may be written as

$$\begin{aligned} V_i^d = & \frac{1}{4}\sum_{j=1}^{n} f_r^d(\Delta r_{ij})^2 + \frac{1}{2} f_\theta^d (r_0^d)^2 \sum_{j=1}^{n-1}\sum_{k=j+1}^{n} (\theta_{ijk})^2 + f_{rr}^d \sum_{j=1}^{n-1}\sum_{k=j+1}^{n} \Delta r_{ij}\Delta r_{ik} \\ & + r_0^d f_{r\theta}^d \sum_{j=1}^{n-1}\sum_{k=j+1}^{n} (\Delta_{ij} + \Delta r_{ik})\Delta\theta_{jik} \\ & + (r_0^d)^2 f_{\theta\theta}^d \sum_{j=1}^{n-2}\sum_{k=j+1}^{n-1}\sum_{l=k+1}^{n} (\Delta\theta_{jik}\Delta\theta_{kil} + \Delta\theta_{kil}\Delta\theta_{lij} + \Delta\theta_{lij}\Delta\theta_{jik}), \end{aligned} \tag{4.2}$$

where $\Delta r_{ij} = r_{ij} - r_{ij}^0$, $\Delta\theta_{jik} = \theta_{jik} - \theta_{jik}^0$ and r_{ij}^0 and θ_{jik}^0 are the equilibrium values of the length of the bond between atoms i and j and the angle subtended by atoms j and k at atom i. n is the coordination number. The summations have all been symmetrised and the factors of $(1/2)$ and $(1/4)$

	f_r (eV/Å^2)	f_θ (eV/Å^2)	f_{rr} (eV/Å^2)	$f_{r\theta}$ (eV/Å^2)	$f_{\theta\theta}$ (eV/Å^2)
GaSb	6.6153	0.2126	0.0974	0.1915	-0.1600
GaAs	7.9689	0.3071	0.4350	0.1813	-0.0028
Si	7.9556	0.3023	0.2965	0.1516	-0.0230
Ge	6.8923	0.2489	0.1629	0.1287	-0.0125

Table 4.1: Valence Force Field Parameters for GaSb, GaAs, Si and Ge.

inserted to avoid double counting. The force constants, f^d, characterise the strength of the different interactions that make up the valence force field for the dot material. The parameter f_r^d is the bond stretching force constant, f_θ^d the bond bending force constant, f_{rr}^d accounts for the coupling between bonds sharing a common atom, $f_{r\theta}^d$ describes the strength of the coupling between an angle and a bond along one leg of θ, and $f_{\theta\theta}^d$ describes the correlation between angles having a common leg and apex. A similar set of force constants exists for the host material.

In the past the VFF method has been used to determine a range of elastic and vibrational properties of covalently bonded solids. Musgrave and Pople, (1962) and McMurry *et al.*, (1967) carried out VFF calculations of the phonon spectrum of diamond. Martin, (1970) investigated the elastic properties of ZnS using a VFF model which accounted for charge transfer through the inclusion of a Coulomb term. Here we are interested in using the VFF model to determine the positions of atoms in the dot and host materials and then extracting information concerning the distribution of strain in and around the islands.

The transfer of charge between the two atomic species in III-V materials should be taken into account through an additional term in (4.2) representing the extra interatomic force resulting from the placement of a point charge on each of the atoms. The resulting electrostatic interaction is the cause of the TO-LO splitting observed at $\mathbf{q} = 0$ in the phonon spectra of these materials. This additional Coulomb term was neglected and instead the five force constants adjusted such that the phonon spectrum in the neighbourhood of $\mathbf{q} = 0$ was well reproduced and agreed with the values predicted from the elastic constants of the material. Although the TO-LO splitting is not recovered during the fitting procedure, the low frequency part of the spectrum was accurately obtained. By this method, the effects of the Coulomb term on the acoustic branches of the spectrum in the neighbourhood of $\mathbf{q} = 0$ were included in the force constants. This was important as it is primarily the longer-wavelength variation in strain that is most important for the electronic structure determination described later on. The force constants used in the structure calculation are listed in Table 4.1.

The calculation of the atomic positions in the dot and host proceeded by placing every atom in a unit cell containing a single island and a wetting layer section surrounded by the host material, at the atomic positions that would be occupied by host atoms in a similar sized unit cell of pure host. The total energy of this conformation was calculated, together with the net force on each atom. Each atom was moved a distance in the direction of the net force and then the total energy was recalculated. This

procedure was repeated until the total energy reached a minimum.

4.2 Strain Distribution

To recover the strain tensor from the relaxed atomic positions, the new positions are compared to the normal bulk positions of the host material. This tensor is assigned to the structure on the basis of the conventional eight atom unit cell. In this way a three-dimensional pattern of the strain can be recovered. Figure (4.1) shows a typical conventional cubic unit cell shown before and after the relaxation process with the deformed and undeformed unit basis vectors labelled. There are several remarks to be made on this method. Firstly, the reason for using an eight atom unit cell is a result of the underlying theory of the strain tensor, i.e. that it assumes a continuum, therefore it cannot be reliably applied to calculat-

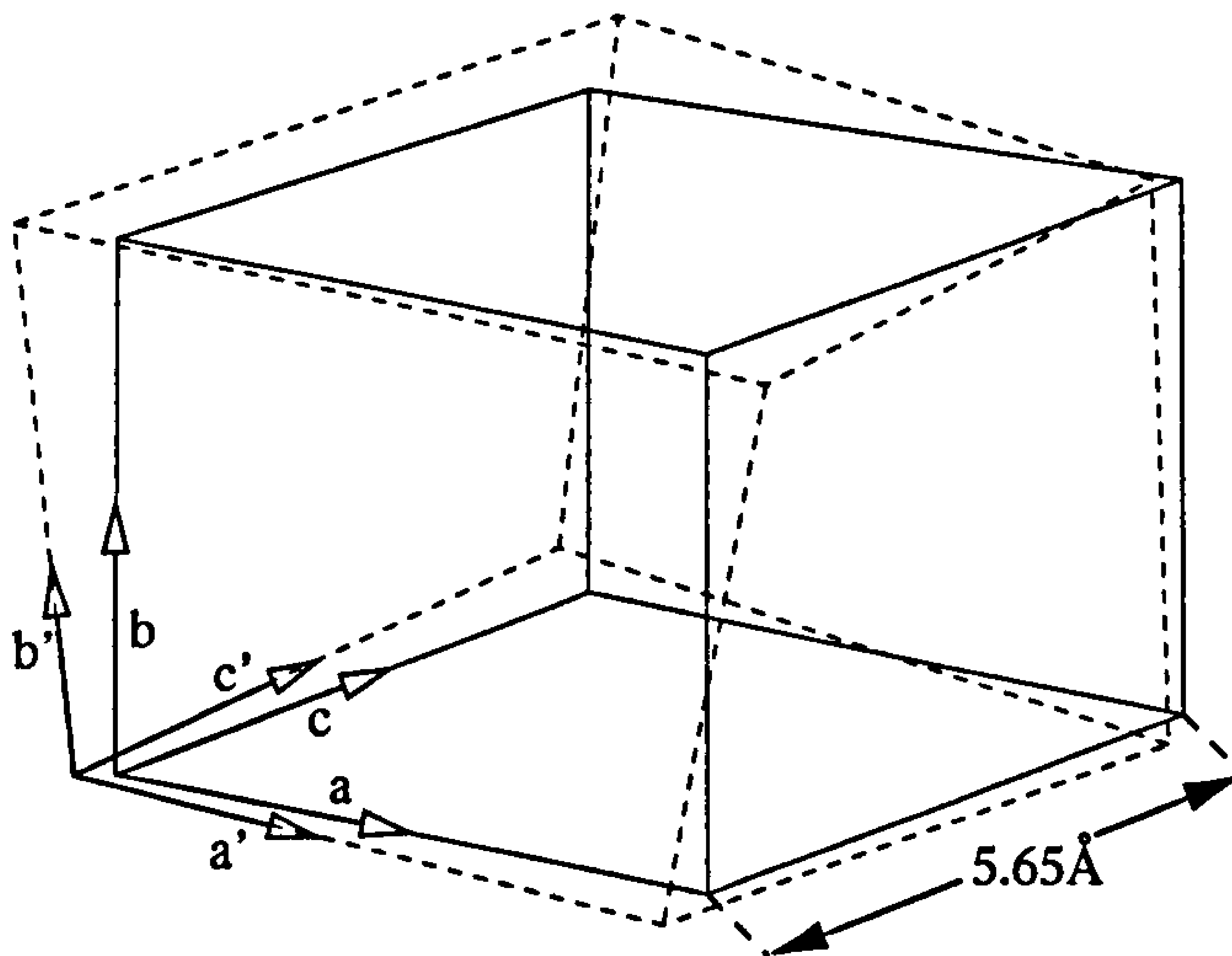

Figure 4.1: A conventional cubic unit cell inside the quantum dot structure before and after deformation.

ing the strain of individual atoms. Secondly, as a consequence of the first comment, the theory breaks down at the interface between the materials in the heterostructure. This means that the strain cannot be accurately calculated at the interface or within the wetting layer (if present). Thirdly, we must solve three simultaneous equations with three unknowns as outlined in equation (3.40) for *every* eight atom unit cell. Despite these restrictions a good description of the strain away from the interface and wetting layer is attainable in a relatively quick manner.

4.3 Confining Potentials

In the absence of strain effects, the confining potential for a charge carrier is a square well formed by the difference in the absolute energy of the conduction or valence band edges in the materials under scrutiny. To calculate the energy levels and electron (or hole) wavefunctions, we use the multi-band effective mass theory outlined earlier. For simplicity, we assume that the conduction and valence bands are decoupled. The general solutions for the electron states are given by:

$$\psi_n^c(\mathbf{r}) = u_1^c(\mathbf{r})\phi_{1,n}^c(\mathbf{r}) \tag{4.3}$$

where u_1^c is the bulk conduction band-edge Bloch function and $\phi_{1,n}^c$ is an envelope function satisfying the simple single-band Schrödinger equation.

$$\left[-\frac{\hbar^2}{2m^*}\nabla^2 + V(\mathbf{r})\right]\phi(\mathbf{r}) = E\phi(\mathbf{r}) \tag{4.4}$$

in which m^* is the isotropic effective mass of the lowest conduction band state and $V(\mathbf{R})$ is the three-dimensional confining potential. We express $\phi(\mathbf{r})$ as a sum over plane waves, each with the periodicity of a unit cell containing a single quantum dot.

$$\phi(\mathbf{r}) = \frac{1}{\sqrt{\Omega}} \sum_{\mathbf{g}} A(\mathbf{g}) e^{i\mathbf{g}\cdot\mathbf{r}} \tag{4.5}$$

and obtain a matrix equation for the conduction band problem:

$$\left[-\frac{\hbar^2}{2m^*} |\mathbf{g}'|^2 - E \right] A(\mathbf{g}') + \frac{1}{\Omega} \sum_{\mathbf{g}} A(\mathbf{g}) \int_{\Omega} V(\mathbf{r}) e^{i(\mathbf{g}-\mathbf{g}')\cdot\mathbf{r}} d^3\mathbf{r} = 0 \tag{4.6}$$

In (4.5) and (4.6), $\mathbf{g}$ is a reciprocal lattice vector of the periodic array of quantum dot unit cells, and Ω is the volume of one such cell. The number of plane waves required to achieve convergence of the series (4.5) depends of the characteristic dimensions of the dot and on the interdot separation. The attraction of this approach is that there is no need to explicitly match the wavefunctions across a boundary between the host and dot materials; the method is thus easily applicable to an arbitrary confining potential. However, the boundary conditions are that the states in neighbouring quantum dots do not overlap significantly.

The valence band states are determined using the four-band Luttinger-Kohn Hamiltonian that has the form given by 3.37. The Kohn-Luttinger parameters of Equation (3.35) are calculated using the method outlined in the following section. In the case of a quantum dot, we have the equation:

$$[H + V(\mathbf{r})]\phi^v(\mathbf{r}) = E\phi^v(\mathbf{r}) \tag{4.7}$$

where the confining potential V(**r**) is added to the diagonal elements of the 4×4 matrix. Since, for the problem of 3-D confinement, k_x, k_y, k_z are no

longer good quantum numbers we must make the following replacements in Equation (3.37):

$$k_x \Rightarrow -i\frac{\partial}{\partial x}, \quad k_y \Rightarrow -i\frac{\partial}{\partial y}, \quad k_z \Rightarrow -i\frac{\partial}{\partial z}. \tag{4.8}$$

Equation (4.6) is solved using an expansion in plane waves with the mth valence band wavefunction being given by

$$\psi^v_m(\mathbf{r}) = \sum_{j=1}^{4} u^v_j(\mathbf{r})\phi^v_{j,m}(\mathbf{r}) \tag{4.9}$$

where u^v_j are the $J = 3/2$ angular momentum states.

If we diagonalise (4.6) using an analytical method, we will obtain N_G eigenvalues and wavefunctions (where N_G is the number of plane waves in the expansion) and the computational time will scale $\propto N_G^3$. However, we require only the first few confined eigenvalues. Fortunately there exists a useful algorithm package called ARPACK (Arnoldi-Ritz PACKage). This provides the means to iterate to the lowest magnitude eigenvalue using the Lanczos method. This method involves evaluating the Hamiltonian upon a trial wavefunction in each iteration and does not require that the entire set of wavefunctions to be stored in memory at once. Diagonalisation of (4.6) by this method scales $\propto N_G^2$ and therefore provides a large saving in processor time as well as memory usage.

4.4 Effective Masses

When modeling the electronic structure of quantum dots the main perturbation to the system is the effect of strain. This effect manifests itself in

two ways: on the potential well, (described above) in which the electron and holes are confined, and on the effective masses of the charge carriers within that potential. In the dot material, compressive stress alters the curvature of the bulk Bands causing the effective masses to differ from those of the unstrained material. This is an important effect to include in the model. However, we have only taken into account the effect of the hydrostatic strain on the charge carriers and neglected the effects of the symmetry breaking biaxial strain because of the difficulty of implementation. These hydrostatically strained effective masses are obtained by performing empirical pseudopotential band structure calculations for the conduction ⇒ valence band momentum matrix elements (P_{cv}) of the host material under the appropriate hydrostatic strain.

Chapter 5

Si/Ge Quantum Dots for Infrared Applications

In this chapter we applied the theory and methodology outlined earlier to model Si/Ge quantum dots. We introduce Si/Ge self-assembled quantum dots that have infrared applications operating in the 3-5 micron range. Conventional Si/Ge quantum well structures are transparent to such wavelengths in the absence of heavy doping. We show that the high degree of strain lowers the band gap and also that the electrons and holes are both localised in the interfacial region. This will consequently enhance the optical transition probabilities.

5.1 Introduction and Background

There have been numerous attempts to design heterostructures of Si and Ge with the intention to make, for example, infrared detectors. The task is then to optimize the key figures of merit (quantum efficiency, dark current, bandwidth) at the favored operational wavelengths i.e. 3-5 and 10 micrometers. Since the band gap of any quantum well Si/Ge system is too large the only option is to make use of an extrinsic (e.g. p-type) structure in which incoming photons create excitations between valence minibands. The disadvantages of such a strategy compared to bulk (e.g. HgCdTe) or n-type (e.g. GaAs/GaAlAs) systems are well known Manareh, (1993). The complex dispersion and momentum mixing in valence minibands as well as interface roughness and unavoidable dopants create a variety of effective scattering and recombination channels. This greatly reduces the quantum efficiency and overall control of the system. It is therefore desirable to seek radically new solutions. Ideally, one desires an intrinsic system with minimum dispersion in the valence band, and a suitable electronic continuum to ensure effective current collection (e.g. weak electron phonon interaction). It is born in mind that most of these conditions might be met by a Ge self-assembled quantum dot (SAQD). Assuming such SAQDs can be fabricated (for reference see Apetz, 1995 or LeGoues, 1995) there are two fundamental questions to be addressed. First, is it possible that in spite of the strong strain field and the finite SAQD size the band gap will be small enough to permit applications at least in the 3-5 mi-

crometer band, and second, if so how can the optical transition in what is essentially an indirect gap system be strong enough to warrant optical applications? As for the second question, we will show that the lowest conduction band state corresponds to the bulk Si indirect band-gap ie that the electrons are confined in silicon. Therefore it is reasonable to expect that conventional selection rules will be broken due to the scattering event (momentum mixing) that the electrons undergo when a Si electron encounters the Ge potential well. This process has previously been investigated with Si/Ge quantum wells with considerable success (for example Jaros, 1990 or Turton, 1996) However, a microscopic calculation to verify this process for a SAQD is very difficult due to the large size of the structure. Therefore it is the purpose of this study to show that the first necessary question can be satisfied. This then creates room for fresh experimentation as previous experiments and theoretical investigations regarding Si/Ge SAQDs have concentrated on the transition related to the direct Ge and indirect Si band-gap energies (Jiang, 1998; Kwok, 1999; Mateeva, 1999; Takagahara, 1992; Ren, 1997; Ren, 1996; Eberl, 2000; Lüth, 1998).

5.2 Determining the Correct Quantum Dot Size to Model

Recently, successful studies have been made of SAQD structures consisting of III-V materials (e.g. GaSb, GaAs, InAs). We have carried out exten-

sive computer modeling of the electronic structure and optical response in such systems (Cusack, 1996). This enabled us to develop a pragmatic macroscopic model that makes it possible to evaluate the form of the potential resulting from the complex strain distribution in such a large system. In this study we shall employ our scheme to assess the electronic structure of Ge SAQDs of similar size with a view to establishing how the band gap of the Si/Ge SAQD system depends on the strain distribution. The band offset in the valence band is large ($\approx$840 meV) and so are the hole masses so that the details of the mass mismatch at the interfaces are irrelevant. However, it transpires (Cusack, 1996; Gruundmann, 1995b) that the strain distribution in and outside the SAQD volume makes a substantial contribution to the depth of the confining potential. This in turn greatly affects the depth and distribution (order) of confined levels on which the functioning of our detector would depend. Our model was designed to provide an accurate estimate of this effect. This means that we have a reliable form of the potential inside the SAQD with which to evaluate the position of confined states.

It is important then, to model a structure that may be conceivably created experimentally and displays some interesting, unexpected property. We have chosen a SAQD consisting of a square-based pyramid of Ge with a base length of 108 Å and a height of 54 Å resting on a 5 Å thick layer of Ge and is entirely surrounded by Si.

5.3 The Strain Distribution and Electronic Structure

The strain tensor components plotted along the principal axis of symmetry (Z-axis) of the Si/Ge SAQD are shown in Figure (5.1). The strain tensor components in the Si/Ge SAQD generally have the same form as those in the InAs/GaAs systems (Cusack, 1996) but are smaller in magnitude due to the smaller lattice mismatch (4% in Si/Ge compared with 7% in InAs/GaAs). In common with the InAs/GaAs structures, hydrostatic and biaxial strain conditions prevail throughout the Si/Ge SAQD.

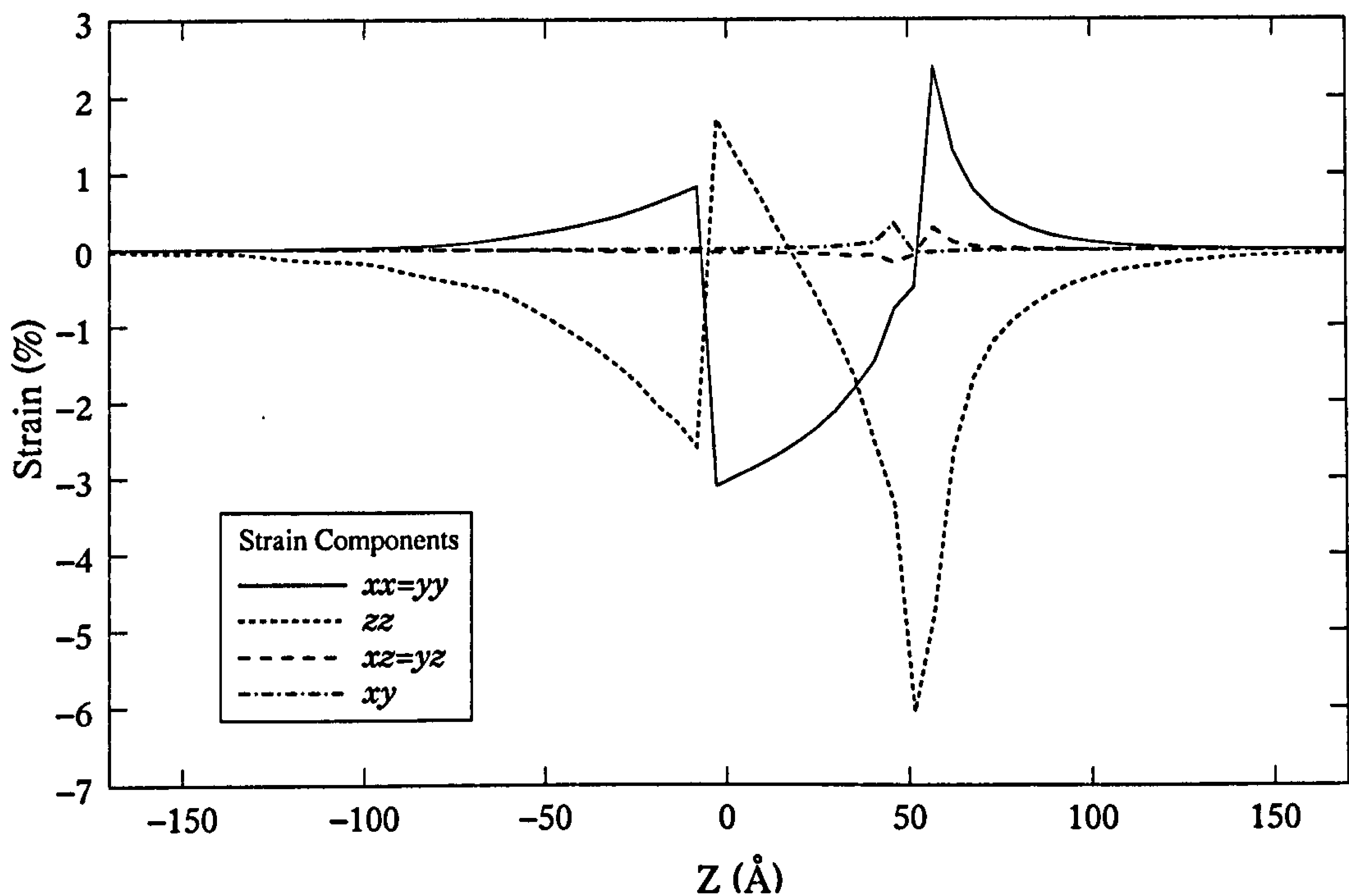

Figure 5.1: The strain tensor components plotted along the Z-Axis through the apex of the pyramid.

We find that throughout the Si the two Δ valleys along k_z are lower in energy than the four Δ valleys found in the k_{x-y} plane. In the Ge, whether the minima in the k_{x-y} plane or the minima along k_z are lower in energy depends strongly on the position. However, since the lowest bulk conduction band energies are found in the Si immediately above and below the Ge pyramid we expect the lowest SAQD conduction state to reside in the Si barrier.

In Figure (5.2) we show the position dependence of the k_z direction Δ minima and the heavy hole and light hole bands in Si and Ge along the Z-axis of the pyramidal Si/Ge SAQD. We have calculated the valence state

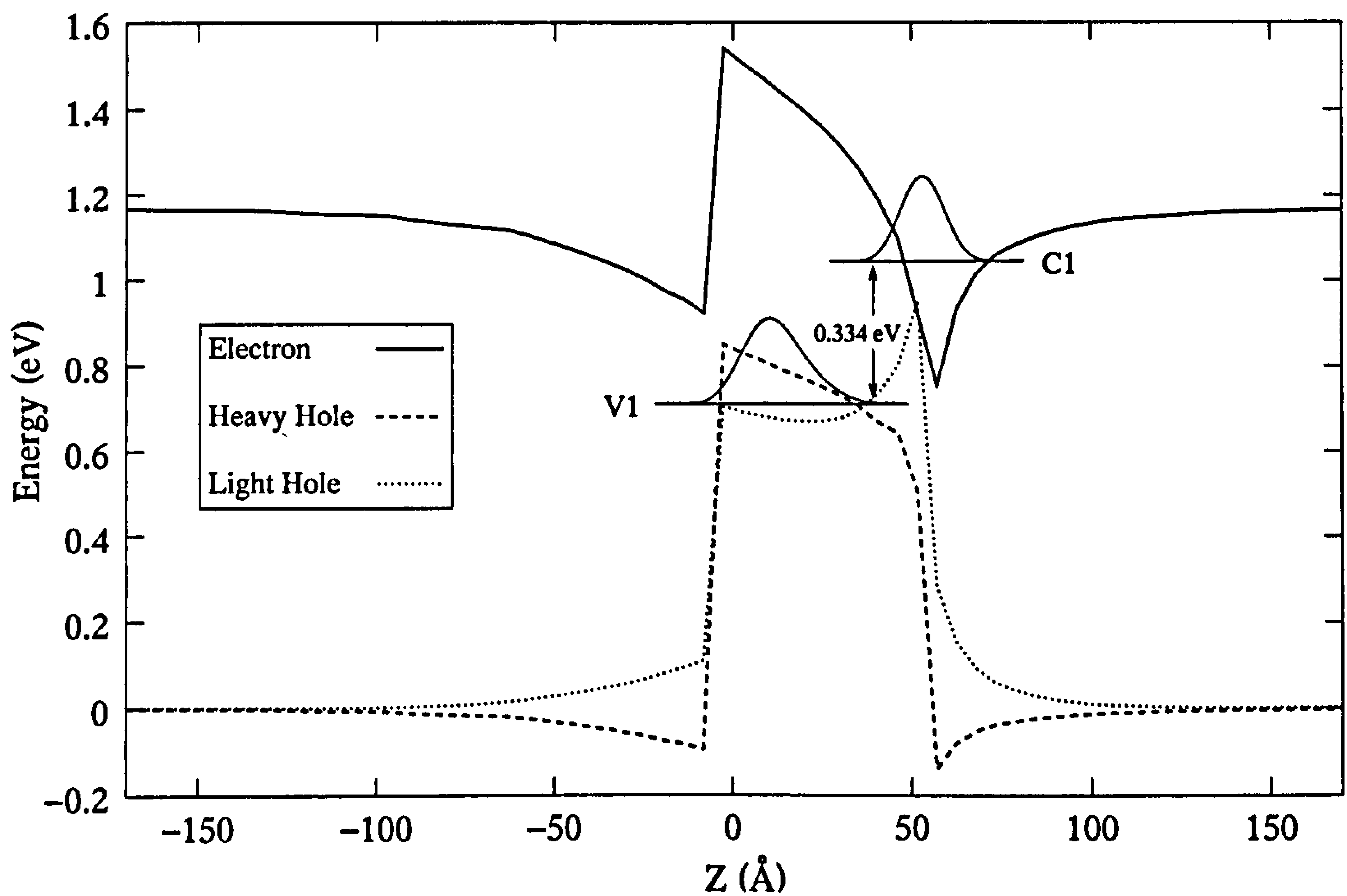

Figure 5.2: The position dependence of the k_z direction Δ minima and the heavy and light hole bands along the Z-axis of the quantum dot.

γ_1	γ_2	γ_3	m^*
-7.765	-2.367	-3.267	0.191

Table 5.1: Hydrostatically strained Ge Luttinger parameters and conduction band effective mass used in the calculation.

energies in the Ge pyramid using a four-band effective mass calculation outlined previously. The split-off band is far away in energy from the heavy hole and light hole bands in the Ge SAQD and so plays no part in our calculation. Also, because of the large valence band offset between Si and Ge no account need be taken of the discontinuity in the effective masses across the interface. Therefore, the valence band effective masses of Ge were used. The hydrostatically strained Luttinger parameters are shown in Table 5.1. The effect of strain on these masses was estimated by performing semi-empirical pseudopotential calculations for the effective masses under the hydrostatic strain conditions existing near to the center of the Ge pyramid. From the calculation, the uppermost valence state (V1) is 723 meV above the band edge of unstrained Si. The energy level is indicated in Figure (5.2) together with the envelope of the charge density. Because of the strongly inhomogeneous heavy hole potential, the ground hole state is confined towards the base of the Ge pyramid.

We performed a single valley effective mass calculation for the electron energies in the Si/Ge SAQD system. The effective masses in the k_{x-y} direction (m_t) and the k_z direction (m_l) in unstrained Si are also given in Table 5.1. Our simple conduction band calculation gives a lowest con-

duction state (C1) energy 125 meV below the conduction band edge of unstrained Si. In Figure (5.2) the envelope of the charge density of the C1 state can be seen to be localized in the Si barrier immediately above the apex of the Ge SAQD. The strain-induced proximity of the electron and hole charge enhances the probability of a ground state transition in this structure Shaw, (1999).

From our calculations, we predict our SAQD to have a band gap of 0.334 eV (3.7 μm). We also performed calculations for larger SiGe SAQDs possessing the same height to width ratios. The lowest conduction level and the highest valence level for these SAQDs are given in Figure (5.3) , relative to the unstrained band edge of Si. The largest SAQD studied

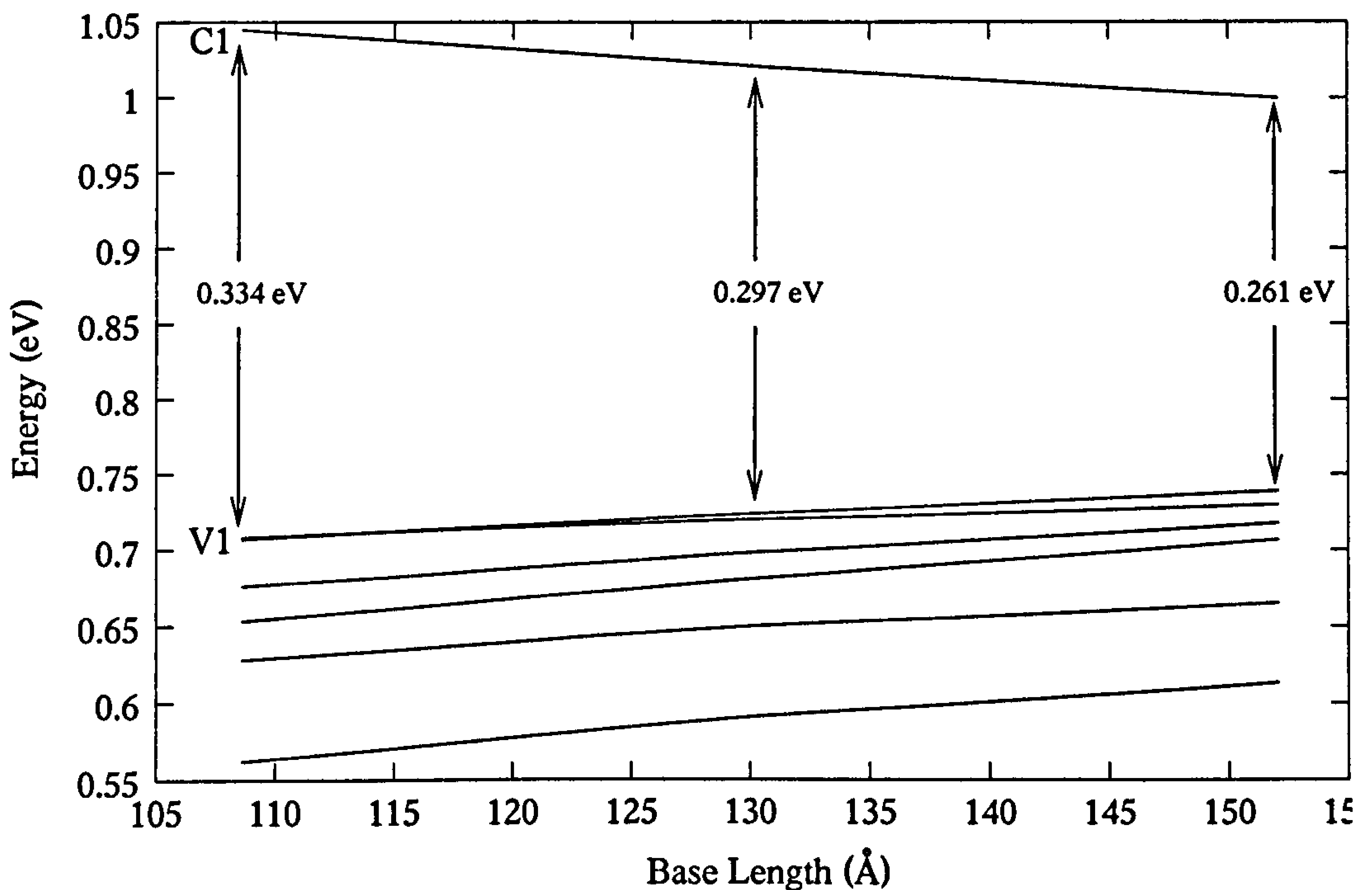

Figure 5.3: The variation of emission energy with SAQD size.

has a base length of 152 Å and a band gap of 0.261 eV (4.7μm) and so is also suited to infrared detector applications. Furthermore, since any extrinsic feature which must be added in order to study quantitatively the magnitude and lineshape of the optical response can only make this transition energy smaller we shall conclude that the Si/Ge SAQD system is suitable for detector applications.

5.4 Conclusion

In summary, we propose that Si/Ge SAQDs can be used as the basis of an infrared detector operating in the 3-5 μm range of wavelengths, a regime inaccessible to intrinsic Si/Ge quantum well systems. Our calculations show that the inhomogeneous strain in these structures lowers the band gap and confines electron and hole carriers in spatial proximity. Hence, the SAQDs exhibit favorable optical characteristics that warrant further investigation.

Chapter 6

Electronic Structure of GaSb/GaAs Quantum Dots

In this chapter we examine the electronic structure of quantum dots that are fabricated from the III-V compounds GaSb and GaAs, using the method and theory outlined in earlier chapters. These materials are of particular interest when used in a heterostructure because they exhibit a Type II band-gap line-up. As a consequence, they offer fresh opportunities for production of optical and electronic devices. A further motivation for researching quantum dots of this type is an apparent discrepancy between experiment and theory regarding the value of the conduction band offset.

6.1 Introduction and Background

Quantum dots with wide range of sizes have been reported. Atomic Force Microscopy (AFM) measurements (Glaser, 1996) have revealed these dots to have a vertical extent of 100-200 Å and width of 400-600 Å. The exact shape of these dots is not well established. Interestingly, the photoluminescence spectra for this range of dot sizes is remarkably constant at around 1.1 eV. This contradicts the prediction of basic quantum well models as well as our own calculations casting doubt on whether quantum confinement is the origin of the photoluminescence spectra. Such findings have prompted researchers to investigate alternative mechanisms for recombination such as interface related models (Hatami, 1998). Our aim in this chapter, then, is to use our model to attempt to make contact with recent experimental results and to shed light upon the possible origin of this discrepancy.

When a self-assembled quantum dot forms, it generally forms a pyramidal shape. However, in order to create a useful technological device the structures are then "capped" with a further layer of the host substrate, in this case GaAs. As the shape of capped quantum dots is not currently well known, we have chosen to model a dome shaped dot with a lateral width of 200 Å and a height of 50 Å. This is a reasonable compromise as even a pyramidal dot will doubtless become more rounded due to the capping process and strain. In addition, recent transmission electron microscopy (TEM) measurements (Prieto, 1998) have shown InSb/InP dots of compara-

ble size to have a dome-like structure. The reason for choosing the above dome dimensions is that the method outlined in a previous chapter, has been developed to model heterostructures with unit cells of the order of a million atoms. In order for the strain fields to reach approximately zero at the edges of the unit cell, this structure requires a unit cell of the order of 6 million atoms. This size unit cell is the largest possible case that can be modeled using the computing resources available at the time of the calculation. That is, approximately 600Mb of physical memory and two weeks of processor time on a SUN System Ultra SPARC 200MHz processor. Since the memory and processing time requirements for relaxation scales roughly linearly with the number of atoms, to model the actual size of the dots sizes reported in experiment would require approximately eight times more memory and more than eight times the processor time. Therefore, in order to produce calculations over a range of dome sizes we have found that simply scaling the size of this dome in the electronic structure calculation yields results consistent with producing dome sizes from first principles. Note that the lateral extent is such that the x/y dimensions are a second order effect when compared to the much smaller height dimension in a quantum confinement model. Hence dome (our theoretical work) or dot (any other referred work) sizes quoted now refer simply to the height of the dome or dot. In addition the dome rests upon 2 ML of wetting layer and is entirely surrounded by GaAs. Also, in order to produce calculations over a range of domes sizes we have simply scaled the size of this dome in the electronic structure calculation.

6.2 Electronic Structure

The shape and dimensions of the domes modeled are such that the strain has almost constant hydrostatic and biaxial components inside the dome. This is consistent with results obtained from GaAs/InAs pyramidal dots with a similarly small height/width ratio (Cusack, 1997). The strained potential profile is then constructed using the deformation potentials calculated by Van de Walle, (1989) coupled with the strain data obtained from the above method. Figure (6.1) shows that in the z-direction this profile closely resembles a quantum well with modification near the interface due

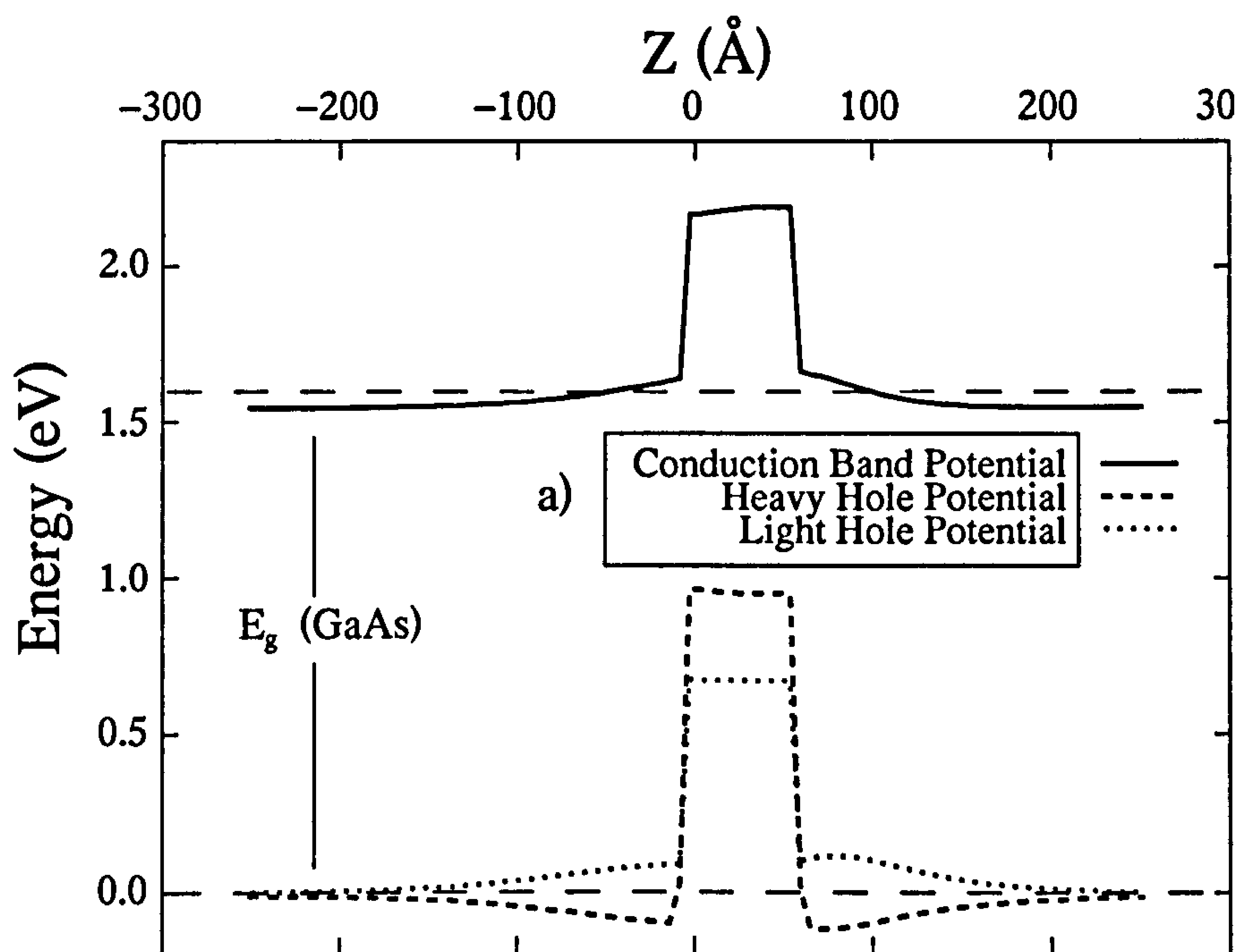

Figure 6.1: The strained conduction band, heavy and light hole potentials of the GaSb/GaAs Quantum Dome. These potentials have been calculated using the Van der Walle data.

γ_1	γ_2	γ_3	m^*
-17.326	-3.578	-3.389	0.080

Table 6.1: Hydrostatically strained GaSb Luttinger parameters and conduction band effective mass used in the calculation.

to strain. As the hydrostatic and biaxial strain present in the dome causes the effective masses to be changed we must obtain new effective masses consistent with this new strain distribution. We have obtained a first approximation of these strained masses using our pseudopotential method. The derived Luttinger parameters from those calculations can be seen in Table 6.1.

The problem that has arisen when performing an electronic structure calculation is the acute sensitivity of the transition energy to the size of the dot. Figure (6.2)b shows that our predicted transition energies drop quickly with dome height. This is because the wells in the valence and conduction bands are very deep and hence in a large dome the ground state eigenvalue is deeply confined. For example, for a dome height of 100 Å the transition energy between the ground states in the valence and conduction bands is around $\sim$ 600 meV. This is contrary to the transition energy experimentally obtained for similar dot sizes of around 1.1 - 1.2 eV (Glaser, 1996). Indeed, to match this transition energy we predict that a dome height of around 20 Å would be required. Furthermore, all the domes in the lattice would have to be very close to that height (say $\pm 5 - 10$ Å) in order to be consistent with the line width of experimental

photoluminescence curve, such is the critical dependence on the dome height.

Since AFM images sample the strain field rather than the true size of the GaSb dot, the dimensions of the dots are likely to be overestimates. However, it is unlikely in the extreme that the overestimate is sufficient to provide an explanation for the above discrepancy. Also Ledentsov, (1995) reported quantum well structures over a 3-10 Å range that have a similarly large discrepancy in transition energy.

Ledentsov, (1995) proposed that the experimental results they obtained are more consistent with those expected if the conduction and valence band wells are shallower. This presents a possible explanation of the

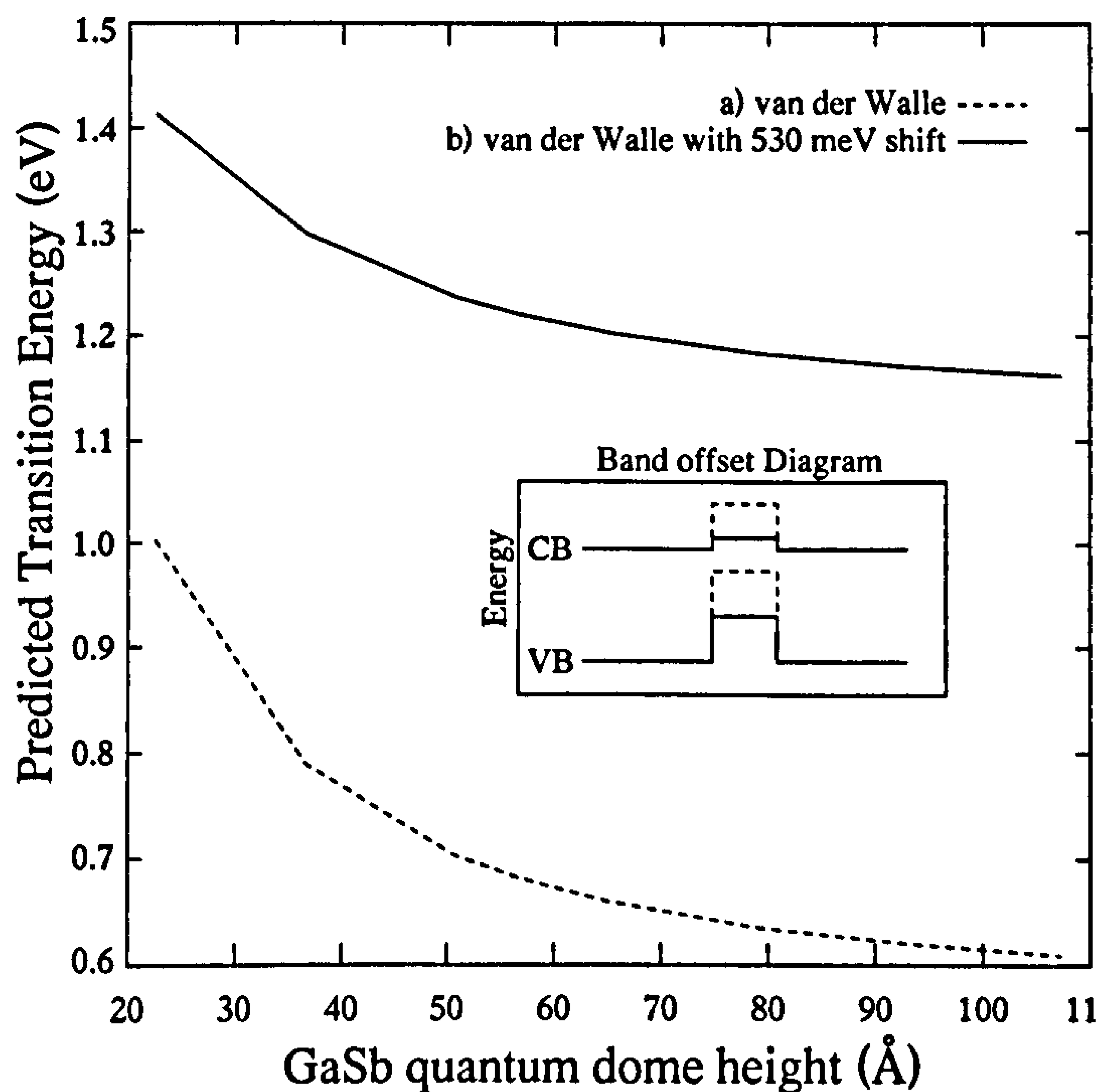

Figure 6.2: The variation of emission energy with SAQD size.

problem. Ledentsov and ourselves have obtained the conduction and valence band offsets from the work of van de Walle. Doubt is therefore cast on the value of $\sim$ 630 meV for the conduction band offset that is obtained from Van de Walle (shown in Figure (6.1)).

To obtain the conduction band offset for a Type II material experimentally is very difficult. Direct optical measurements do not give any information on the conduction band offset due to the spatially indirect electron-hole recombination. Also electrical transport methods cannot yield this value as the dots are too small and any measurement would average out over the entire area regardless of whether there is or is not a dots there. However, recently the relatively new technique of Ballistic Emission Electron Microscopy (BEEM) has been applied to the problem. Experiments performed using this technique (Rubin, 1997) have placed the value of the conduction band offset at 80 ± 20 meV, c.f. van de Walle derived offset of $\sim$ 630 meV. This is a substantial deviation and no attempt to reconcile difference is provided here. However assuming deformation potential theory holds, we can compare the Van de Walle derived conduction band offset with the experimental offset and apply a rigid shift to both the conduction and valence band potentials within the dome. The magnitude of this shift, within our calculation, is ultimately governed by the potential at the interface. Examination of Figure (6.1) shows that immediately outside the dome the conduction band offset from the strained potential alone is 100 meV. Therefore, in order to be consistent with experiment we have applied a rigid shift to the conduction band, heavy hole

and light hole potentials within the dome. This results in a conduction band well that is not localised within the dome, and without any confined states. In addition, the heavy hole and light hole potential wells are much smaller. Figure (6.3) shows the proposed new confining potentials.

This then provides a possible explanation — without having to abandon the simple quantum confinement mechanism — of the inconsistencies between predicted and measured values of dot size and transition energy.

Electronic structure calculations performed using these shallower wells are revealing. Figure (6.2)b shows that the ground state in the valence

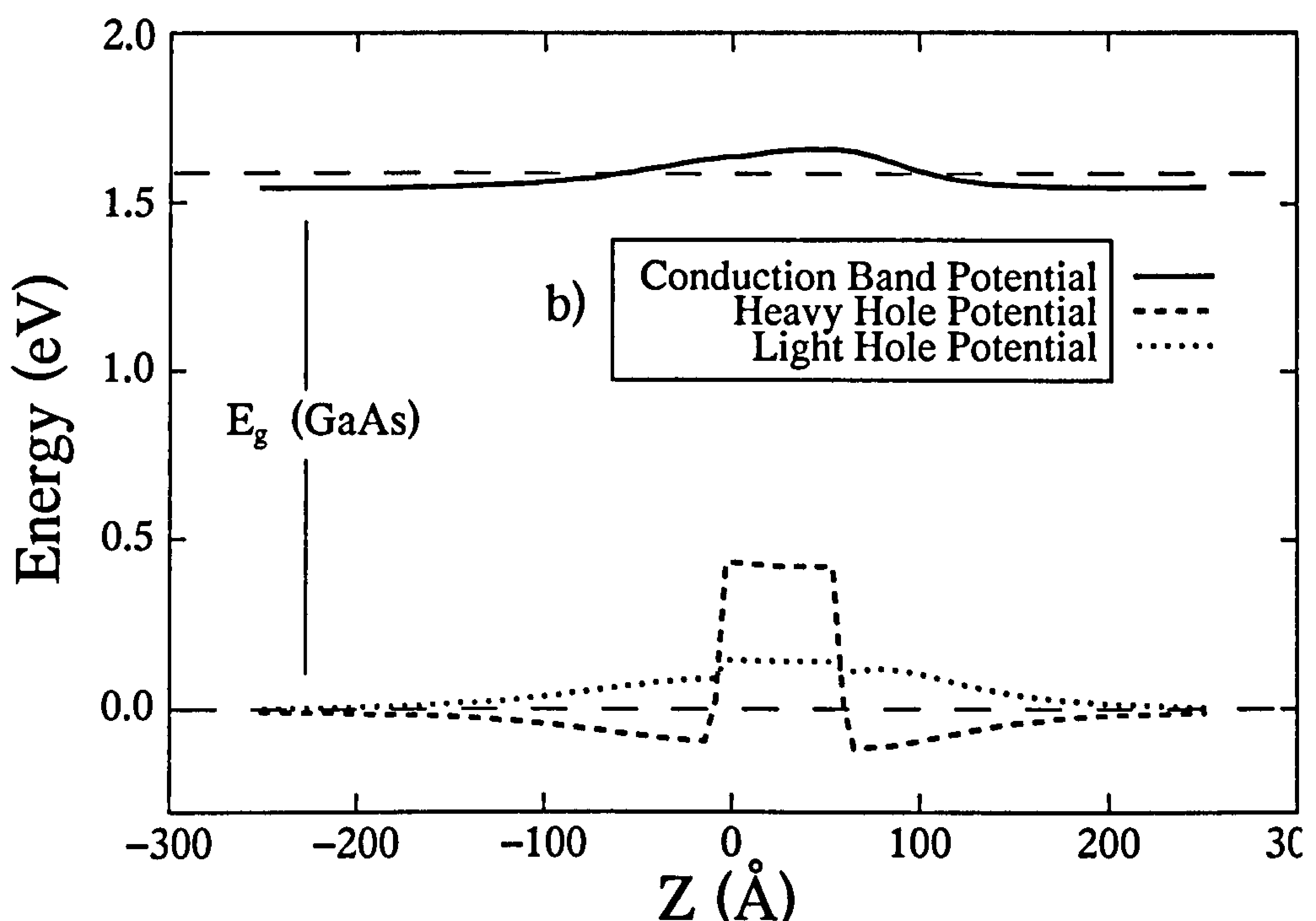

Figure 6.3: The GaSb/GaAs quantum dome potentials after a rigid shift of the potentials has taken place to bring the conduction band offset in line with experimental measurements.

band potential well is much nearer the top of the well for a large dot. This leaves less room for variation as the dot size decreases. Indeed, our calculations predict that the transition energy varies over a much smaller range compared to the previous results (Figure (6.2)b). Also for the larger domes the transition energies predicted are much more consistent with experiment. Note that although the transition energy begins to rise steeply as the dome height approaches 20 Å, this is probably exaggerated due to the method of scaling we have performed, i.e. that the entire dome is scaled by the same factor. In addition Figure (6.4) displays results obtained with quantum well calculations we have performed. As can be seen the tran-

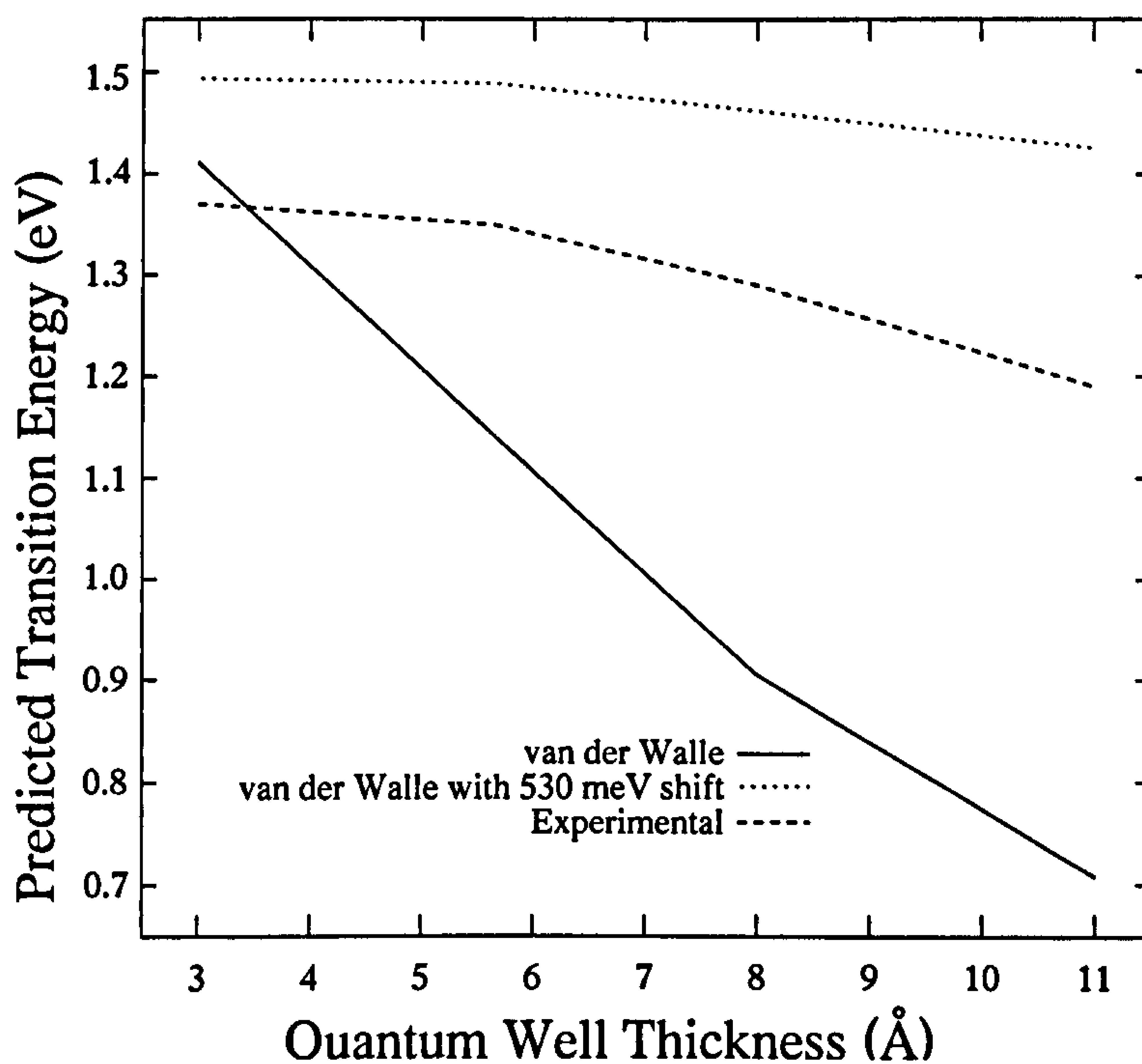

Figure 6.4: The A plot of the variation of the transition energy against quantum dome height using (a) a potential derived from van der Walle, (b) the same potential with a 530 meV shift inside the dome.

sition energies obtained using the shifted well depths better match the trend of the experimental results obtained by Ledentsov, (1995) in comparison to the unshifted energies.

6.3 Discussion

The purpose of this study is to find a way of bridging the gap between theory and experiment and to offer a new model that might open the way for fresh experimentation. We think that this objective has been achieved: the hypothesis of a "new" band offset clearly is a useful one since it offers testable predictions about the manifold of observable transitions. However, this is by no means the only "interpretation" of our modeling experiment.

Let us first set the tone of this discussion by a cautionary remark about the accuracy of our numerical model; our calculation is still too rough to offer more than a plausibility argument. As we commented in the above paragraphs, neither the precise size nor the shape of the dot are well established experimentally to justify the computational effort needed to account for these parameters. Hence we think that the somewhat arbitrary choice of the dome structure and the scaling are well in keeping with the level of empirical information available for this system and with our experience with this class of system. In any case, we do not expect the uncertainties introduced by these approximations to affect huge differences such as the shift in the band offset but we propose to treat the quanti-

tative aspects of our predictions with some scepticism. Furthermore, it is worth remarking that in the previously a number of calculations have been performed to test such models in a variety of low dimensional structures (Wong, 1987) usually with a view to test the simplifications typical of the particle in a box type calculations. However, provided that the atomic arrangement remains intact to conform to the idealisations normally assumed in most models, only the smallest of structures (of order one bulk lattice constant) exhibit significant deviations of energy level positions from the particle-in-a-box picture of confinement. Corrections such as the familiar light and heavy hole mixing can be included without having to abandon the model. Given the objectives set out in this study, any increase in sophistication cannot be justified.

If we accept our results as qualitatively correct, we can now discuss the options opened by our result, i.e. by the apparent improvement achieved by adopting the new - experimental - value of the band offset. Firstly, it is quite conceivable that there is a large error in the calculated value of the band offset available in the literature for this interface. The story of GaAs-AlAs - surely an "easy" interface to model compared to that in question here - suggests that *ab initio* calculations (Jaros, 1988) may not always have the predictive power required for an accurate determination of band offsets. Since there is no other experiment to test this new value it simply remains as the most obvious possibility and therefore one we have adopted. However, it is also that the message here is that we must abandon the standard picture of confinement that requires constructive

interference made possible by the walls of an ideal "box". Instead, it might be profitable to postulate another model in which the transitions take place via quantum states localised at the interface such as those discussed in other strained systems (Turton, 1996). However, such states are also likely to be affected by any deviation from ideal atomic arrangement (Shaw, 1996) and local clustering and interdiffusion. It is also possible to separate the two models (Turton, 1996; Presting, 1996) but one must possess information about higher transitions and their temperature and directional dependence; we hope that our results will encourage just such experiments. The difference between the two types of binding is far from academic; for example the volume in momentum space needed for effective lasing and the optical response are different depending whether one has a continuum of states or not.

6.4 Summary

To summarise, the conflict between experimental observations and theoretical calculations have been examined for GaSb/GaAs. We employed our method for electronic band structure calculations — developed to take full account of the strain distribution in the system — on a GaSb/GaAs quantum dome structure. The results indicate that the discrepancy may be usefully studied by adopting a model of confinement in which the conduction band offset is much smaller than previously thought. We propose that the lower limit of the conduction band offset is 100 meV due to the

effect of strain near the interface. Alternatively, we must assume that the quantum states participating in the the observed transitions are linked to the interfaces and possible disorder effects in these regions.

Chapter 7

Direct Modeling of GaSb/GaAs Quantum Dot Structures

GaSb/GaAs quantum dots show a large variation in their physical sizes but a remarkablely consistent photoluminescence spectra (Glaser, 1996). Experimentalists then discount quantum confinement as a possible explanation for this effect because they only consider a simple constant-depth quantum well model to explain their results. This simple model is inadequate because of the variation in strain caused by the differing height/width aspect ratios of the dots. Previously, we have attempted to reconcile conflicting experimental results by using an empirical fit for the conduction and valence band offsets. In this chapter we revisit the GaSb/GaAs quantum dots reported by Glaser, (1996) and adapt our method to model directly the quantum dots sizes reported. We then demonstrate that the apparent contradiction between the large variation of quantum

dot sizes and their remarkablely consistent photoluminescence spectra is not inconsistent with theory.

7.1 Adaptation of the Method for Larger Unit Cell Sizes

As mentioned in the previous chapter, the methods outlined previously in this thesis become very computationally expensive for very large heterostructures. The solution to this expense is to parallelise the valence force field method for calculating the atomic positions and to exploit Fast Fourier Transforms (FFT) in the electronic structure calculation.

7.1.1 Parallelisation of the Valence Force Field Method

Parallelisation of the valence force field method (VFFM) involves dividing the unit cell into $\mathcal{N}$ equally sized (i.e. same number of atoms) regions and distributing the data across $\mathcal{N}$ identical processors (or nodes). Each node can then, in principle, perform energy and force calculations independently of each other node. Unfortunately, with the VFFM this is not completely possible because in order to calculate the total energy of all atoms on a given node there is a requirement for data from an adjacent node because the bond lengths and angles of adjacent atoms are required. Consequently we must consider carefully the implementation of the parallel VFFM. Figure (7.1) shows the concept of parallelisation of the VFFM

in terms of the distribution of atoms throughout the nodes in the parallel machine. The surface layers of node 0 must be copied to nodes 1 and 2 and the overlap between the two surface layers must be copied to node 3. Of course the equivalent data copying must be performed by nodes 1, 2 and 3 to the relavent nodes. This will provide each node with all the necessary information required to perform it's own calculation using the VFFM.

Using the parallel VFFM, the processor time and memory requirement for relaxation is reduced by a factor of $\mathcal{N}$. The results that are presented in this chapter were performed on 64 nodes of a CRAY T3E900 and took approximately three and a half hours to perform 1000 iterations (cf 1-2

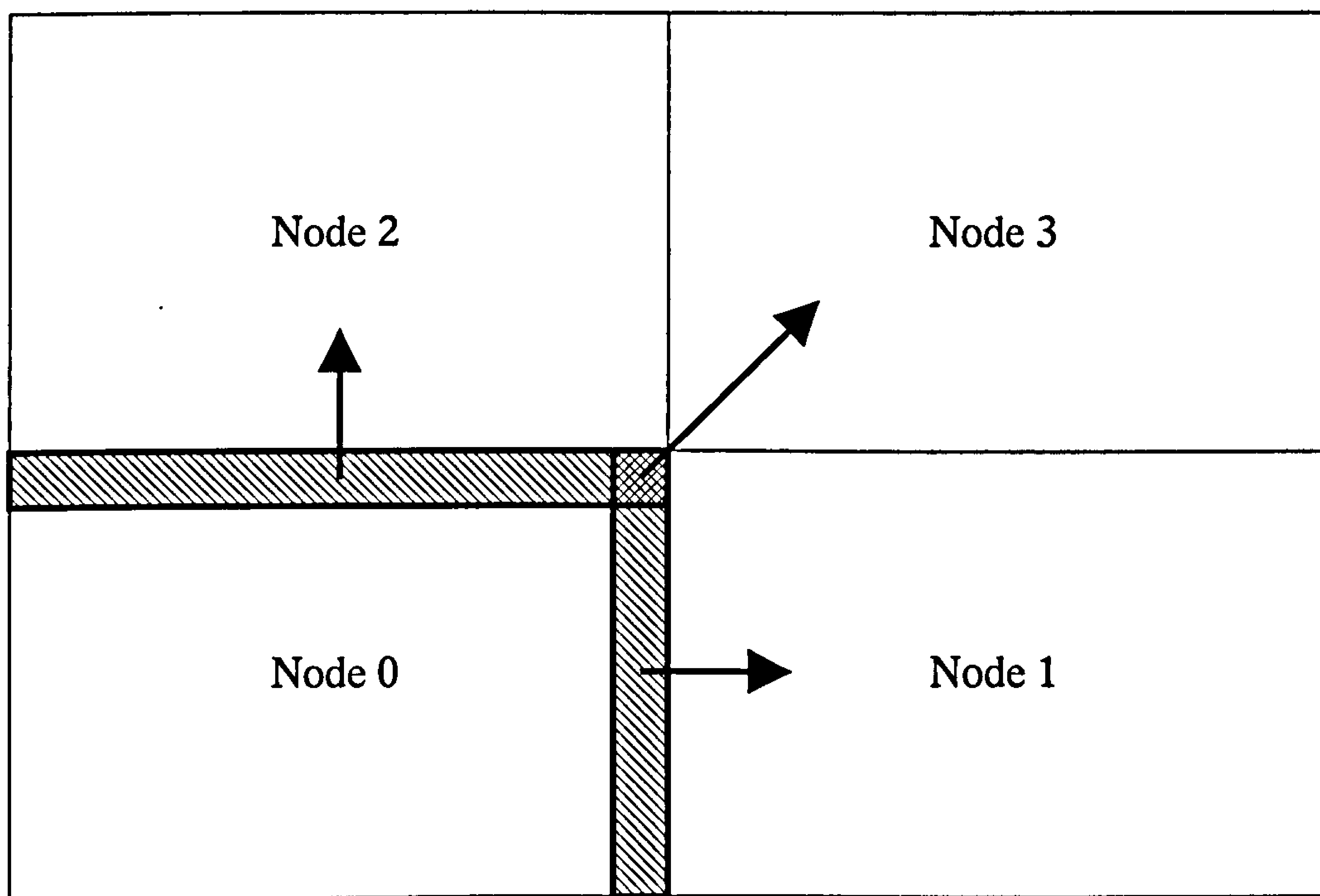

Figure 7.1: This figure illustrates the necessary data copying required to perform the VFFM in parallel.

weeks for 400 iterations in serial).

7.1.2 Optimisation of the Electronic Structure Calculation

The calculation of the electronic structure by the $\mathbf{k} \cdot \mathbf{p}$ method outlined earlier scales poorly with N_G, the number of plane waves in the wavefunctions expansion. This is because as the number of unit cells $\mathcal{N}$ is increased, the computational expense increases in proportion to $N_G^2 \sim \mathcal{N}^2$ a relationship that is introduced by Equation (4.6) through the evaluation of the confining potential. In the previous chapter, we calculated the electronic structure of a unit cell with $> 2 \times 10^6$ atoms using $\sim 9 \times 10^4$ plane waves in approximately two days. If we are to perform calculations upon a unit cell with 16×10^6 atoms we clearly require a faster algorithm. Fortunately one is readily attainable.

Consider the following TISE:

$$H_0 \psi(\mathbf{r}) + V(\mathbf{r})\psi(\mathbf{r}) = E\psi(\mathbf{r}) \tag{7.1}$$

where $H_0 = -\frac{\hbar\nabla^2}{2m}$. If we consider the simple example of a single electron (with an effective mass, m^*) in a single conduction band we obtain:

$$\frac{\hbar^2}{2m*} \mathrm{g}^2\, \psi(\mathbf{r}) + V(\mathbf{r})\psi(\mathbf{r}) = E\psi(\mathbf{r}) \tag{7.2}$$

If we then note that a part of the diagonalisation process is the calculation of $H\psi_{\text{trial}}(\mathbf{r})$, then by performing an FFT on the trial wavefunction then evaluating $H\psi_{\text{trial}}(\mathbf{g})$ and FFTing the result, we can then simply evaluate $V(\mathbf{r})\psi(\mathbf{r})$ and add the two results. This then makes the matrix diagonalisation process scale as $2N_G \ln(N_G)$, that is, roughly a factor of N_G faster

than before. This method can be extended to the EMA by substituting H_0 for $\overline{\overline{H_{LK}}}$. Using this process an electronic structure calculation with 2×10^6 atoms may be performed within one hour.

The two developments described here, then, have decreased the computational time required to model a large heterostructure from over one week to about four hours and consequently have made possible the following calculations.

7.2 Results and Discussion

The choice of the self-assembled quantum dot (SAQD) structures to be modeled is determined by experimental results published by Glaser, (1996) estimating the SAQD sizes of GaSb/GaAs to be in the range 50 – 100Å high and 200 – 400Å wide. This range can be considered typical for GaSb/GaAs SAQDs as many other researchers have reported similar sizes. Table 7.1 contains a list of the SAQD sizes we have used in our calculations. Notice that these structures cover a wide range of aspect ratios i.e. base:height ratios of 1:2, 1:4 and 1:8. We will show that the aspect ratio plays a key role in the determination of the SAQD potential and hence the electronic structure. Aside from the size of the SAQDs, a further important point is the *shape* of the SAQDs. Generally, a four-sided pyramidal structure is modeled because this shape has been determined to be that of the SAQDs after formation (i.e. pre-capping). However, it is unlikely that this shape is retained after capping. In a previous chapter we proposed that a dome

shaped (or hemi-spherical) SAQD was a more realistic shape for the embedded SAQD. Consequently, for completeness, we have modeled both pyramidal and dome-shaped SAQDs.

Figures (7.2)-(7.7) show the hydrostatic and biaxial strains of each of the six structures. Interestingly, the hydrostatic strain (HSS) for each of the six structures is almost constant throughout the SAQD regions at $\sim$ 7.5% (i.e. about $\sim$ 2% change in lattice constant). This result is particularly interesting as it shows that the fractional change in volume is the same for GaSb/GaAs SAQDs regardless of shape, size or aspect ratio. Therefore a potential dependent only on HSS for *any* GaSb/GaAs SAQD will have the same, constant well depth to a good approximation. This then leads us to the view that the commonly used simple model, based on a constant well depth derived from hydrostatic strain only, is a fair representation of the actual potential within a SAQD structure. Therefore, we have used **k.p** theory to calculate the potentials for all six structures *in the absence of biaxial strain*. We find that the well depth for all six structures is about 600meV. Of course the lack of biaxial strain means that the HH and LH potential are still degenerate. Table 7.1 shows the ground state energies (GSE) of the six structures in the absence of biaxial strain. Obviously, all the GSEs are less than 600meV and correspond to a transition energy between valence GSE to GaAs conduction band edge of about 1 eV. This, coincidentally is similar to the emission energies found by various experimental measurements (Glaser, 1996; Hatami, 1998). So, can it be possible that only HSS is playing a role in the determination of the poten-

tial ? This is unlikely as there is no reason whatsoever to discount the role of biaxial strain from the calculation. Also, the most likely reason for poor contact with experiment for GaSb/GaAs SAQDs is that the theoretically derived conduction band offset (VdW) does not agree with experiment (Glaser, 1996). We therefore expect that for GaSb/GaAs SAQDs any simple square well based solely on hydrostatic strain will systematically *underestimate* the confinement and therefore overestimate the transition energy. We can draw this conclusion by examining Figures (7.8)-(7.13) and noting that the well depth for the six structures is significantly more than 600meV. Clearly, this is a consequence of biaxial strain and its effect on the HH and LH potentials. For example, compare structure 3 to structure 5 (Figures (7.10) and (7.12)). Both of these dots have dome shapes but different aspect ratios. Both dots have virtually the same hydrostatic strain. However, structure 5, the *bigger* dot has the *least* confined eigenvalue with respect to (w.r.t.) the GaAs valence band edge. This paradox is explained by examining the biaxial strain profile of the two dots. Structure 3 has a roughly constant biaxial strain of about 20-25% within the dot. This compares to the biaxial strain of structure 5 that varies between a maximum of about 25% at the base of the dome and a minimum of 10% at the apex, within the dot. There are several important points to make regarding this issue. Firstly, the physical origin of this difference can be explained by simply considering the differing aspect ratios. This difference then causes the cubic unit cells to be distorted in different directions. Secondly, the amount of cube distortion across the GaSb/GaAs

interface is equal in both cases. For structure 3 there is about 25% biaxial strain just inside the base of the dome and about -10% just inside the GaAs barrier at the base, making about a 35% magnitude shift in biaxial strain between the barrier and well. There is also an identical shift at the apex of structure 3 (a 20% to -15% shift). For structure 2 there is a 20% - 15and a 10% - 25% shift at the apex. So the *magnitude* of the shift in biaxial strain across the interface is the same in both dots. However, with structure 5, the dot with a higher aspect ratio, the biaxial strain across the interface is shifted into the barrier, particularly at the apex. The effect of this differing strain distribution on the potential is that: Firstly, the heavy-hole potential in structure 5 is not as deep as in structure 3 and secondly, that this is especially true towards the apex of the dot. It is therefore the differing biaxial strain that explains the sloped HH-potential within structure 5.

So, to summarise this example, because the magnitude of biaxial strain within the dot in structure 5 is less than that in structure 3 the potential is shallower. In particular the biaxial strain is much less near the apex of the dots. This results in the sloped potential within the dot of structure 5. The important effect of this result is that the envelope-function in structure 5 is confined to the *base* of the dot and that the eigenvalue is less confined than the ground-state energy of structure 3 w.r.t the GaAs valence band edge.

The same explanation can also be applied to structures 4 and 6 that are pyramidal in shape (see Figures (7.11) and (7.13)). Both of these structures

Structure	Base (Å)	Height (Å)	Shape	GSE (HSS only) meV	GSE (Full) meV
1	50	400	Dome	−578	−956
2	50	400	Pyr	−569	−931
3	50	200	Dome	−522	−917
4	50	200	Pyr	−501	−883
5	100	200	Dome	−557	−848
6	100	200	Pyr	−538	−857

Table 7.1: Ground states energies using potentials with and without biaxial strain effects for SAQDs of various dimensions and shapes

have less confined eigen-values than structure 3. Again the hydrostatic strain is approximately constant within the dots, but the biaxial strain varies from 20% strain at the base of structure 6 to -30% at the apex of the dot. This observation may be explained by considering the effect that the dot shape has on the distortion of the relaxed (strained) cubic unit cells. The effect of this large biaxial strain on the potential is similar to that described above only more exaggerated. This results in the shallower wells (w.r.t. structure 3) and, in the case of structure 6. a ground-state envelope-function that is even more confined towards the base of the dot.

7.3 Summary

We have shown that the large variation in dot sizes observed by Glaser, (1996) is not inconsistent with the comparatively small variation of the

photoluminescence spectra observed in these structures. This is because the valence band GSE is quite constant in different GaSb/GaAs self-assembled quantum dot structures. The biaxial strain distribution of these structures (and hence the shape and aspect ratio) plays an important role in keeping this variation in the GSE small.

We find that in general the hydrostatic strain for most SAQDs is approximately constant throughout the dot region. Furthermore, this hydrostatic strain is almost the same for any dot fabricated from the same material types. This observation however does not lead to the conclusion that every SAQD will have the same potential well depth because of additional effects from biaxial strain.

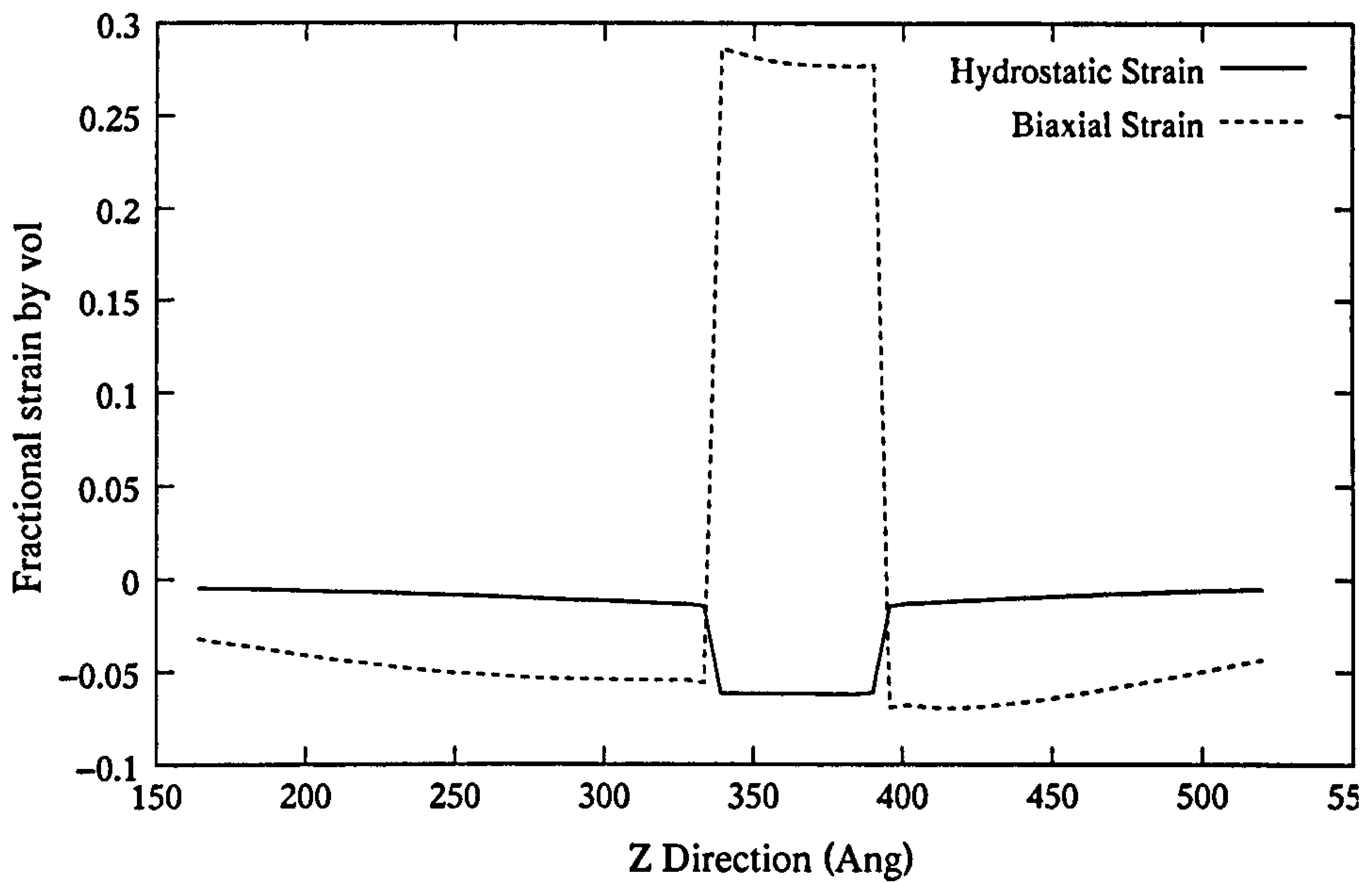

Figure 7.2: Structure 1: The hydrostatic and biaxial strain distribution through the centre of a GaSb/GaAs quantum dome of dimensions $x = y = 400\dot{A}$ and $z = 50\dot{A}$.

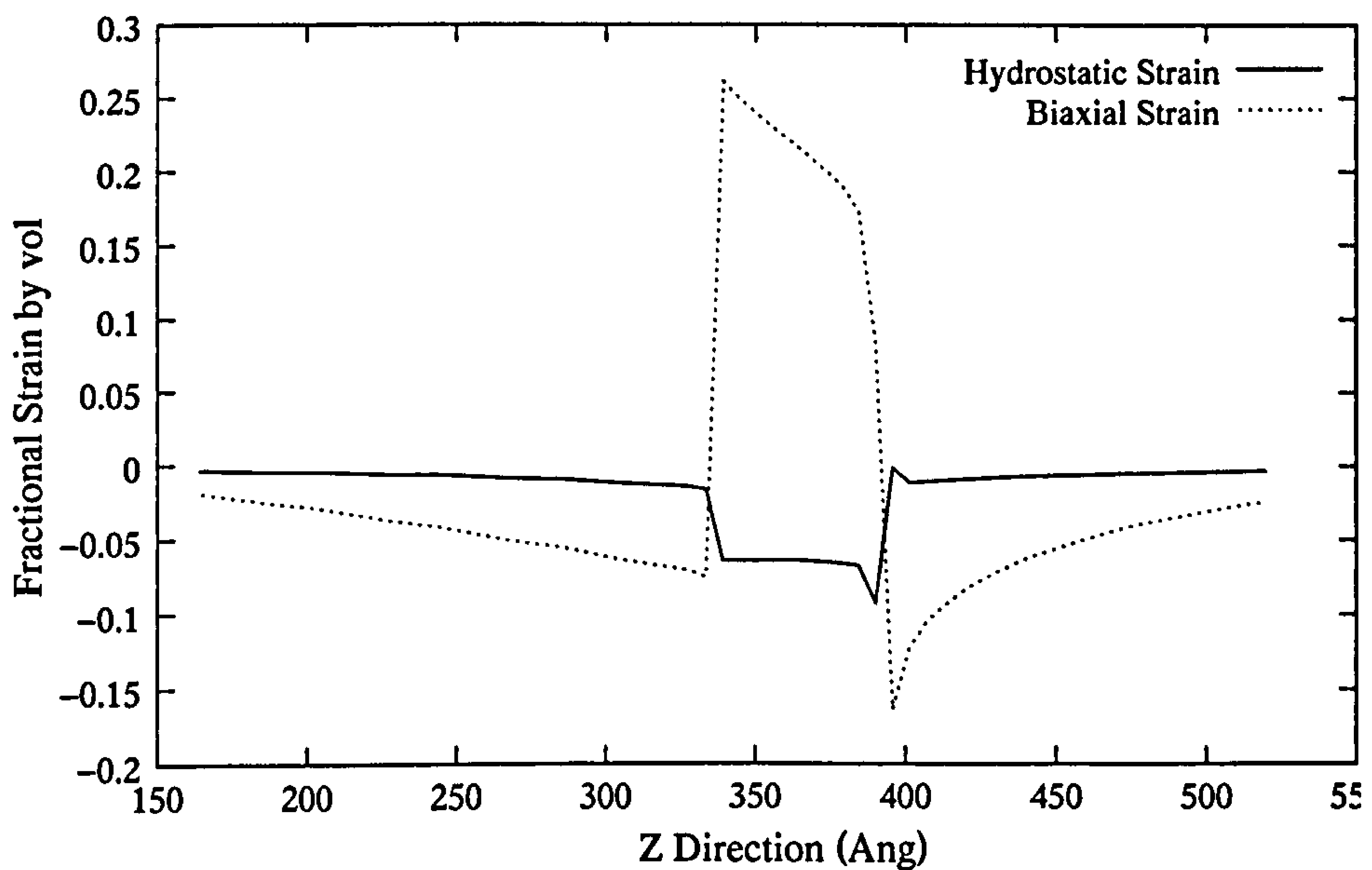

Figure 7.3: Structure 2: The hydrostatic and biaxial strain distribution through the centre of a GaSb/GaAs quantum pyramid of dimensions $x = y = 400\dot{A}$ and $z = 50\dot{A}$.

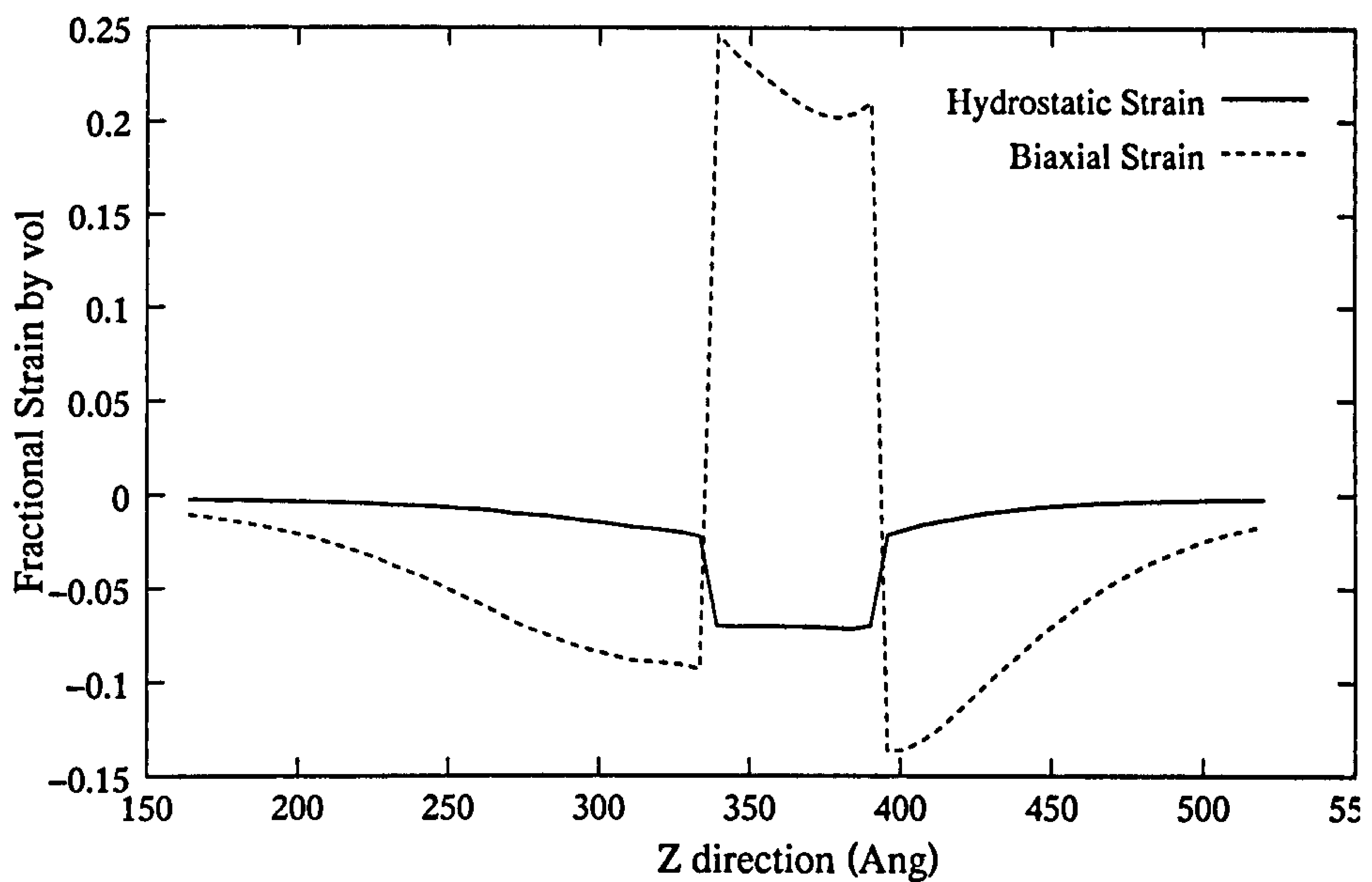

Figure 7.4: Structure 3: The hydrostatic and biaxial strain distribution through the centre of a GaSb/GaAs quantum dome of dimensions x = y = 200$\dot{A}$ and z = 50$\dot{A}$.

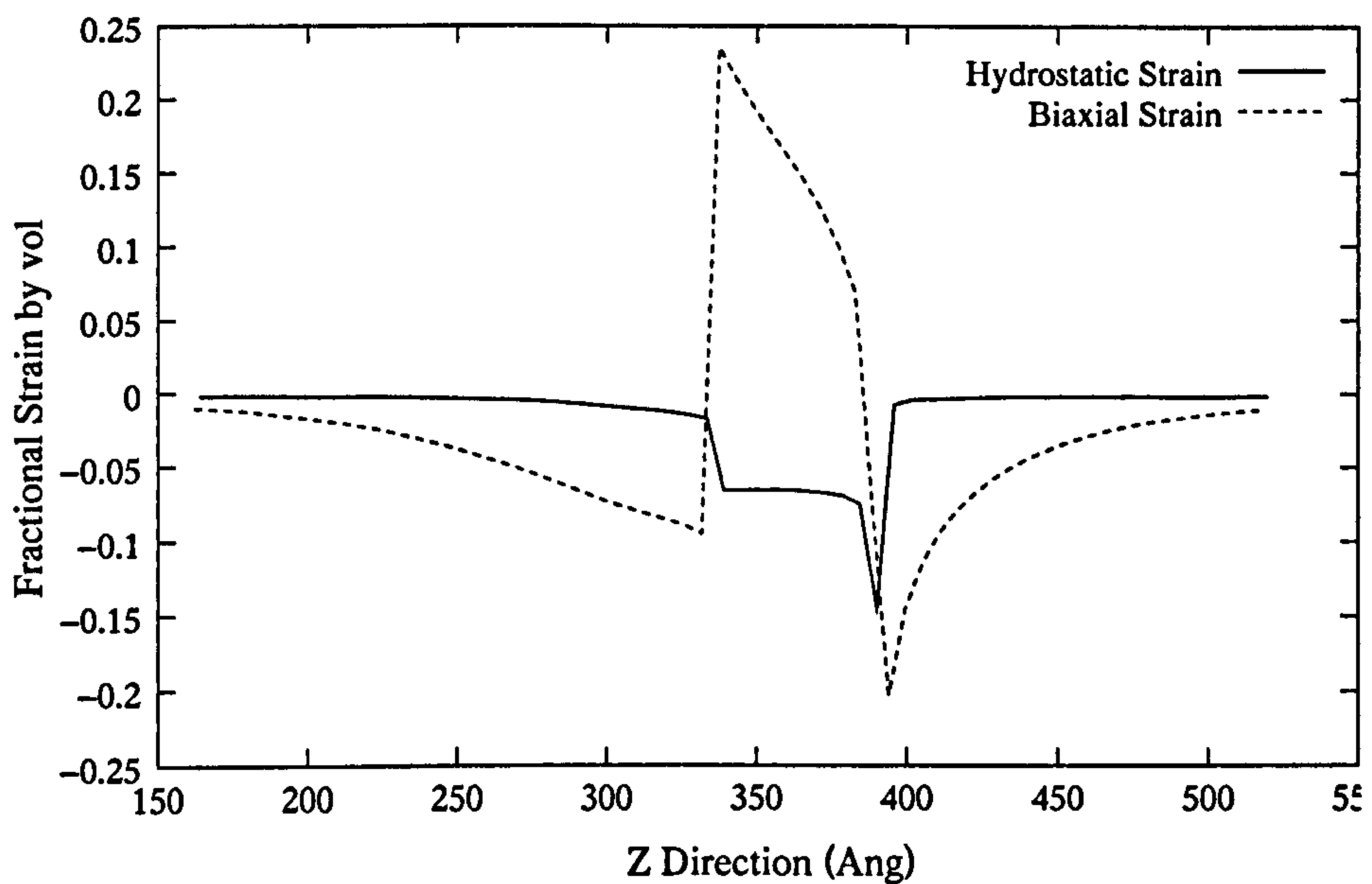

Figure 7.5: Structure 4: The hydrostatic and biaxial strain distribution through the centre of a GaSb/GaAs quantum pyramid of dimensions x = y = 200$\dot{A}$ and z = 50$\dot{A}$.

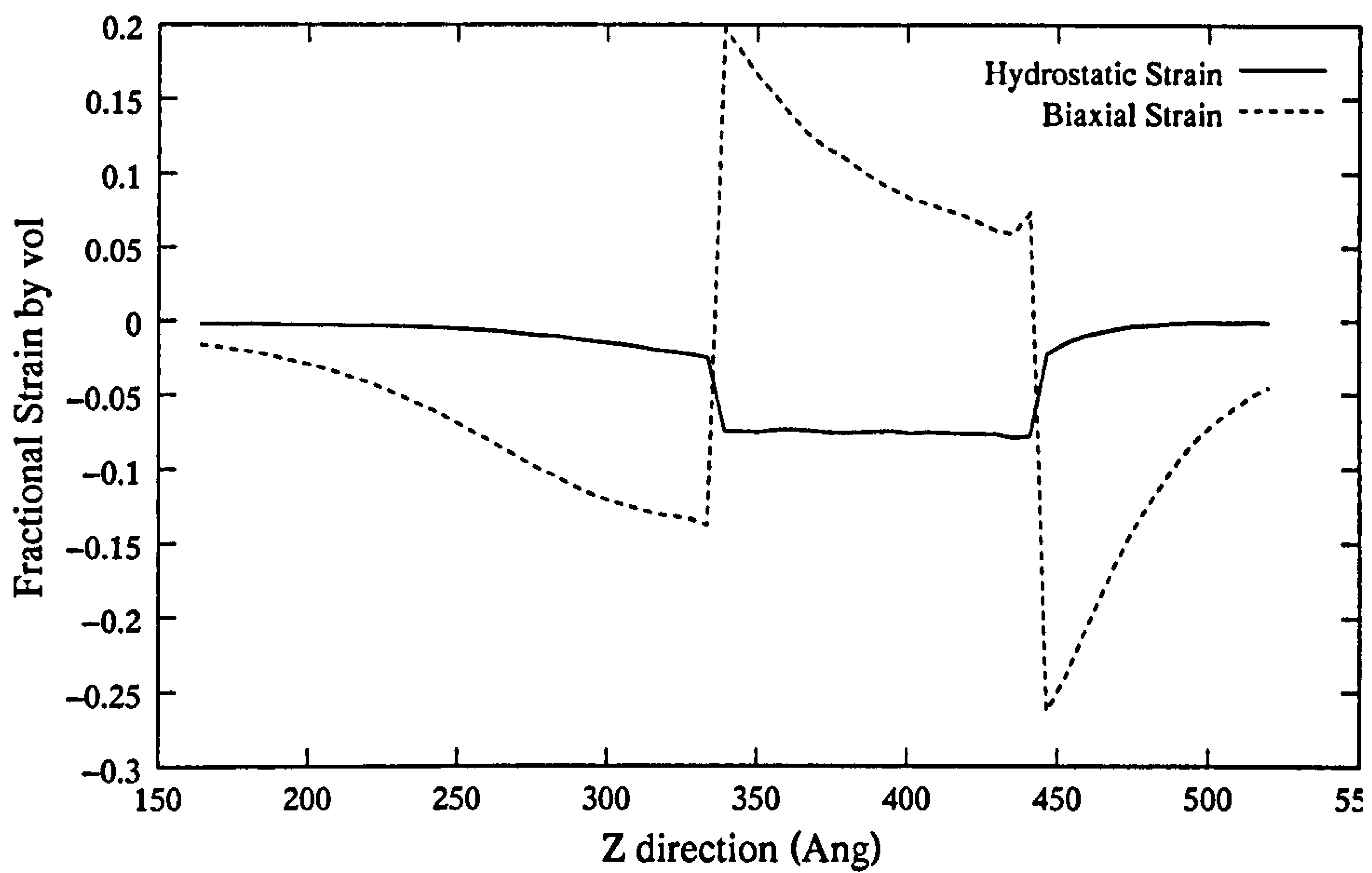

Figure 7.6: Structure 5: The hydrostatic and biaxial strain distribution through the centre of a GaSb/GaAs quantum dome of dimensions $x = y = 200\mathring{A}$ and $z = 100\mathring{A}$.

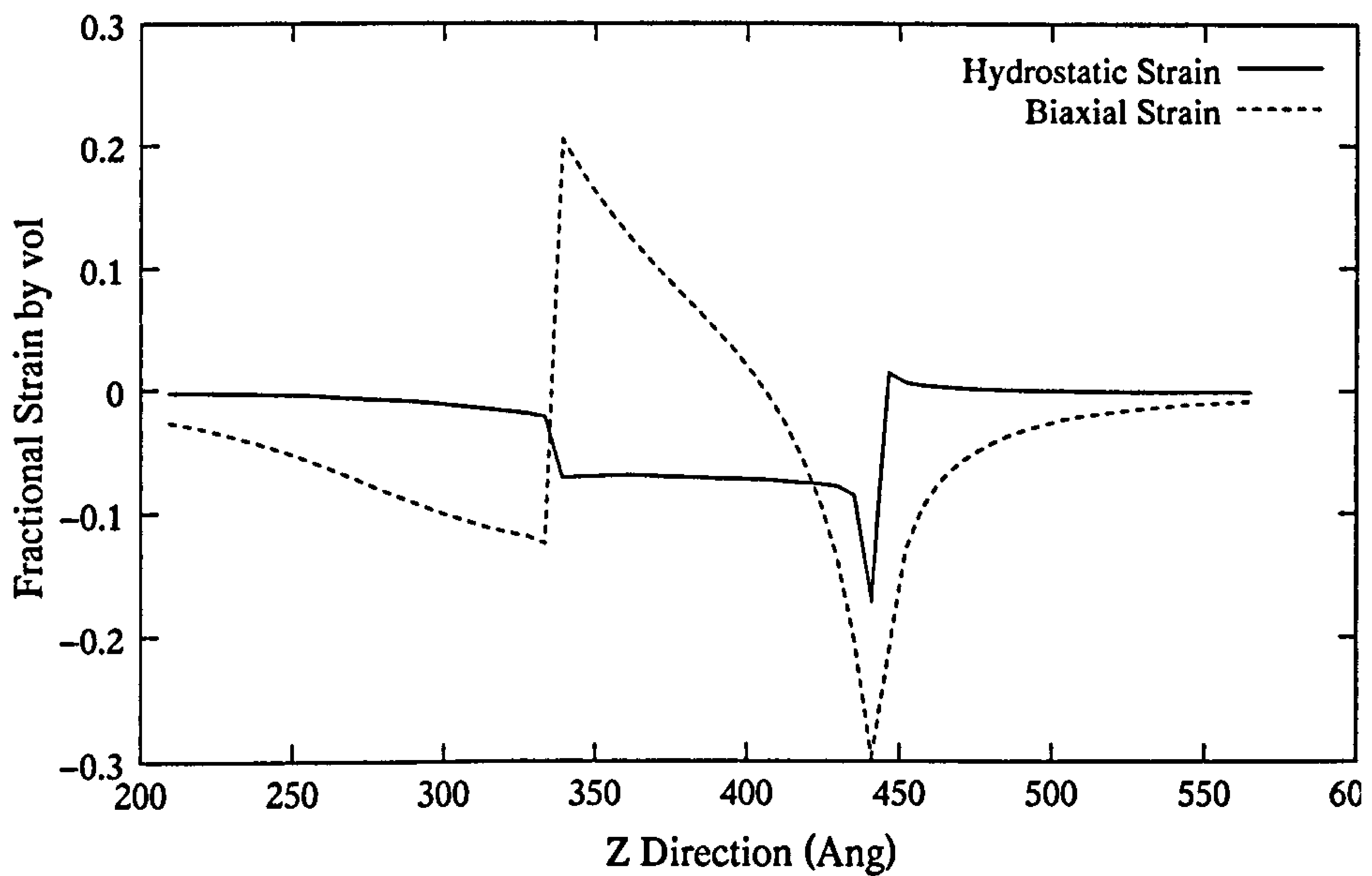

Figure 7.7: Structure 6: The hydrostatic and biaxial strain distribution through the centre of a GaSb/GaAs quantum pyramid of dimensions $x = y = 200\mathring{A}$ and $z = 100\mathring{A}$.

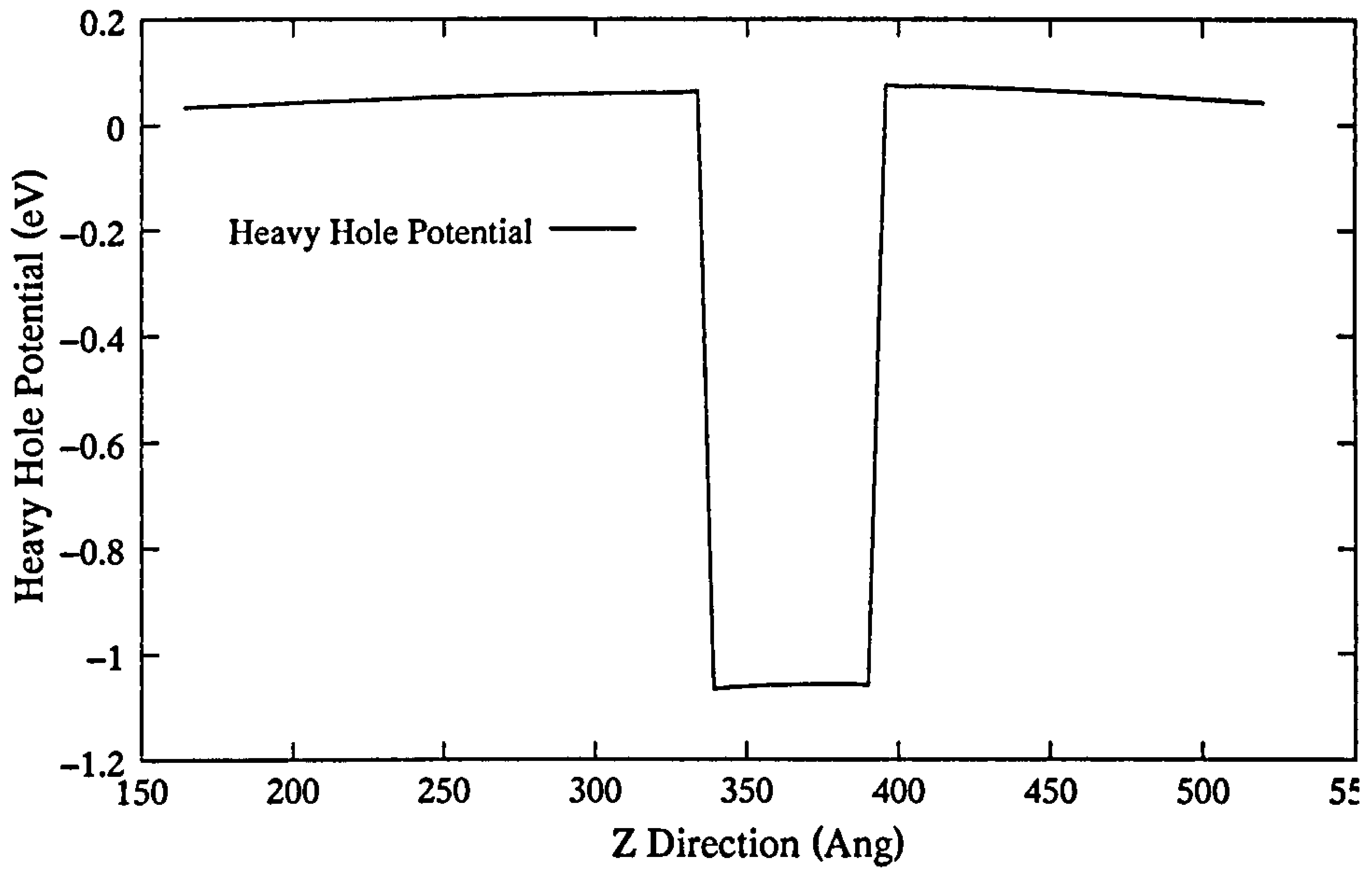

Figure 7.8: Structure 1: The heavy-hole potentials through the centre of a GaSb/GaAs quantum dome of dimensions x = y = 400$\dot{A}$ and z = 50$\dot{A}$.

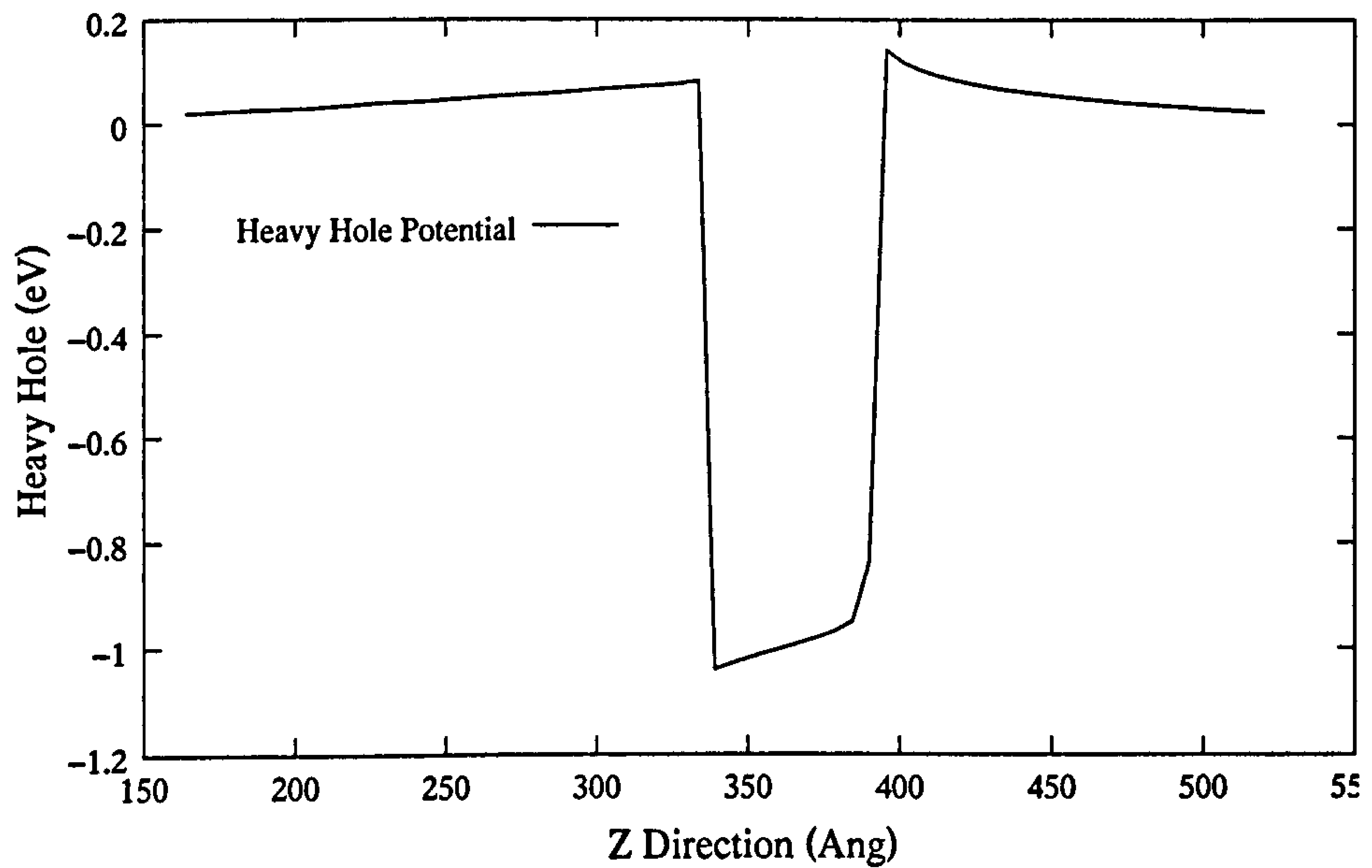

Figure 7.9: Structure 2: The heavy-hole potentials through the centre of a GaSb/GaAs quantum pyramid of dimensions x = y = 400$\dot{A}$ and z = 50$\dot{A}$.

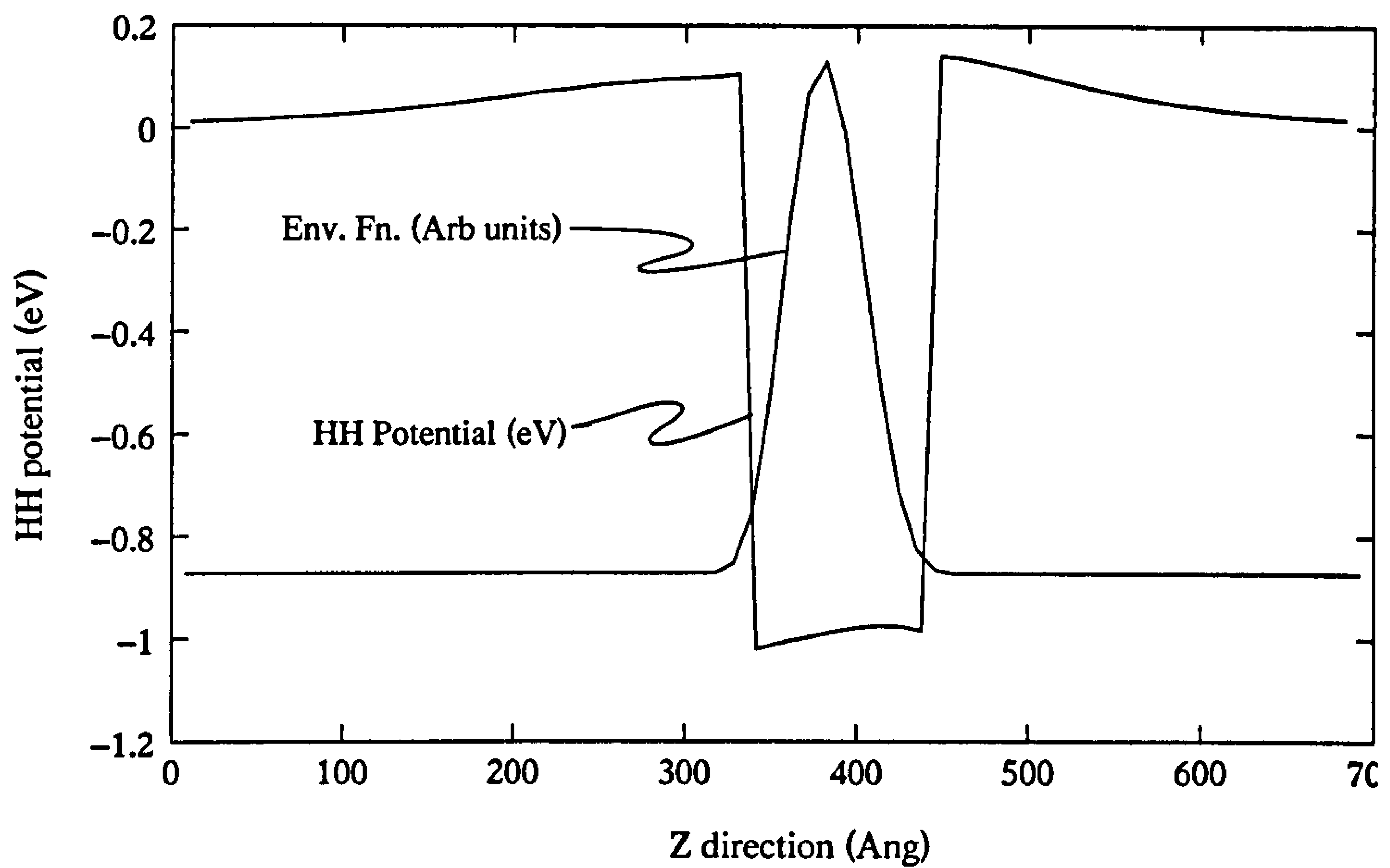

Figure 7.10: Structure 3: The heavy-hole potentials through the centre of a GaSb/GaAs quantum dome of dimensions x = y = 200Å and z = 50Å.

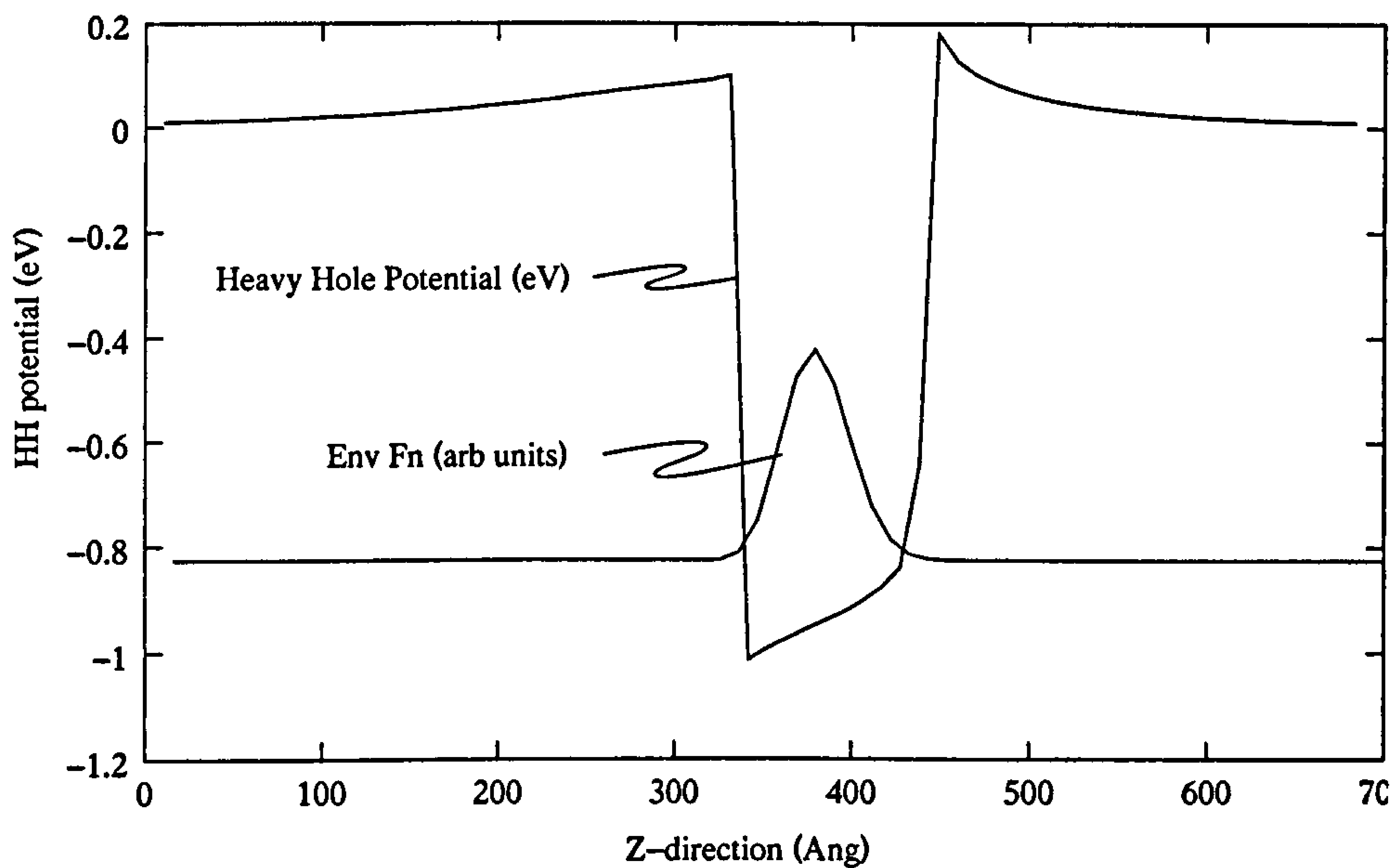

Figure 7.11: Structure 4: The heavy-hole potentials through the centre of a GaSb/GaAs quantum pyramid of dimensions x = y = 200Å and z = 50Å.

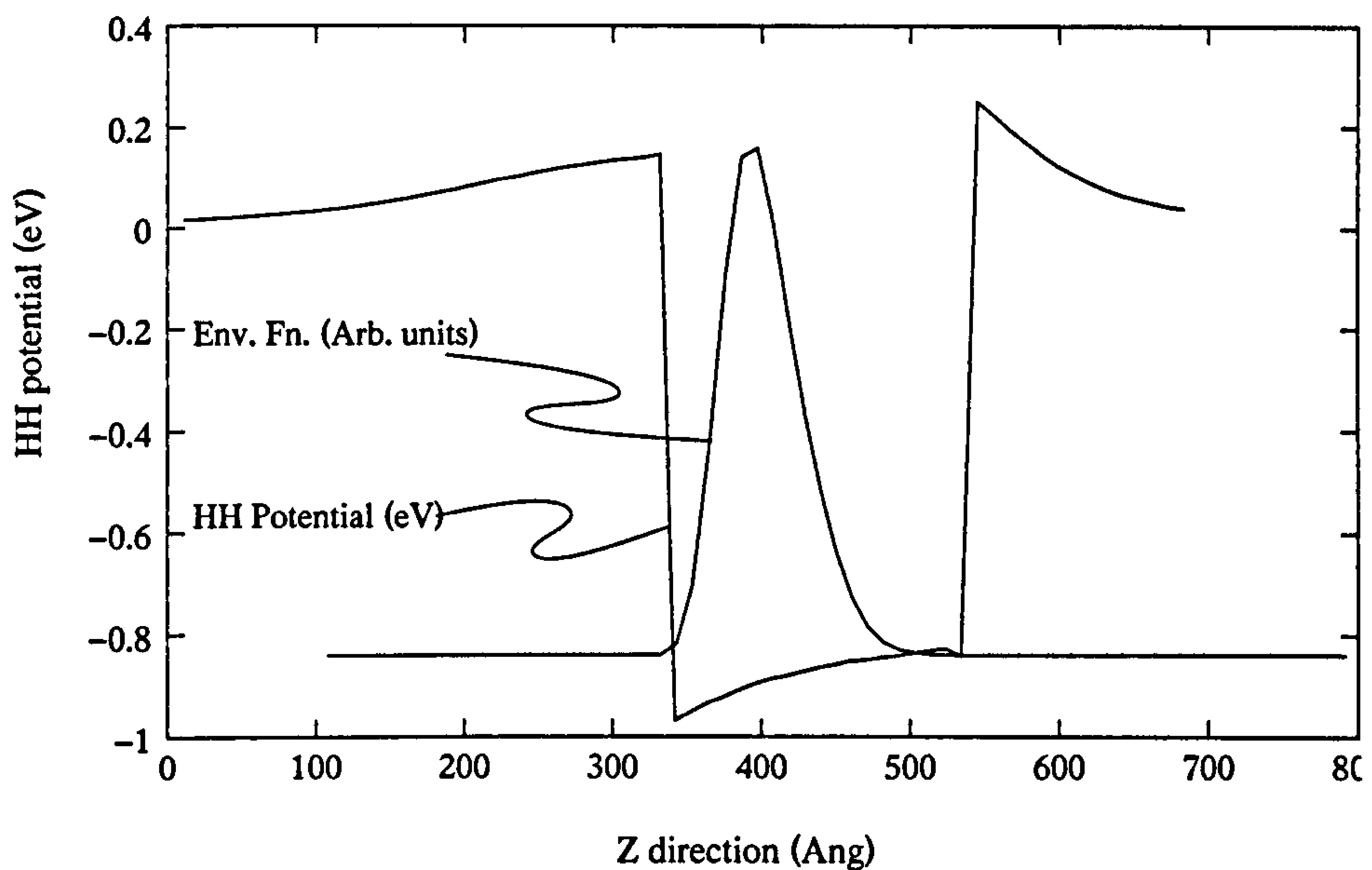

Figure 7.12: Structure 5: The heavy-hole potentials through the centre of a GaSb/GaAs quantum dome of dimensions x = y = 200Å and z = 100Å.

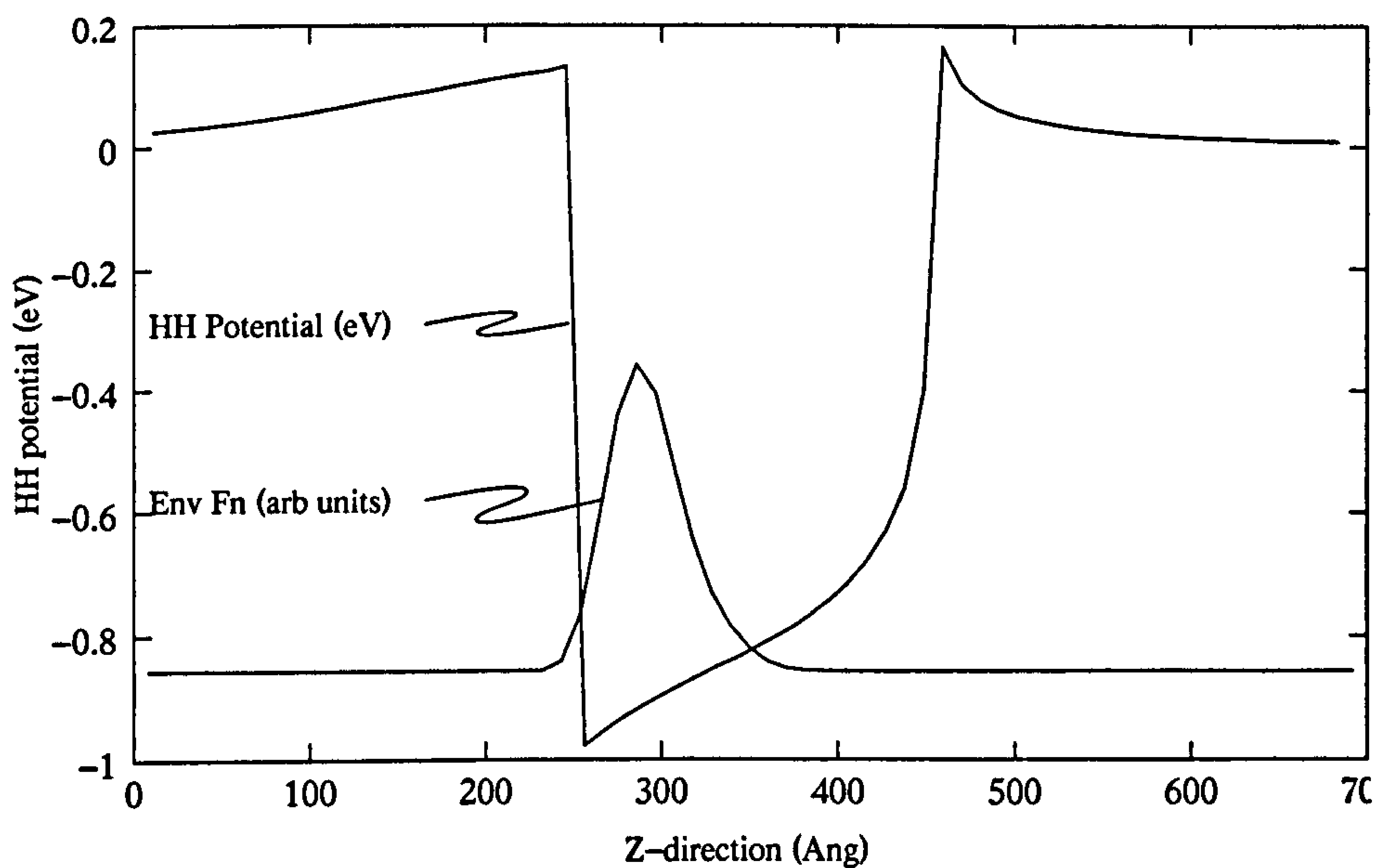

Figure 7.13: Structure 6: The heavy-hole potentials through the centre of a GaSb/GaAs quantum pyramid of dimensions x = y = 200Å and z = 100Å.

Chapter 8

Conclusions

The effects of hydrostatic and biaxial strain upon the bandstructure of self-assembled quantum dots (SAQDs) has been investigated. To undertake this task, established theories of the energy bands of solids have been taken, optimised and finally applied to describe electronic and potential optical properties in a range of semiconductor heterostructures. In this chapter, we summarise the principal findings of this study and provide suggestions on how to extend the calculation and models.

The calculation of atomic positions of a heterostructure containing two lattice mismatched semiconductors was described. A method for calculating the effect of these new atomic positions upon the "macroscopic" confining potentials was presented. Finally, the solution of the one electron Schrödinger equation was used to calculate the electronic structure of several heterostructures that show promising optical properties and others reported by experimentalists.

In chapter 5, we examined a series of Si/Ge based SAQDs using the effective mass approximation (EMA). Account was taken of the strain distribution imposed on the heterostructure because of the lattice mismatch. The extreme biaxial strain affects the Δ-valley in such a way as to create a localised state at the apex of the pyramid. This puts the electrons and holes in close proximity and enhances the probability of a optical transition. Also, the bandgap in these structures is in the 3-5μm range of wavelengths. This regime is inaccessible to intrinsic Si/Ge quantum well systems. Hence the SAQDs exhibit favourable optical characteristics that warrant further investigation.

We also applied the EMA to a number of GaSb/GaAs SAQDs reported by experiment, highlighting what has previously been deemed to be an apparent conflict between experiment and theory regarding the transition energies of the heterostructures. We found that suspicion is placed upon the accepted value of the GaSb/GaAs conduction band offset. Agreement with experimental transition energies was obtained by applying a rigid shift of the GaSb potential in accordance with experimental measurement of the GaSb/GaAs conduction band offset.

By parallelising the method of calculation of the atomic positions and optimisation of the calculation of the electronic structure using Fast Fourier Transforms, we were able to apply the valence force field method (VFFM) and EMA to much larger structures. This approach enables the modelling of the large GaSb/GaAs SAQDs directly, without the need for scaling. The study revealed the role that biaxial strain plays in keeping the ground

state energy of the valence band very consistent across a range of SAQD sizes, shapes and aspect ratios.

8.1 Future Study

There are several extensions to calculation of the strain distribution, electronic structure and optical transitions in SAQDs that may be possible. A simple model for the inclusion of excitonic effects should be relatively straightforward (Bastard, 1990). Also, piezoelectric effects induced by shear strains could be determined as this will affect the confining potential. However, because the method presented here is unreliable at the interface, where the largest shear strains will likely occur, careful thought will have to be given to the method by which the strain tensor components are obtained from the relaxed atomic positions. It should also be possible to construct the confining potentials for different charge carriers by accounting for the gradient of the strain in the effective Hamiltonian, as outlined by Zhang, (1994). Another useful addition would be the inclusion of bulk conduction and split-off bands in the basis set used to construct the SAQD states. This should improve the accuracy of allowed transitions. Account could also be taken of the effect of the biaxial strain on the effective masses, as well as the variation of the effective masses at the interface and indeed throughout the SAQD. The theory of Burt, (1988) demonstrates how the second of these suggestions may be implemented. As for the first suggestion, careful consideration is needed of the empir-

ical pseudopotential method. A further possibility is that the empirical pseudopotential method may be applied *directly* to SAQD unit cells. Preliminary investigations into this option have revealed that it should be possible to calculate the valence and conduction band ground state energies of a SAQD structure with a unit cell $\sim 10^5$ atoms within a week on an inexpensive PC.

Bibliography

Ashcroft, N. W., and Mermin, N. D. (1976). "Solid State Physics", Saunders College Publishing, Philadelphia.

Apetz, R., Vescan, L., Hartmann, A., Dieker, C., and Lüth, H. (1995) *Appl. Phys. Lett.* 66, 445.

ARPACK, http://www.caam.rice.edu/software/ARPACK/

Bachelet, G. B., Hamann, D. R., and Schlüter, M. (1982). *Phys. Rev. B* 26, 4119.

Baraff, G. A., and Gershoni, D. (1991). *Phys. Rev. B* 43, 4011.

Bastard, G., and Brum, J. A. (1986). *IEEE J. Quantum Electron* 22, 1625.

Bastard, G. (1990). "Wave Mechanics Applied to Semiconductor Heterostructures", Les Editions de Physique, Paris.

Burt, M. G. (1988). *Semicond. Sci. Tech.* 3, 739.

Capasso, F., and Cho, A. Y. (1994). *Surface Science* 300(1-3), 878.

Chang, L. L., Esaki, L., Howard, W. E., and Ludeke R. (1973). *J. Vac. Sci. Technol.* 10, 11.

Cohen, M. L., and Bergstresser, T. K. (1966). *Phys. Rev.* 141, 789.

Cusack, M. A. PhD Thesis, "Electronic and Optical Properties of Semicon-

ductor Quantum Wells and Dots", University of Newcastle upon Tyne.

Cusack, M. A., Briddon, P. R., and Jaros, M. (1996). *Phys. Rev. B* **54**, 2300.

Cusack, M. A., Briddon, P. R., and Jaros, M. (1997). *Phys. Rev. B* **56**, 4047.

Dreizler, R. M., and Gross, E. K. U. (1990), "Density Functional Theory: An Approach to the Quantum Many-Body Problem", Spinger-Verlag, Berlin.

Eberl K. *et al*, (2000). *Thin Solid Films* **369**, 33.

Esaki, L., and Tsu R. (1970). *IBM J. Res. Develop.* **14**, 61.

Fraser, D. A. (1979). "The Physics of Semiconductor Devices", Calrendon Press, Oxford.

Gell, M. A. Ninno, D., Jaros, M., and Herbert D. C. (1986). *Phys. Rev. B* **34**, 2416.

Glaser, E. R., Bennett, B. R., Shanabrook, B. V., and Magno, R. (1996). *Appl. Phys. Lett.* **68**, 3614.

Grundmann, M., Christen, J., Ledentsov, N. N., Böhrer, J., Bimberg, D., Ruvimov, S. S., Werner, P., Richter, U., Gösele, U., Heydenreich, J., Ustinov, V. M., Egorov, A. Yu., Kop'ev, P. S., and Alferov, Zh. I. (1995a). *Phys. Rev. Lett.* **74**, 4043.

Grundmann, M., Stier, O., and Bimberg D. (1995b). *Phys. Rev. B* **52**, 11969.

Hatami, F. *et al*, (1998). *Phys. Rev. B* **57**, 4635.

Jaros, M. (1988). *Phys. Rev. B* **37**, 7112.

Jaros, M. (1990). "Semiconductors and Semimetals" **32**, 175.

Jones, R. (1988). *J. Phys. C* **21**, 5735.

Kittel, C. (1996). "Introduction to Solid State Physics", John Wiley and Sons, Inc., New York.

Kwok, S. H. *et al* (1999). *Phys. Rev. B* 59, 4980.

Ledentsov, *et al* (1995). *Phys. Rev. B* 52, 4058.

LeGoues, F. K., Tersoff, J., Reuter, M. C., Hammer, M., and Tromp, R. (1995) Appl. Phys. Lett. 67, 2317.

Löwdin, P. (1951). *J. Phys. Chem.* 19, 1396.

Lüth, Hansm (1998). *Appl. Sur. Sci.* 130-132, 855.

Luttinger, J. M., and Kohn, W. (1955). *Phys. Rev.* 97, 8690.

Luttinger, J. M. (1956). *Phys. Rev.* 102, 1030.

Mansareh, M. O. (Editor 1993). "Semiconductor Quantum Wells and Superlattices for Long-Wavelength Infrared Detectors", Artech House, Boston.

Martin, R. M. (1970). *Phys. Rev. B* 1, 4005.

Marzin, J.-Y., Gérard, J.-M., Izraël, A., Barrier, D., and Bastard G. (1994). *Phys. Rev. Lett.* 73, 716.

Mateeva, E., Sutter, P., and Lagally, M. G. (1999). *Appl. Phys. Lett.* 54, 567.

McMurry, H. L., Solbrig, Jr., A. W., Boyter, J. K., and Noble, C. (1967). *J. Phys. Chem. Solids* 28, 2359.

Medeiros-Ribeiro, G., Leonard, D., and Petroff, P. M. (1995). *Appl. Phys. Lett.* 66, 1767.

Moison, J. M., Houzay, F., Barthe, F., Leprince, L., André, E., and Vatel, O. (1994). *Appl. Phys. Lett.* 64, 196.

Musgrave, M. J. P., and Pople, J. A. (1962). *Proc. Roy. Soc. (London)* A268, 474.

Pollak, F. H. (1973). *Surface Science* 37, 863.

Pollak, F. H. (1990). "Semiconductors and Semimetals" (R. K. Willardson

and A. C. Beer, eds.) Vol. 32. Academic Press, New York.

Presting, H. (1996). *Appl. Phys. Lett.* **69**, 2376.

Prieto, *et al*, (1998). *Phys. Rev. Lett.* **80**, 1094.

Reed, M. A. (1993). *Scientific American* **268**, 118.

Rubin, M. E., Blank, H. R., Chin, M. A., Kroemer, H., and Narayanamurti, V. (1997). *Appl. Phys. Lett.* **70**, 1590.

Schulman, J. N., and Chang, Y. C. (1985). *Phys. Rev. B* **31**, 2056.

Shang Yuan Ren, (1996). *Solid State Commun.* **102**, 479.

Shang Yuan Ren, (1997). *Phys. Rev. B* 55, 4665.

Shaw, M. J. (1988). *Phys. Rev. B* 54, 16781.

Shaw, M. J. (1998). *Phys. Rev. B* 58, 7834.

Shaw, M. J., and Jaros, M. (1999). "Semiconductors and Semimetals" 56, 169.

Stranski, I. N., and Krastanow, Von. L. (1939). *Akad. Wiss. Lit. Mainz Math.-Natur. Kl. IIb* 146, 797.

Takagahara, T., and Takeda, K. (1992). *Phys. Rev. B* 46, 15578.

Turton, R. J., and Jaros, M., *Appl. Phys. Lett.* 69, 2891.

Van der Walle, C. G. (1989). *Phys. Rev B* 39, 1871.

Vinsome, P. K. W. (1971). PhD Thesis, "The Valence Charge Density and Dielectric Function in Covalent Semiconductors", University of Newcastle upon Tyne.

Wang, L. -W., and Zunger, A. (1996). *Phys. Rev. B* 54(16), 11417.

Wang, L. -W., Wei, S. -H., Mattila, T., Zunger, A., Vurgaftman, L., and Meyer, J. R. (1999). *Phys. Rev. B* 60(8), 5560.

Wang, L. -W., Williamson A. J., Zunger, A., Jiang, H., and Singh, J. (2000). *Appl. Phys. Lett.* **76**, 339.

Wong, K. B., Jaros, M. and Hagon, J. P. (1987). *Phys. Rev. Lett.* **69**, 2463.

Wood, D. M., Zunger, A., and Gershoni, D. (1996). *Europhys. Lett.* **33**(5) 383.

Xui-min Jiang *et al* (1998), *Thin Film Solids* **321**, 60.

Zhang, Y. (1994). *Phys. Rev. B* 49, 14352.